SYSTEM IDENTIFICATION USING FLIGHT TEST DATA

A THESIS SUBMITTED TO
THE GRADUATE SCHOOL OF NATURAL AND APPLIED SCIENCES
OF
MIDDLE EAST TECHNICAL UNIVERSITY

BY

ORKUN ŞİMŞEK

IN PARTIAL FULFILLMENT OF THE REQUIREMENTS
FOR
THE DEGREE OF MASTER OF SCIENCE
IN
AEROSPACE ENGINEERING

JANUARY 2014

Approval of the thesis:

SYSTEM IDENTIFICATION USING FLIGHT TEST DATA

submitted by **ORKUN ŞİMŞEK** in partial fulfillment of the requirements for the degree of **Master of Science in Aerospace Engineering Department, Middle East Technical University** by,

Prof. Dr. Canan Özgen _____
Dean, Graduate School of **Natural and Applied Sciences**

Prof. Dr. Ozan Tekinalp _____
Head of Department, **Aerospace Engineering**

Prof. Dr. Ozan Tekinalp _____
Supervisor, **Aerospace Engineering Dept., METU**

Examining Committee Members

Prof. Dr. Serkan Özgen _____
Aerospace Engineering Dept., METU

Prof. Dr. Ozan Tekinalp _____
Aerospace Engineering Dept., METU

Assoc. Prof. Dr. İlkay Yavrucuk _____
Aerospace Engineering Dept., METU

Asst. Prof. Dr. Ali Türker Kutay _____
Aerospace Engineering Dept., METU

Prof. Dr. M. Kemal Özgören _____
Mechanical Engineering Dept., METU

Date: 20.01.2013

I hereby declare that all information in this document has been obtained and presented in accordance with academic rules and ethical conduct. I also declare that, as required by these rules and conduct, I have fully cited and referenced all material and results that are not original to this work.

Name, Last name: Orkun ŞİMŞEK

Signature:

ABSTRACT

SYSTEM IDENTIFICATION USING FLIGHT TEST DATA

Şimşek, Orkun

M.Sc., Department of Aerospace Engineering

Supervisor: Prof. Dr. Ozan Tekinalp

January 2014, 150 pages

In this study, a linear model of an unmanned aerial vehicle (UAV) is developed by using frequency domain system identification methods. The data used in the identification methods are obtained by performing flight tests. To obtain appropriate flight test data for identification process, flight test maneuvers are designed. These flight test data are used in two main frequency domain system identification methods, namely, transfer function modeling and state space modeling. The linear models obtained by using these two methods are verified in time domain using flight test data obtained by applying inputs called as verification inputs.

A UAV is designed, produced and instrumented in Turkish Aerospace Industries, Inc. (TAI) as a test platform. In this thesis, this test platform is used to obtain flight test data. In identification process, two programs are mainly used, namely, Comprehensive Identification from Frequency Responses (CIFER®) and MATLAB®&Simulink®.

Keywords: Frequency domain system identification, Flight test, UAV, Transfer function modeling, State space modeling

ÖZ

UÇUŞ TEST VERİLERİ KULLANARAK SİSTEM MODELİ BELİRLEME

Şimşek, Orkun

Yüksek Lisans, Havacılık ve Uzay Mühendisliği Bölümü

Tez Yöneticisi: Prof. Dr. Ozan Tekinalp

Ocak 2014, 150 sayfa

Bu çalışmada, frekans tabanlı sistem modeli belirleme yöntemleri ile bir doğrusal insansız hava aracı (İHA) modeli geliştirilmiştir. Bu belirleme yöntemlerinde kullanılan veriler, uçuş testleri gerçekleştirilerek elde edilmiştir. Uçuş test verilerini bu yöntemlerde kullanılabilir hale getirmek için, test manevraları tasarlanmıştır. Bu uçuş test verileri, transfer fonksiyon modelleme ve durum uzay modelleme isimli iki temel frekans tabanlı sistem modeli belirleme yönteminde de kullanılmıştır. Bu iki yöntem kullanılarak elde edilen doğrusal modeller, doğrulama girdileri olarak adlandırılan girdiler ile elde edilen uçuş test verileri ile doğrulanmıştır.

Test platformu olarak kullanılmak üzere bir insansız hava aracı Türk Havacılık ve Uzay Sanayii A.Ş. (TUSAŞ)'de tasarlanmış, üretilmiş ve enstrümantasyonu yapılmıştır. Bu tezde, uçuş test verilerini elde etmek için bu platform kullanılmıştır. Model belirleme sürecinde CIFER® ve MATLAB®&Simulink® adlı iki program kullanılmıştır.

Anahtar Kelimeler: Frekans tabanlı sistem modeli belirleme, Uçuş test, Transfer fonksiyon modelleme, Durum uzayı modelleme

To My Family

ACKNOWLEDGMENTS

First, I would like to express my sincere gratitude to my supervisor Prof. Dr. Ozan Tekinalp for his guidance, encouragements, and advices. His experience, knowledge and effective feedbacks helped me to complete this work.

I would like to express my special thanks to my chief engineer Gürkan Çetin and my leader E. Hakan Orhan in TAI for their support on the thesis subject, their patience and motivation. Also, I would like to thank my co-workers Halil Kaya, Senem Ayşe Haser, Umut Türe, Deniz Karakaş and Volkan Kargın for their friendships and advices. Especially, I would like to thank Hakan Tiftikçi for his useful discussions with me during the thesis.

I would like to express my special thanks to test pilot Tamer Ekinci for his support, guidance and motivation. His responsive attitude towards the identification tests makes the test processes easy, quick and successful. I would like to thank project manager Mehmet Karakaş and project member Yavuz Öztürk for their understanding and support.

I would like to express my special thanks to my parents and my brother for their endless support and thrust throughout my life. It would be impossible for me to finish this thesis without their love. I would like to thank Kadriye Güçlü for her endless support and understanding.

Finally, I would like to thank The Scientific and Technological Council of Turkey (TUBITAK), since this study was supported by TUBITAK-BIDEB National Scholarship Program for M.Sc. Students.

TABLE OF CONTENTS

ABSTRACT ..... **v**

ÖZ ..... **vi**

ACKNOWLEDGMENTS ..... **viii**

TABLE OF CONTENTS ..... **ix**

LIST OF TABLES ..... **xii**

LIST OF FIGURES ..... **xiii**

LIST OF ABBREVIATIONS ..... **xv**

CHAPTERS **1**

1 INTRODUCTION **1**

1.1 Background and Motivation **1**

1.2 Literature Review **6**

1.3 Scope of Research **7**

1.4 Research Objective **8**

1.5 Thesis Outline **8**

2 MATHEMATICAL BACKGROUND **11**

2.1 Frequency Response Theory **11**

2.1.1 Fourier Transform 13

2.1.2 Spectral Functions 15

2.2 Calculation of Frequency Response **16**

2.2.1 Windowing 16

2.2.2 Chirp-Z Transform 19

2.2.3 Coherence Function 19

2.2.4 Bode Plots 20

3 DATA GATHERING & RECONSTRUCTION 23
3.1 Introduction 23
3.2 Platform & Instrumentation 23
3.2.1 Platform 23
3.2.2 Instrumentation 24
3.3 Input Design 26
3.3.1 Identification Inputs 27
3.3.2 Verification Inputs 28
3.4 Inputs Applied in Flight Tests 33
3.5 Flight Path Reconstruction 38
4. TRANSFER FUNCTION MODELING 45
4.1 Introduction 45
4.2 Low Order Equivalent System (LOES) Modeling 49
4.2.1 MUAD Boundaries 49
4.2.2 Equivalent Time Delay 51
4.3 Model Structure Selection 56
4.4 Parameter Estimation 58
4.4.1 Longitudinal Transfer Function Modeling 60
4.4.2 Lateral-Directional Transfer Function Modeling 62
4.5 Handling Quality Analysis 74
5. STATE SPACE MODELING 79
5.1 Introduction 79
5.2 State-Space Model Structure 79
5.3 Accuracy Analysis & Model Structure Determination 83
5.3.1 Accuracy Analysis Metrics 84
5.3.2 Model Structure Determination Using Accuracy Analysis Metrics 87
5.4 State-Space Identification 88
5.4.1 Longitudinal Model Structure 89
5.4.2 Lateral/Directional Model Structure 97
5.5 Verification 102

5.6 State Space and Transfer Function Model Comparison 112
5.6.1 Comparison of the Graphs of Model Outputs and Flight Test Data .. 112
5.6.2 Comparison of the Transfer Functions of Both Models..... 115
6. CONCLUSION AND FUTURE WORK 119
6.1 Conclusion 119
6.2 Future Work 120
REFERENCES 121
APPENDICES 125
A. AIRCRAFT EQUIPMENT SPECIFICATIONS 125
B. SOFTWARE AND THEIR USAGE IN IDENTIFICATION PROCESS 129
B.1 CIFER 129
B.1.1 FRESPID 130
B.1.2 COMPOSITE 138
B.1.3 NAVFIT 140
B.1.4 DERIVID 142
B.2 SIMULINK PARAMETER ESTIMATION 146
B.2.1 Nonlinear Least Square Estimation 149

LIST OF TABLES

TABLES

TABLE 1.1 UAV OPERATOR COUNTRIES IN 2009 1
TABLE 3.1 LIST OF MEASURED QUANTITIES 25
TABLE 3.2 VARIABLES FOR OEM 42
TABLE 4.1 CLASSIFICATION OF LEVELS OF FLYING QUALITIES [24] 75
TABLE 4.2 LONGITUDINAL RESPONSE CHARACTERISTICS 76
TABLE 4.3 LATERAL-DIRECTIONAL RESPONSE CHARACTERISTICS 77
TABLE 5.1 LONGITUDINAL STATE SPACE MODEL STRUCTURE ARRAYS 90
TABLE 5.2 MODIFIED LONGITUDINAL STATE SPACE MODEL STRUCTURE ARRAYS 93
TABLE 5.3 LONGITUDINAL STATE SPACE IDENTIFICATION RESULT – STEP 1 93
TABLE 5.4 LONGITUDINAL STATE SPACE IDENTIFICATION RESULT – STEP 2 94
TABLE 5.5 LONGITUDINAL STATE SPACE IDENTIFICATION RESULT – STEP 3 95
TABLE 5.6 LONGITUDINAL STATE SPACE IDENTIFICATION RESULT – STEP 4 95
TABLE 5.7 LONGITUDINAL STATE SPACE MODEL STRUCTURE ARRAYS TO IDENTIFY PHUGOID MODE 96
TABLE 5.8 LONGITUDINAL STATE SPACE IDENTIFICATION RESULT – STEP 5 96
TABLE 5.9 LATERAL-DIRECTIONAL STATE SPACE MODEL STRUCTURE ARRAYS 98
TABLE 5.10 FREQUENCY RANGE OF INTERESTS OF FREQUENCY RESPONSE PAIRS 99
TABLE 5.11 LATERAL/DIRECTIONAL STATE SPACE IDENTIFICATION RESULT – STEP 1 100
TABLE 5.12 LATERAL/DIRECTIONAL STATE SPACE IDENTIFICATION RESULT – STEP 2 100
TABLE 5.13 LATERAL/DIRECTIONAL STATE SPACE IDENTIFICATION RESULT – STEP 3 101
TABLE 5.14 LATERAL/DIRECTIONAL STATE SPACE IDENTIFICATION RESULT – STEP 4 101
TABLE 5.15 COMPARISON OF SHORT PERIOD MODES OF BOTH MODEL 116
TABLE 5.16 COMPARISON OF LATERAL/DIRECTIONAL MODES OF BOTH MODELS 116
TABLE A.1 EGI SPECIFICATIONS 126
TABLE A.2 TRANSDUCER SPECIFICATIONS 126
TABLE A.3 FCC SPECIFICATIONS 126
TABLE A.4 DATA LOGGER SPECIFICATIONS 127
TABLE A.5 DATA LINK SPECIFICATIONS 127

LIST OF FIGURES

FIGURES

FIGURE 1.1 EXPECTED MILITARY UAV REVENUES - EUROPE 3
FIGURE 2.1 SINUSOIDAL INPUT AND RESPONSE OF A SYSTEM 11
FIGURE 2.2 FOURIER TRANSFORMATION OF A SIGNAL [13] 13
FIGURE 2.3 OVERLAPPED HANNING WINDOWS [28] 17
FIGURE 2.4 FREQUENCY RESPONSE FUNCTION OF FIRST ORDER SYSTEM (1/S+1) 21
FIGURE 2.5 FIRST ORDER SYSTEM BODE PLOT 22
FIGURE 2.6 SECOND ORDER SYSTEM BODE PLOT 22
FIGURE 3.1 SPECIFICATIONS OF PELIKAN 24
FIGURE 3.2 THE BLOCK DIAGRAM OF EGI 25
FIGURE 3.3 CAD MODEL OF UAV 26
FIGURE 3.4 EXAMPLE OF AILERON IDENTIFICATION INPUT GIVEN IN THE FLIGHT TEST 28
FIGURE 3.5 ENERGY SPECTRA OF DOUBLET INPUTS [10] 29
FIGURE 3.6 FREQUENCY DOMAIN COMPARISONS OF STANDARD INPUTS [10] 30
FIGURE 3.7 1-2-1 AND DOUBLET INPUTS GIVEN IN THE FLIGHT TEST 31
FIGURE 3.8 THEORETICAL 1-2-1 AND DOUBLET 31
FIGURE 3.9 INPUT POWER SPECTRAL DENSITY COMPARISON 32
FIGURE 3.10 CONTROL SURFACE DEFLECTIONS DURING ELEVATOR SWEEP 35
FIGURE 3.11 CONTROL SURFACE DEFLECTIONS DURING ELEVATOR VERIFICATION INPUTS 35
FIGURE 3.12 CONTROL SURFACE DEFLECTIONS DURING AILERON SWEEP 36
FIGURE 3.13 CONTROL SURFACE DEFLECTIONS DURING AILERON VERIFICATION INPUTS 36
FIGURE 3.14 CONTROL SURFACE DEFLECTIONS DURING RUDDER SWEEP 37
FIGURE 3.15 CONTROL SURFACE DEFLECTIONS DURING RUDDER VERIFICATION INPUTS 37
FIGURE 3.16 FILTERED (SM) AND CORRECTED (CR) VALUES - ELEVATOR SWEEP 43
FIGURE 3.17 FILTERED (SM) AND CORRECTED (CR) VALUES – AILERON SWEEP 44
FIGURE 3.18 FILTERED (SM) AND CORRECTED (CG) VALUES – RUDDER SWEEP 44
FIGURE 4.1 FLOWCHART OF TRANSFER FUNCTION MODELING 48
FIGURE 4.2 EXAMPLE TRANSFER FUNCTIONS FOR TIME DELAY EFFECT 53
FIGURE 4.3 ANGLE OF ATTACK RESPONSE TO ELEVATOR INPUT (AOA/ΔE) 61

FIGURE 4.4 ROLL RATE RESPONSE TO AILERON INPUT (P/ΔA) CIFER RESULT 63
FIGURE 4.5 ROLL RATE RESPONSE TO AILERON INPUT (P/ΔA) SIMPE RESULT.....64
FIGURE 4.6 ROLL RATE RESPONSE TO AILERON INPUT (P/ΔA) 66
FIGURE 4.7 MAG, PHASE AND COHERENCE FUNCTIONS OF B/ΔR 68
FIGURE 4.8 SIDESLIP RESPONSE TO RUDDER INPUT (B/ΔR).....70
FIGURE 4.9 ROLL RATE RESPONSE TO AILERON INPUT (P/ΔA) 72
FIGURE 4.10 SIDESLIP RESPONSE TO RUDDER INPUT (B/ΔR).....73
FIGURE 4.11 SHORT PERIOD FREQUENCY REQUIREMENTS – CATEGORY B FLIGHT PHASE 76
FIGURE 5.1 COHERENCE VALUES OF RESPONSES OF LONGITUDINAL VARIABLES TO THROTTLE INPUT91
FIGURE 5.2 COHERENCE VALUES OF RESPONSES OF LONGITUDINAL VARIABLES TO ELEVATOR INPUT92
FIGURE 5.3 REGIONS OF IDENTIFIABILITY FOR LONGITUDINAL PARAMETERS [10] 92
FIGURE 5.4 SIMULINK MODEL FOR CALCULATING BIAS AND REFERENCE SHIFTS 103
FIGURE 5.5 LONGITUDINAL SS MODEL RESPONSES TO ELEVATOR SWEEP 105
FIGURE 5.6 LONGITUDINAL SS MODEL RESPONSES TO VERIFICATION INPUTS 106
FIGURE 5.7 ROLL RATE RESPONSES TO LATERAL/DIRECTIONAL INPUTS 107
FIGURE 5.8 YAW RATE RESPONSES TO LATERAL/DIRECTIONAL INPUTS.....108
FIGURE 5.9 Y ACCELERATION RESPONSES TO LATERAL/DIRECTIONAL INPUTS 109
FIGURE 5.10 SIDESLIP ANGLE RESPONSES TO LATERAL/DIRECTIONAL INPUTS 110
FIGURE 5.11 COMPARISON OF RESULTS AND FLIGHT DATA – RESPONSES TO IDENTIFICATION INPUTS 113
FIGURE 5.12 COMPARISON OF RESULTS AND FLIGHT DATA – RESPONSES TO VERIFICATION INPUTS .114
FIGURE 5.13 BODE PLOTS OF LONG. SS AND TF MODELS.....117
FIGURE 5.14 BODE PLOTS OF LAT. / DIR. SS AND TF MODELS.....117
FIGURE 5.15 COMPARISON OF SHORT PERIOD MODES OF BOTH MODELS 118
FIGURE 5.16 COMPARISON OF LAT/DIR MODES OF BOTH MODELS - ZOOMED DUE TO DIVERGENCE ..118

LIST OF ABBREVIATIONS

A/C	Aircraft
AoA	Angle of Attack
AoS	Angle of Sideslip
CAP	Control Anticipation Parameter
CG	Center of Gravity
CIFER	Comprehensive Identification from Frequency Responses Program
CR	Cramer-Rao
CZT	Chirp-Z Transform
DoD	Department of Defense
DoF	Degree of Freedom
EGI	Embedded GPS/INS
FAA	Federal Aviation Administration
FFT	Fast Fourier Transform
FPR	Flight Path Reconstruction
GPS	Global Positioning System
GUI	Graphical User Interface
HALE	High Altitude Long Endurance UAV
INS	Inertial Navigation System
LOES	Low Order Equivalent System
MALE	Medium Altitude Long Endurance UAV
MEMS	Microelectromechanical Systems
MIMO	Multi Input Multi Output
MTOW	Maximum Take-Off Weight
MUAD	Maximum Unnoticed Added Dynamics
MUAV	Micro UAV
NASA	National Aeronautics and Space Administration
OEM	Output Error Method
SimPE	Simulink Parameter Estimation
SISO	Single Input Single Output
TAI	Turkish Aerospace Industries, Inc.
TUAV	Tactical UAV
TUSAŞ	Türk Havacılık ve Uzay Sanayii A.Ş.
U.S	United States
UAV	Unmanned Aerial Vehicle

CHAPTER 1

INTRODUCTION

1.1 Background and Motivation

UAV is an acronym for Unmanned Aerial Vehicle and Unmanned Aerial Vehicle is defined by the Department of Defense (DoD) as [29]:

"Powered, aerial vehicles that do not carry a human operator, use aerodynamic forces to provide vehicle lift, can fly autonomously or be piloted remotely, can be expendable or recoverable, and can carry a lethal or nonlethal payload."

The countries, which operate UAV systems in 2009, are listed in Table 1.1[9].

Table 1.1 UAV Operator Countries in 2009

Algeria	Finland	Malaysia	South Africa
Argentina	France	Netherlands	South Korea
Australia	Germany	North Korea	Spain
Austria	Greece	Pakistan	Sweden
Bahrain	Hungary	Philippines	Switzerland
Belgium	India	Poland	Taiwan
Botswana	Iran	Qatar	Thailand
Bulgaria	Israel	Romania	Turkey
Canada	Italy	Russia	Ukraine
China	Japan	Saudi Arabia	United Arab Emirates
Czech Republic	Jordan	Singapore	United Kingdom
Egypt	Kuwait	Slovenia	United States of America

As seen in the table, many countries operate UAV systems since UAV systems have various advantages over manned aircrafts such as:

- A qualified pilot on board is not required
- UAV systems can work in environments that are dangerous to human life
- the exposure risk of the aircraft operator is reduced
- can stay in the air up to 30 hours, performing a precise, repetitive visualization of a region, in day or night and in any circumstances under computer control:
    - performing a geological survey
    - performing visual or thermal imaging of a region
    - measuring cell phone, radio, or, TV coverage over any terrain
- can be programmed to complete the mission autonomously even when contact with its ground control station is lost [30].

The UAV systems are used both civilian and military applications. UAVs are currently in use or under consideration around the world and in U.S. unrestricted airspace for such civil and commercial uses as [7]:

- Wildfire Detection and Management
- Pollution Monitoring
- Traffic Monitoring
- Disaster Relief
- Fisheries Management
- Pipeline Monitoring & Oil and Gas Security
- Meteorology - Storm Tracking
- Remote Aerial Mapping
- Transmission Line Inspection

The military applications of UAV systems are listed as:

- Surveillance and reconnaissance,
- Electronic warfare (early warning/electronic counter measures),
- Harassment,

- Relay command/control/communications,
- Terrain following/avoidance,
- Antisubmarine search,
- Surface attack,
- Formation flying,
- Weapon delivery,
- Air-to-air combat,
- Target acquisition,
- Interceptor, etc.

The adaptation to UAV system is satisfied more quickly and effectively in military applications. Especially, surveillance and reconnaissance capability provides real-time information and surface attack capability provides low cost attacks without the risk of personnel lost. In 2011, an expectation is made on military UAV revenues in Europe and the expected revenues are seen in Figure 1.1. This figure indicates that the UAV systems are seen as an important system in military applications.

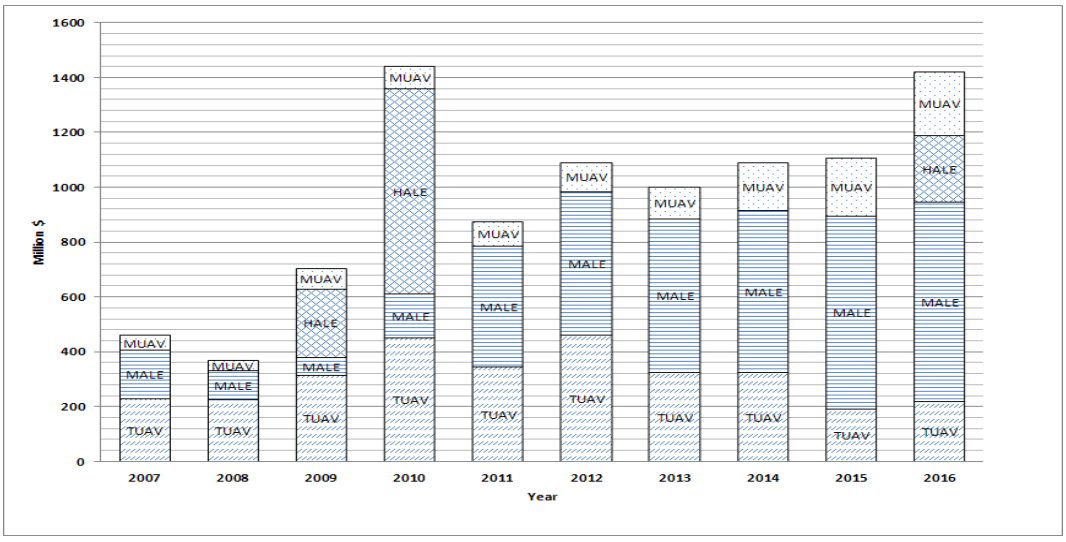

Figure 1.1 Expected Military UAV Revenues - Europe

The UAVs are classified according to their mission applications as:

- Target
- Strategic
- Combat
- Tactical
- Man-portable
- R&D
- Commercial

So far, the applications where UAV systems are used are listed. Recently, a new application area becomes popular. Nowadays, small UAVs are used as flight test platforms, especially in the domain of flight control research. Because of their compact size, low cost and reduced damage or harm risk in the failure situations, small UAV systems are very attractive as test platforms. An important task in the projects, where the UAVs are used as flight test platforms, is modeling and identifying the aircraft dynamics. Accurate models of UAV flight dynamics are generally unavailable due to the custom design and production of the airframes. However, such accurate models are required to characterize aircraft behavior and determine stability, control and performance properties.

The approaches generally applied to manned aircrafts and large UAVs to implement and validate the flight control systems are time consuming and high labor cost. Applying the same techniques to small UAVs is not productive. To make small UAV project low cost and complete the project in a short time commercial-off-the-shelf autopilots are used [6]. Most of these autopilots are tuned in flight by using ad-hoc method. This tuning in flight with ad-hoc method is time consuming and brings high risk. Moreover, tuning controller has limitations in performance optimality and robustness since it is performed in flight. To make development process faster and improve system reliability and robustness of the flight control system, it is important to develop verified accurate model of the UAV and system identification is practical and verified way of developing this model.

System identification has grown to a separate topic of the control theory and the examples of its successful utilization are found in many areas of practical applications. These are the cases where a verification of some mathematically described phenomena from the experimentally derived data is required. A more expanded description of the identification problem is given in [34]:

"Identification is the determination of the basis of input and output, of a system within a specified class of systems, to which the system under test is equivalent".

Iliff [1] provided a philosophical definition in contrast with the above technical definition as: "Given the answer, what are the questions, that is, look at the results and try to figure out what situation caused those results."

The process of system identification involves certain fundamental assumptions [10]:

"1. The true state of the dynamic system is deterministic.
2. Physical principles underlying the dynamic process can be modeled.
3. It is possible to carry out specific experiments.
4. Measurements of system inputs and outputs are available."

In flight vehicle development, it is a necessary step because system identification leads to adequately accurate and validated mathematical models of the flight vehicle, which are required to [10]:

"1. understand the cause-effect relationship that underlines a physical phenomenon,
2. investigate system performance and characteristics,
3. verify wind-tunnel and analytical predictions,
4. develop high-fidelity aerodynamic databases for flight simulators meeting FAA fidelity requirements,
5. support flight envelope expansion during prototype testing,
6. derive high-fidelity and high-bandwidth models for in-flight simulators,
7. design flight control laws including stability augmentation systems,
8. reconstruct the flight path trajectory, including wind estimation and incidence analysis,

9. perform fault-diagnosis and adaptive control or reconfiguration, and
10. analyze handling qualities specification compliance."

The motivation for this study is arisen from the research and development activities currently continuing in TAI.

1.2 Literature Review

A literature review given here mainly covers frequency domain system identification and its application to the aircrafts. There are many studies on system identification, so only the ones that cover related topics within the thesis are given in this part.

In a study, NASA F-18 High Alpha Research Vehicle was used to obtain low order equivalent system (LOES) modeling of bare airframe and flight control system of this vehicle [21]. Output error and equation error techniques were developed to identify the models using flight test data, and then the models were validated on simulation data. In the flight test, frequency sweep could not be applied due to time constraint. In this study, data requirements and flight test designs were also addressed. Unlike the study, in this thesis, both frequency sweeps and other inputs used in identification are performed although the time for test inputs are short, too. Moreover, both LOES and state space model of aircraft are formed.

A paper presents an approach used in input design and its analysis, identification of parameters and flying quality analysis [12]. The approach was applied on various Boeing transport and research aircrafts and the results are given as an example in the study. Piloted frequency sweeps were used as identification input in flight tests and CIFER® program is used for identification. The match between high order and low order frequency responses was checked using Maximum Unnoticed Added Dynamics (MUAD) Boundaries. Flying quality analysis is applied by specifying the Control Anticipation Parameter (CAP) using results of LOES method. Similar processes for transfer function modeling and handling quality analysis are followed in this thesis. In both studies, good matches are obtained between identified model and actual aircraft. Unlike the study, state space model of the aircraft is identified in this thesis.

In another study, a six-degree-of-freedom linear parameter varying (LPV) dynamic model of the UAV helicopter was obtained using MATLAB® and Simulink. The validation of model was done using CIFER® [4]. The data used in validation were obtained from flight tests, where frequency sweeps were applied as identification inputs. In the study, Thunder Tiger Raptor 50 UAV helicopter was used. A 2nd order Butterworth filter with a cutoff frequency of 6 Hz was used to filter the noise in the signals. In the study, flight test were not performed well, exact frequency sweeps were not applied. However, good match in pitch rate and roll rate is obtained but it is seen that a transfer function model is not enough to validate a helicopter model.

A fully autonomous, small and unmanned airplane used in flight tests to collect open loop data to perform system identification in another study [11]. Carrier-Phase Differential GPS was used to obtain position, velocity, attitude and attitude rate and in the test no inertial sensor was used. The only additional sensors were indicators of wind speed and direction. Three different identification techniques (Moshe Idan, Observer/Kalman Identification (OKID) Process, and Subspace) were applied to the same data and results were compared. The results show that the matches between predicted and real responses seem poor especially in roll angle and y-axis velocity.

1.3 Scope of Research

The scope of this work is divided into three parts:

The first is to perform flight test where proper excitations are obtained for identification. This part covers the test input design. Corrections due to bias and noise in the signal are also addressed. In addition, cg location corrections are applied to acceleration measurement.

The second is to form transfer function models of the UAV using flight test data. To obtain transfer function model, firstly, the necessary model structure determination is obtained. Then, the model structure parameters are estimated.

The third is to form state space model of the UAV using flight test data. To obtain state space model, firstly, model structure determination is done using Cramer-Rao bounds and insensitivity values. Then, the parameters in the determined state space structure are estimated.

1.4 Research Objective

The objective of this study is to obtain accurate and verified models of the UAV from both transfer function and state space model identification techniques using flight test data. The importance of this objective arises from the necessity and advantages of having accurate aircraft model especially in flight control system design since an accurate model satisfies improvements on robustness requirements of the autopilot and this makes possible to obtain a high performance autopilot. More importantly, an accurate model of aircraft simplifies the tuning process of flight control system gains in flight; therefore, number of time consuming flights, risk of losing aircraft control, and the cost are reduced.

1.5 Thesis Outline

The present study is composed of six chapters; each is summarized as follows:

Chapter 1 is an introductory part, which puts forward the motivation and aim of this study, supplies the definition and properties of UAVs in general stressing on the UAV type specific to this study, and briefly gives some system identification application. The published studies in literature including the system identification and aircraft modeling are reviewed and discussed, and finally the research scope and objectives are given.

Chapter 2 presents the mathematical background, which covers frequency response function, Fourier transform, spectral functions, supplies definitions and calculations of frequency response.

In chapter 3, the data gathering and reconstruction is presented. In this chapter, identification and verification input designs are discussed and obtained results are checked whether they are kinematically consistent. Bias and scale factor corrections are done and data are reconstructed.

In chapter 4, transfer function identification is carried out. In this chapter, longitudinal and lateral/directional transfer functions are obtained using flight test data. In transfer function modeling, model structure determination plays important role. The steps applied to obtain proper model structure, which covers input-output

pairs, and frequency ranges, order of numerator and denominator, equivalent time delay, are discussed. Then parameter estimation is applied to obtain coefficients of transfer function models. For many applications these rather simple transfer function models are found to be quite sufficient, including handling qualities analysis, actuator and other subsystem models.

Chapter 5 covers a state space modeling part, which presents the basic concepts and identification of state space model of the UAV. An important assessment of model fidelity, robustness and limitations of identified model are checked by using verification inputs such as doublets. After determining biases and offsets of the identified state space model, this model is compared with the flight data.

Chapter 6 is the conclusion part of the study, which summarizes the whole performed study, and gives conclusions derived from the results of the study and gives examples of possible future works.

CHAPTER 2

MATHEMATICAL BACKGROUND

2.1 Frequency Response Theory

From differential equations, it is known that if a linear system is driven by a forcing function, such as a sine wave with a frequency (ω_0) and a period (T_0) the system will produce a transient response and a steady-state response. After a period of time, the transient response will damp out if the system is stable, leaving the steady-state response, which is solely due to the forcing function. Examples of a forcing function and the system steady-state response in time history are depicted in the Figure 2.1.

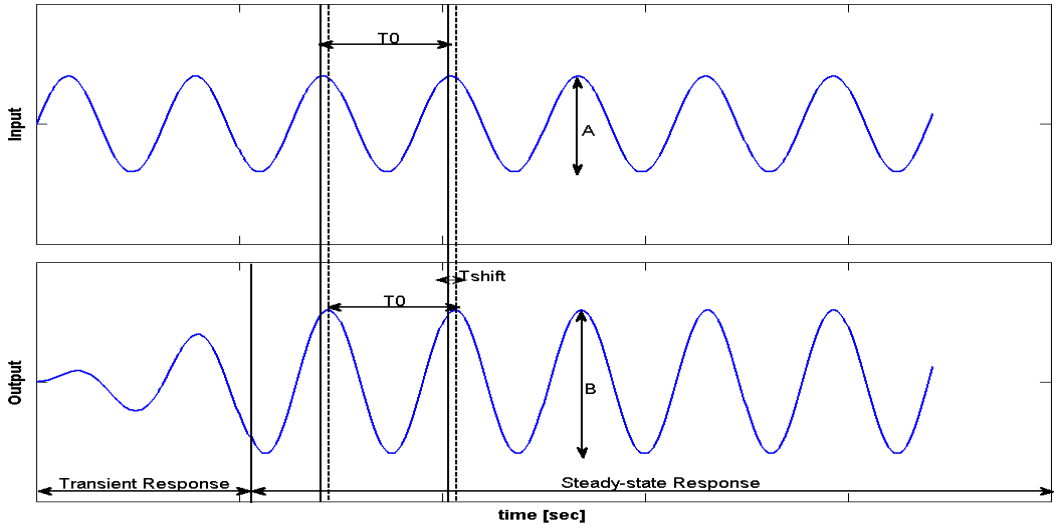

Figure 2.1 Sinusoidal Input and Response of a System

The periodic input used to excite the system is given as [3]:

$$x(t) = Asin(\omega t) \tag{2.1}$$

As stated, after a period of time, the transient response will die out and the system output will be also periodic function with same frequency but with different amplitude and a phase shift [3]:

$$y(t) = Bsin(\omega t + \varphi) \tag{2.2}$$

Frequency domain identification methods are based on spectral analysis in which frequency response functions are derived from time history data. Frequency response functions describe the characteristic of the system as a function of frequency, which is a complex-valued function that relates the Fourier Transform of the inputs and outputs of the system. In the light of these expressions, the frequency response function is expressed as [28]:

$$H(f) = \frac{Y(f)}{X(f)} \tag{2.3}$$

where

$H(f)$: Frequency response function

$X(f)$: Fourier transform of $x(t)$ $\quad X(f) = \int_{-\infty}^{+\infty} x(t)e^{-i2\pi ft}dt$

$Y(f)$: Fourier transform of $y(t)$ $\quad Y(f) = \int_{-\infty}^{+\infty} y(t)e^{-i2\pi ft}dt$

Further expressions of frequency response functions are obtained by using features of being complex-valued function [28]:

$$H(f) = H_R(f) + H_I(f) \tag{2.4}$$

$$|H(f)| = \sqrt{H_R^2(f) + H_I^2(f)} \tag{2.5}$$

$$\varphi(f) = \angle H(f) = tan^{-1}\left[\frac{H_I(f)}{H_R(f)}\right] \tag{2.6}$$

where

$H_R(f)$: Real component of $H(f)$ $\quad H_R(f) = \int h(t)\cos(wt)\,dt$

$H_I(f)$: Imaginary component of $H(f)$ $H_I(f) = \int h(t)\sin(wt)\,dt$

$|H(f)|$: Amplification factor

$\angle H(f)$: Phase shift

2.1.1 Fourier Transform

The Fourier transform, named after Joseph Fourier, is a mathematical transform, which is used for transforming a function in time domain to frequency domain. The Fourier transform is an extension of the Fourier series that results when the period of the represented function is lengthened and allowed to approach infinity [17].

The Fourier transform relates time domain of the function, to frequency domain of the function. The component frequencies, spread across the frequency spectrum, are represented as peaks in the frequency domain, as seen in Figure 2.2.

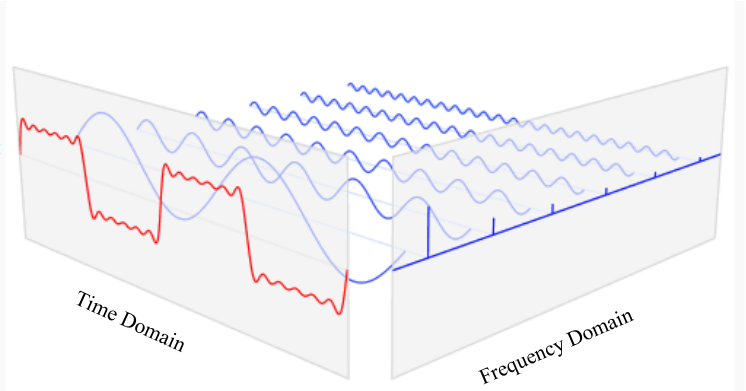

Figure 2.2 Fourier Transformation of a Signal [13]

Fourier transform is defined for t= -∞ to +∞ [3]:

$$X(f) = \int_{-\infty}^{+\infty} x(t)e^{-i2\pi ft}dt \tag{2.7}$$

However, in the experiment, data samples last from t=0 to t=T. Therefore, finite Fourier transform is used in this study [3]:

$$X(f,T) = \int_{0}^{T} x(t)e^{-j2\pi ft}dt \tag{2.8}$$

The expression in Eqn. (2.8) is valid for continuous time; however, since data are collected with instruments at a certain sample rate, data samples are formed by a bunch of discrete time points. Therefore, it is leading to discrete Fourier transform [3]:

$$X(f_k) = X(k\Delta f) = \Delta t \sum_{n=0}^{N-1} x_n e^{-j2\pi(kn)/N} \tag{2.9}$$

where

N : number of discrete frequency points

$X(f_k)$: Fourier coefficients, for $k = 0,1, \dots, N-1$

x_n : time history data record, for $n = 0,1, \dots, N-1$

Δt : increment in time

Δf : frequency resolution

2.1.2 Spectral Functions

The input autospectrum, also called as input power spectral density, indicates the distribution of the squared input, excitation power, as a function of frequency [28]. Eqn. (2.10) shows the one-sided spectral function.

$$\tilde{G}_{xx}(f) = \frac{2}{T}|X(f)|^2 \tag{2.10}$$

The output autospectrum, also referred as output power spectral density, indicates the distribution of the squared output, response power, as a function of frequency [28]. Eqn. (2.11) shows the one-sided spectral function.

$$\tilde{G}_{yy}(f) = \frac{2}{T}|Y(f)|^2 \tag{2.11}$$

The cross spectrum, also referred as cross power spectral density, displays the distribution of the product of input and output, input-to-output power, as a function of frequency [28]. Eqn. (2.12) shows the one-sided spectral function.

$$\tilde{G}_{xy}(f) = \frac{2}{T}[X^*(f)Y(f)] \tag{2.12}$$

Using these equations, frequency response function is obtained in Eqn. (2.13):

$$H(f) = \frac{\hat{G}_{xy}(f)}{\hat{G}_{xx}(f)} \; or \; H(f) = \frac{\hat{G}_{yy}(f)}{\hat{G}_{yx}(f)} \tag{2.13}$$

Both expressions in Eqn. (2.13) give the same result when there is no measurement noise.

Using these spectral functions, the coherence function is obtained in Eqn. (2.14). The equation in which coherence function γ is obtained using spectral functions is given in Eqn. (2.14) [28]:

$$\hat{\gamma}_{xy}{}^2(f) = \frac{\left|\hat{G}_{xy}(f)\right|^2}{\left|\hat{G}_{xx}(f)\right|\left|\hat{G}_{yy}(f)\right|} \tag{2.14}$$

The detail explanations of coherence equations will be given in Section 2.2.

2.2 Calculation of Frequency Response

In this study, frequency responses are obtained by using FRESPID module of CIFER®. This module gets the time history data and filters it digitally to eliminate high frequency noises, and then apply overlapped windowing method to reduce random error [28]; after that, this time history data are transformed into frequency domain using Chirp-Z transformation and spectral functions are obtained. Finally, using these spectral functions, coherence functions and frequency response functions and their Bode plots are obtained to be used in frequency domain system identification.

In this part, the methods used in calculation of frequency response are covered, such as; windowing, chirp-z transformation, coherence functions and Bode plots which are performed by the CIFER® software.

2.2.1 Windowing

Windows are weighting functions applied to data to reduce the spectral leakage. The spectral leakage is defined as spreading of frequency content of signal on frequencies lying near that frequency, due to the fact that the signal is not periodic. If there is a leakage, the amplitude of frequency content is smaller than it should be.

In this study overlapped Hanning window is used. Hanning window works by weighting the start and end parts of data to zero while increasing the amplitude of the signal at the center to maintain the average amplitude of the signal. The increment in amplitude is implemented using following equation:

$$w(n) = 0.5\left(1 - \cos\left(\frac{2\pi n}{N-1}\right)\right) \tag{2.15}$$

where n is *n=0, 1… N-1* and *N* is number of sample elements.

Overlapping the windows (periodograms) greatly reduces the random error by averaging the rough estimates in multiple segments of data [28]. The random error is estimated by using Eqn. (2.16). As seen in the equation the number of overlapped window, n_d, is inversely proportional with random error:

$$\varepsilon_r = C_\varepsilon \frac{\left[1 - \gamma_{xy}^2\right]^{1/2}}{|\gamma_{xy}|\sqrt{2n_d}} \tag{2.16}$$

where

C_ε is a constant to take window overlap into account (for a 50% window overlap $C_\varepsilon = \sqrt{0.55}$)

n_d is the number of non-overlapping time history averages ($n_d = T_{rec}/T_{win}$)

Another important parameter in windowing is the total number of overlapped window, which is calculated by:

$$n_r = 1 + \left[\frac{(T_{rec}{}'/T_{win}) - 1}{1 - x_{frac}}\right] \tag{2.17}$$

where

T_{win} : width of window

$T_{rec}{}'$: extended record length to the end of the last window (Figure 2.3)

x_{frac} : overlap fraction, it takes values within a range of 0 to 1

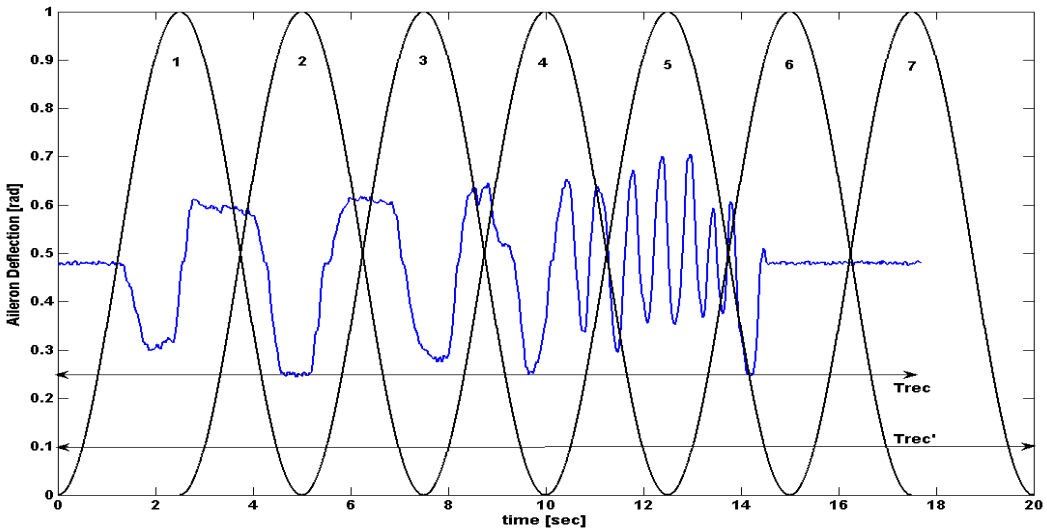

Figure 2.3 Overlapped Hanning Windows [28]

In Figure 2.3, overlapped windows applied to the aileron sweep taken from flight test data are given as an example. The time history data is segmented into n_r overlapped windows, which have T_{win} period and contain L points. In the figure, 50% overlap of $n_r = 7$ windows is shown. The time history data in each window are weighted by the window shaping function $\omega\ (t)$; in this study, Hanning window shaping is used.

After applying the overlapped Hanning windows, the smooth estimate spectral functions are obtained by using Eqns (2.18), (2.19), and (2.20) [28]

$$\hat{G}_{xx}(f) = (\frac{1}{Un_r}) \sum_{k=1}^{n_r} \tilde{G}_{xx,k}(f) \tag{2.18}$$

$$\hat{G}_{yy}(f) = (\frac{1}{Un_r}) \sum_{k=1}^{n_r} \tilde{G}_{yy,k}(f) \tag{2.19}$$

$$\hat{G}_{xy}(f) = \left(\frac{1}{Un_r}\right) \sum_{k=1}^{n_r} \tilde{G}_{xy,k}(f) \tag{2.20}$$

U is the correction value used to put the energy loss, due to weighting, into the calculations. For Hanning window this value is equal to 0.612 [28].

In the theory of frequency, since it is reciprocal of period, the minimum frequency is defined as reciprocal of maximum period, which is window length, T_{win}; however, in reality, it is not applicable due to noise in input and output signals, nonlinearities and contributions from secondary inputs etc. According to Tischler, obtaining satisfactory coherence is available at twice of theoretical minimum frequency, which is named as minimum effective frequency. Therefore, the nominal window size is given as twice of the longest period of interest [28]:

$$T_{win_{nom}} = 2T_{max} \tag{2.21}$$

Although maximum window size is limited with individual record length T_{rec}, experiments show that it is limited with half of the individual record length T_{rec} [28].

$$T_{win_{max}} \leq 0.5T_{rec} \tag{2.22}$$

Minimum window size should provide at least a decade of data bandwidth between the minimum effective frequency and maximum frequency of interest. Therefore minimum window size is expressed as [28]:

$$T_{win_{min}} \geq 20\frac{2\pi}{\omega_{max}} \tag{2.23}$$

2.2.2 Chirp-Z Transform

Chirp-Z Transform (CZT) is a specialized implementation of the Fast Fourier Transform (FFT), and the advantages of CZT are covered in this section.

Unlike FFT, Chirp-z transform is not required N=L equality, where N is number of discrete frequency points and L is number of time history points in a spectral window. In Chirp-z transform, two criteria are satisfied that N≤L and N+L is power of 2. Therefore, Chirp-z is more flexible than FFT [28].

Although FFT distributes its N frequency points to a unit circle, N frequency points of CZT is distributed to over an arbitrary arc of unit circle. Therefore, the frequency resolution of CZT is more than FFT [28].

Another advantage of CZT is that CZT has reduced leakage and improved accuracy [25].

2.2.3 Coherence Function

Coherence function is a key indicator of the frequency response accuracy as a function of frequency. The coherence function indicates whether the system excited satisfactorily across the operating range of frequency also it indicates whether system being modeled can be characterized as linear model in this frequency range [28]. This indication is obtained using Eqn. (2.24):

$$\hat{\gamma}_{xy}{}^{2}(f) = \frac{\left|\hat{G}_{xy}(f)\right|^{2}}{\left|\hat{G}_{xx}(f)\right|\left|\hat{G}_{yy}(f)\right|} \tag{2.24}$$

When, Eqn. (2.24) is examined, it is seen that the coherence function does not depend on parametric model structure. The coherence function takes values in a range of 0 to 1. The value of 1 indicates that the relation of input and output spectrum is perfectly linear. In applications, it is not a real case; the coherence function value is smaller than 1 due to following reasons [28]:

1. Noise in measured outputs reduces the coherence.
2. The system responses to input signals can contain nonlinearities; therefore, perfect representation of system characteristic using frequency response function is not available.
3. Process noise due to unmeasured inputs such as gust or other control inputs not used in identification or not measured reduces the coherence.

In the system identification, in the interested frequency range it is desired that the coherence is higher than 0.6 [28].

$$\gamma_{xy}{}^2 \geq 0.6 \tag{2.25}$$

2.2.4 Bode Plots

Since the representation of frequency responses (complex functions) are difficult in graphs, which is shown in Figure 2.4, three plot types are used in representation of frequency responses:

- Bode diagrams
- Nyquist plot
- Log-magnitude versus phase plot

In Figure 2.4, solid curve shows the values of frequency response H(jω) at frequencies, ω, and dot and dashed curves are projections of solid curve and show changes in imaginary and real parts of frequency response, H(jω) with respect to frequency. As seen in this figure, it is difficult to deduce the characteristics of H(jω) from the graph.

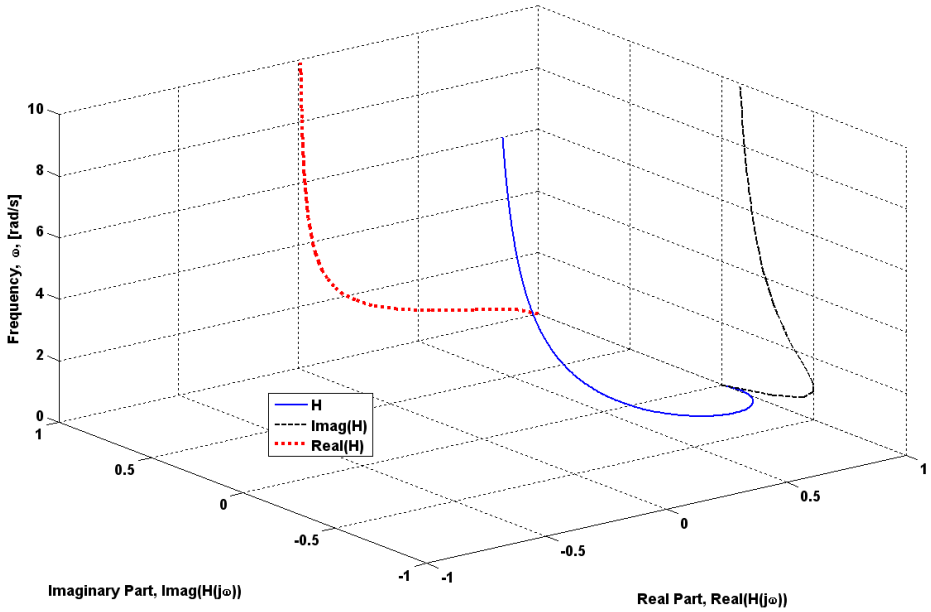

Figure 2.4 Frequency Response Function of First Order System (1/s+1)

In this study, bode diagrams are used to represent the frequency response functions. In bode diagrams, the frequency response is represented as two curves, one is the magnitude in dB versus logarithm of frequencies, and other is the phase angle in degrees versus log of frequencies. Usage of bode plot gives some advantages such:

- Bode plots have additive feature in series.
- Wide frequency range of system response can be displayed in Bode plots.
- Bode plots determined through an experiment present response of the system as a linear approximation without any assumptions about system order.

The magnitude and phase curves give characteristics of system according to poles and zeros in transfer function. If there is a zero in transfer function, it behaves like differentiator and caused +20dB/decade magnitude slope, and +90° degree phase shift. Moreover, if there is a pole in transfer function, it behaves like integrator and caused -20dB/decade magnitude slope and -90° degree phase shift.

In the Figure 2.5 and Figure 2.6, bode plots of first order systems and second order systems are given as an example.

The magnitude curves are drawn by calculating the magnitude for each frequency ω, using Eqn. (2.26):

$$H_{dB} = 20\log_{10}|H(j\omega)| \tag{2.26}$$

The phase curves are drawn by calculating the magnitude for each frequency ω, using Eqn. (2.27):

$$H_{deg} = \tan^{-1}\frac{real(H(j\omega))}{imag(H(j\omega))} \tag{2.27}$$

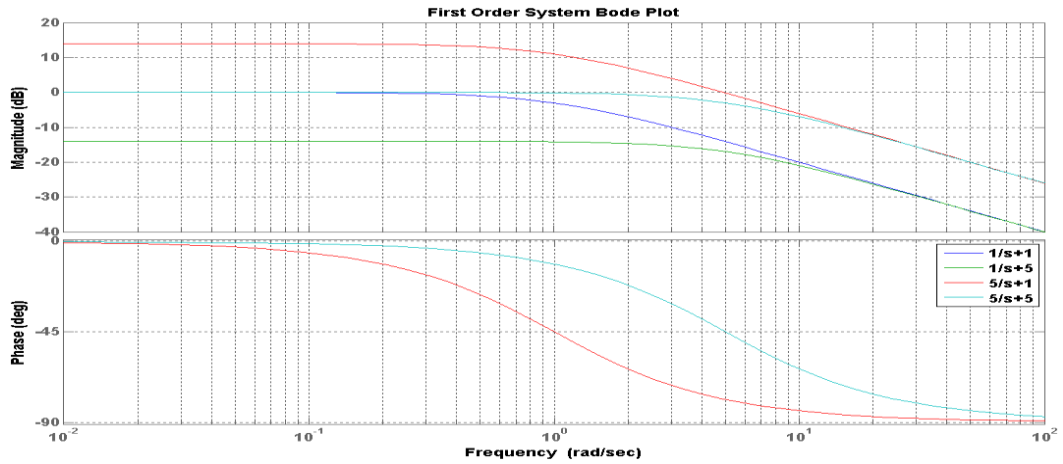

Figure 2.5 First Order System Bode Plot

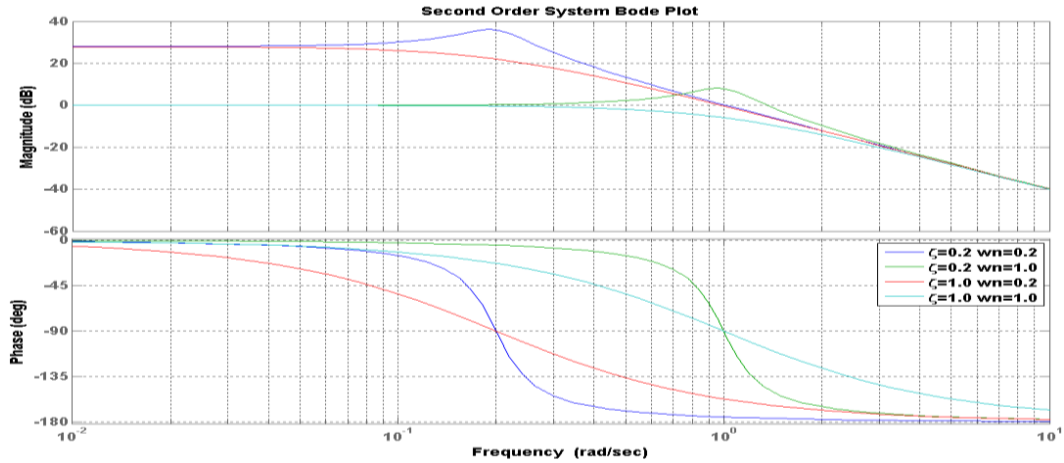

Figure 2.6 Second Order System Bode Plot

CHAPTER 3

DATA GATHERING & RECONSTRUCTION

3.1 Introduction

This chapter presents the collection of the time history database and its consistency analysis. The quality of the end product of identification process depends on [28]:

- Properly selected instrumentation system
- Properly designed and executed flight tests
- Properly removed kinematic inconsistencies

The main principle in system identification is that the flight test records must have the information about the dynamics, which will be identified. This condition is provided by selecting proper instrumentation system, planning flight test to excite the system properly, and checking the consistency of the data obtained in the flight tests.

3.2 Platform & Instrumentation

3.2.1 Platform

Pelikan, used in this study, is a TAI developed and instrumented test platform for developing system identification models and flight control systems for UAVs. It has high-wing configuration, 2 piston-prop engines (1 pusher, 1 tractor), tricycle landing gear system and boom mounted tail arrangement. The specifications and a sketch of Pelikan are given in Figure 3.1.

Parameter	Value
Length	3,3 m
Wing Span	4,0 m
Wing Chord	0,39 m
Wing Area	1,5 m^2
MTOW	65 kg
Max. Speed	80 kias
Ixx	16 kgm^2
Iyy	40 kgm^2
Izz	55 kgm^2

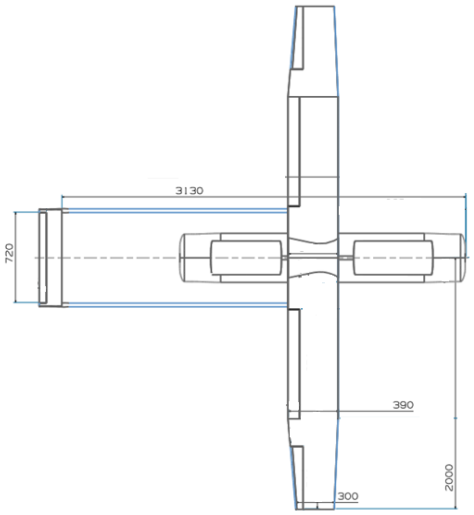

Figure 3.1 Specifications of Pelikan

3.2.2 Instrumentation

In identification, it is known that, "If it is not in the data, it cannot be modeled" [28]. This basic rule makes input design and instrumentation for flight tests important. The importance of instrumentation arise from that the quality of sensor specifies the data characteristics like accuracy, noise, etc. In addition, some features of data recording, such as sample rate and filtering are important since they directly affect the available information in the data. According to Shannon's sampling theorem, sample rate is at least twice of the maximum frequency presented in the signal; however, in reality more than that is necessary. The filters utilized may cause unreal phase resulting into estimated parameters with bias [28]. Therefore, in Pelikan, digital filters with same cut-off frequency are applied to all sensor measurements:

- GPS/INS (EGI) – 50 Hz
- Air Data Boom – 50 Hz
- Servo Commands – 50 Hz
- Servo Encoder – 50 Hz

The measured variables are listed in Table 3.1 :

Table 3.1 List of Measured Quantities

	Measured Quantity		Measured Quantity		Measured Quantity		Measured Quantity
EGI Data	a_x	**Pilot Commands**	Aileron Command	**Air Data**	V	**Servo Encoder**	Left Aileron Position
	a_y		Elevator Command		AoA		Right Aileron Position
	a_z		Rudder Command		AoS		Left Elevator Position
	p		Throttle Command		h		Right Elevator Position
	q						Left Rudder Position
	r						Right Rudder Position
	Φ						
	Θ						
	ψ						

GPS/INS:

The GPS/INS system used in A/C includes a MEMS based Inertial Measurement Unit (INS), a GPS receiver and a pressure sensor. In addition, this system has a built in Extended Kalman Filter. In Figure 3.2, the block diagram of EGI is given:

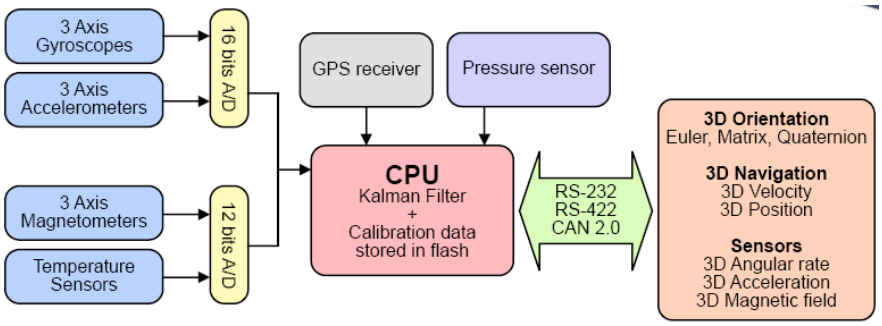

Figure 3.2 The Block Diagram of EGI

Air Data Test Boom:

Air data test boom has total and static pressure ports, angle of attack and angle of sideslip vanes. Its shape and the location on the A/C are presented in Figure 3.3. Detailed explanations about instrumentation systems and other equipment are given in Appendix A.

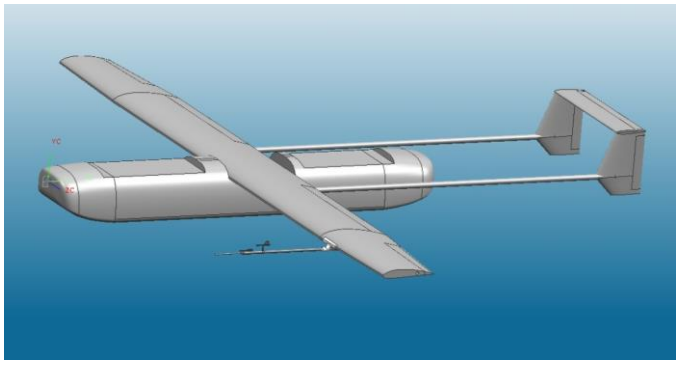

Figure 3.3 CAD model of UAV

3.3 Input Design

The inputs used in frequency domain are separated in two main parts:

- Inputs used for identification
- Inputs used for verification

Inputs used for identification are generally frequency sweeps for frequency domain system identification. If it is not applicable, several multi-inputs like 3-2-1-1 input or doublets may be applied in series [22].

Inputs used for verification are generally doublets, multi inputs like 3-2-1-1 and 1-2-1. The important thing for verification inputs is that they must be dissimilar than inputs used in identification to ensure that the identified model is accurate and robust [33].

The detailed explanations of input types are given in Section 3.3.2.

The flight testing for frequency domain data acquisition is designed to provide frequency sweeps for selected input-output pairs at about a given trimmed flight condition over frequency range of interest [33]. Frequency range of interest is the range over which the identified model is expected to be valid.

3.3.1 Identification Inputs

In this part, frequency sweeps, which are generally used as identification inputs in frequency domain identification, are discussed. Frequency sweep refers to a class of control inputs that has a quasi-sinusoidal shape of increasing frequency.

Tischler remarks four important points while planning frequency sweep tests [28]:

1. Before and after frequency sweeps, there are nearly 3s trim durations to get trim states of control inputs and responses
2. The frequency sweep starts with two long period control inputs to get data about low frequency dynamics like phugoid.
3. In frequency sweep, the increase in frequency is performed smoothly to prevent rushing through mid-frequencies.
4. While applying frequency sweeps, the aircraft oscillations are roughly symmetric and responses are near trim values. Aircraft responses in the range of ±5-15 deg in angular attitudes and ±5-15 deg/s in angular rates and ±5-10kts in velocity and the inputs in the range of ±10-20% of control input are intended to obtain in frequency sweeps.

In flight tests of Pelikan, there are practical constraints while applying frequency sweeps. For a racetrack pattern, the flight leg where identification tests are performed is 25 seconds long. Therefore, a sweep is performed in 25 seconds. The trim duration takes 5 seconds therefore the frequency sweeps lasts nearly 20 seconds.

While applying frequency sweep input, exact sinusoidal input shape is not required also is not desirable since irregularities ensure a broader bandwidth of excitation, and non-repeatability of the input waveform improves the overall information content when concatenated sweep records are formed [28]. However, for long period inputs, input shape quite important since the aircraft responses can be diverged from trim condition. In Figure 3.4, the data obtained from the encoder of the aileron while frequency sweep is being applied are shown as an example of identification input applied in the flight tests.

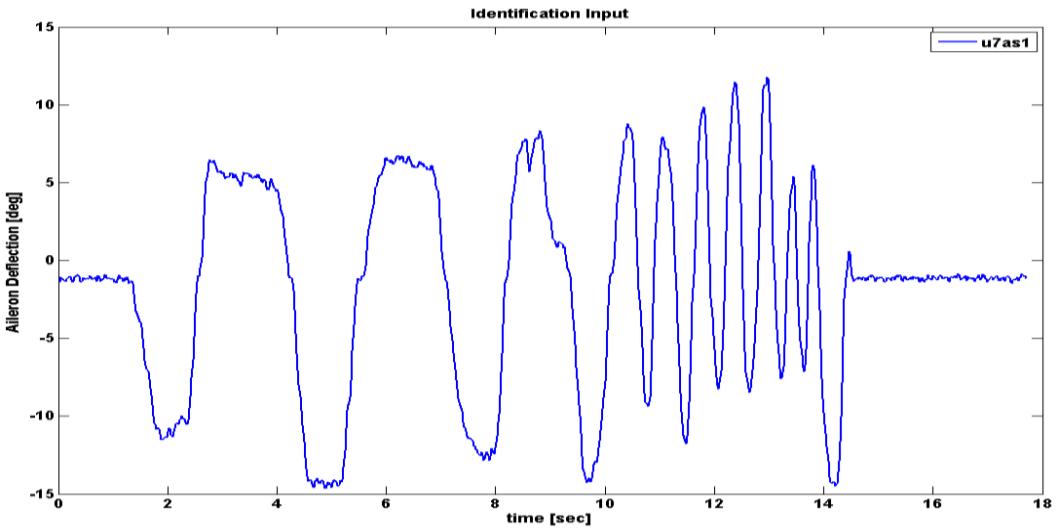

Figure 3.4 Example of Aileron Identification Input Given in the Flight Test

3.3.2 Verification Inputs

The aims of the verification are [28]:

- to check the accuracy of the identified model by comparing the estimated responses and measured flight data.
- to check the robustness of the identified model by comparing the estimated responses and measured flight data.

The identification input is also used for accuracy verification; however, for robustness analysis dissimilar inputs must be used. In this study, doublets and 1-2-1 multi inputs are used as dissimilar inputs. These types of inputs are generally used in time domain system identification. The main differences of this type of inputs from frequency sweeps are [7, 19]:

- Frequency sweeps are not time efficient when these inputs are concerned
- Frequency sweep moves smoothly, on the other hand, these inputs are applied by moving controls abruptly
- Frequency sweep has not a part where control stick is constant except trim durations; however, these inputs keep fixed for a time Δt, which determines the excited frequency.

- Since these inputs are not sweeps, the excited frequency range is very narrow.

Doublet Inputs:

Doublets are applied by moving control abruptly in one direction, then the input is kept fix for a certain time Δt, after that control moved abruptly to other direction, after waiting one more Δt time, the control moves to neutral position. The doublet input, which is a two-sided pulse, results in a symmetrical signal, having energy concentrated at a frequency, which varies with Δt. The variation shows in Figure 3.5.

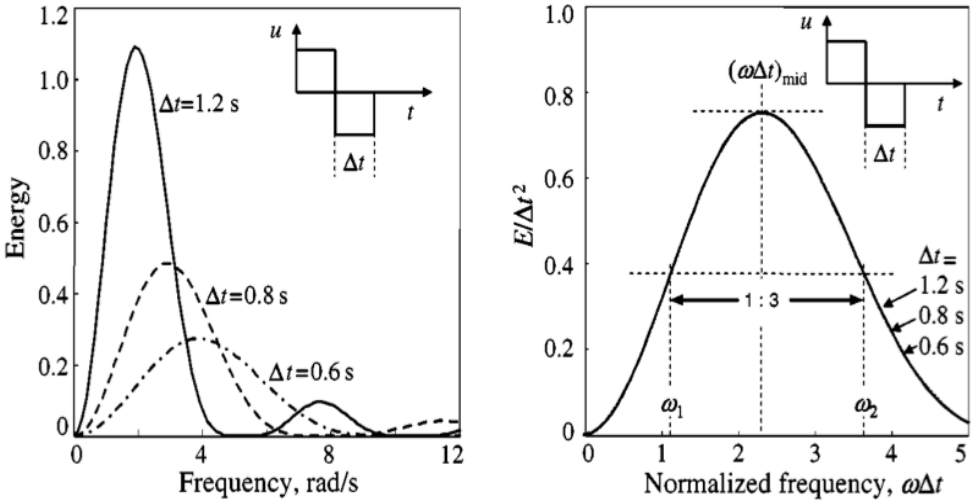

Figure 3.5 Energy spectra of doublet inputs [10]

In Figure 3.5, energy spectrum changes of the input signal according to Δt value of the doublet are shown. Jategaonkar gives a detailed explanation about energy spectrum and a code to obtain graphs given in Figure 3.5 [10]. As seen in Figure 3.5, the highest energy content in the signal is reached at a normalized frequency, ωΔt of 2.3. This means that the aircraft response obtained with this input signal represents the aircraft characteristics at the frequency range where the highest energy content is reached. Therefore, doublet input is designed according to desired frequency, ω, which is roughly 2.3/Δt. There is a practical constraint that exact shape of doublets cannot be obtainable in flight tests since doublet cannot be applied as sharp as given

in Figure 3.5. An example of the doublets applied in Pelikan flight test is given in Figure 3.7, obtained using the encoder data of aileron deflections.

3-2-1-1 Inputs:

Extending the logic that progressing from single-step input to two-step input (doublet) leads to a spread of the power spectrum; therefore, much broader band signal is achieved through a multistep input. 3-2-1-1 is one of the multistep inputs and it is 7Δt long and includes positive and negative equal amplitude steps. The comparison of energy spectra of inputs is given in Figure 3.6. In that graph, how the input signal type affects the change in energy spectrum of the input signal.

1-2-1 Inputs:

This input type uses a time step, which is half of that of the doublet, to get excitation at a frequency; therefore, it becomes possible to shift the energy spectrum to higher frequencies. 1-2-1 input is generally used for lateral system identification, especially for aileron inputs [10]. In Figure 3.7, first subplot shows aileron 1-2-1 input applied in flight test and second subplot shows aileron doublet.

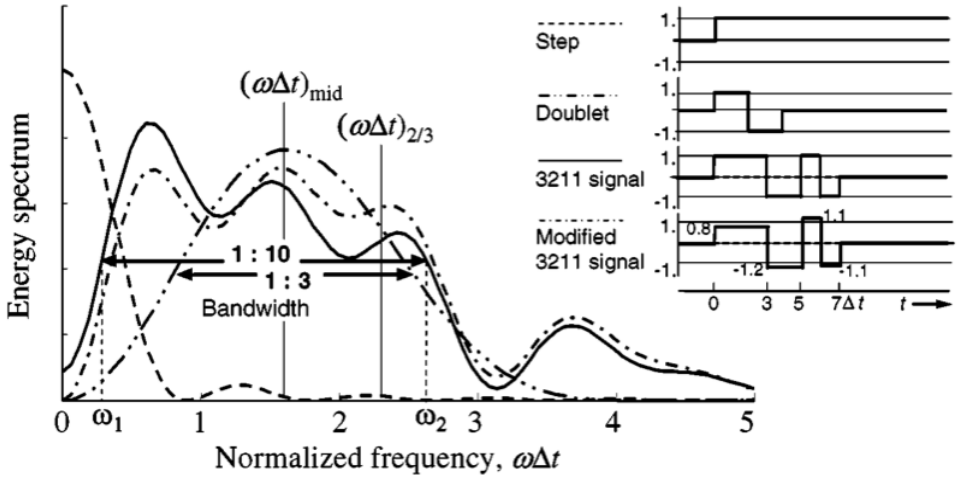

Figure 3.6 Frequency domain comparisons of standard inputs [10]

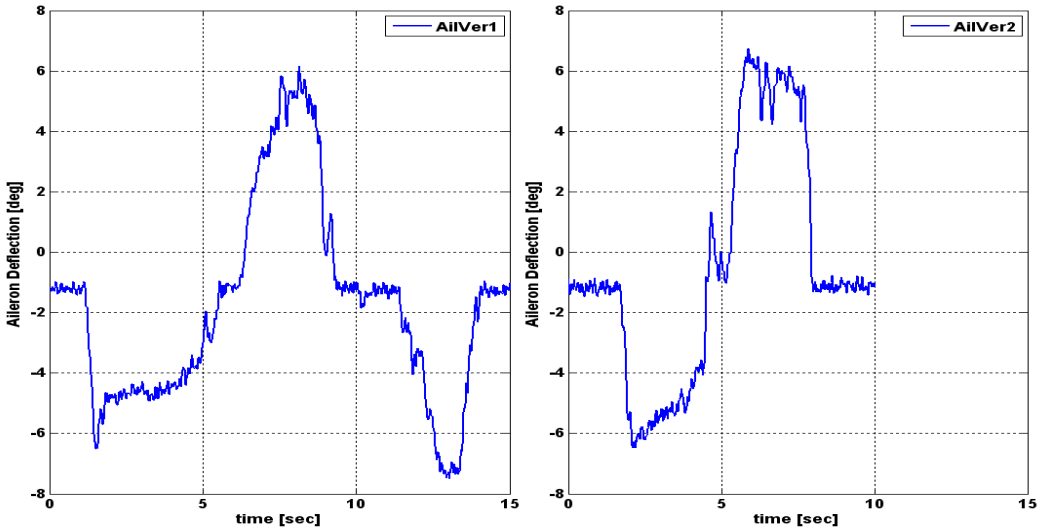

Figure 3.7 1-2-1 and Doublet Inputs Given in the Flight Test

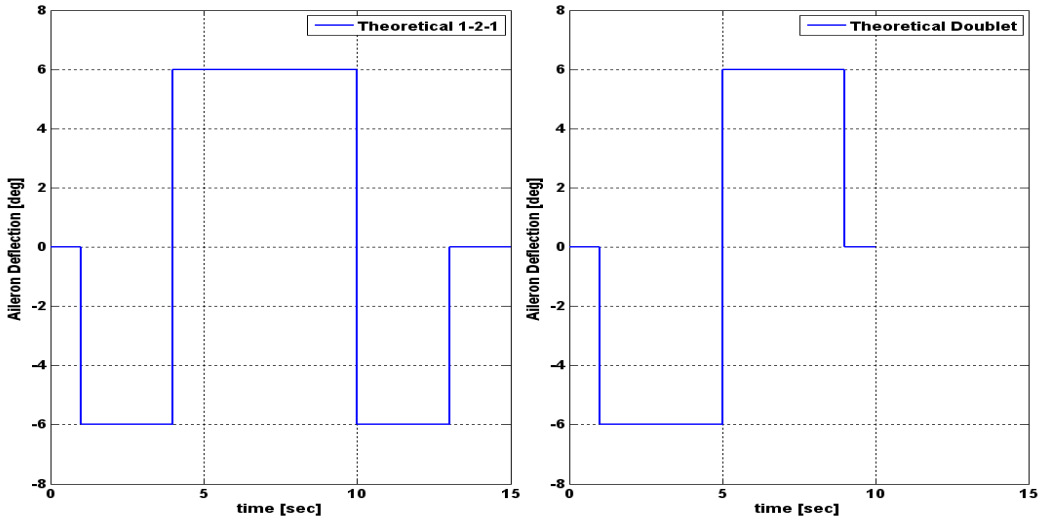

Figure 3.8 Theoretical 1-2-1 and Doublet

As seen in Figure 3.7, the verification inputs obtained in flight tests are not similar with the theoretical ones which are given in Figure 3.8. The differences between two figures occur due to two reasons: pilot and servo. Jategaonkar states that the inputs have not sharp edges since pilots behave like a filter [10]. The other reason of the differences between them is since the values given in Figure 3.7 are control surface deflections, these values includes effects of servo dynamics.

Therefore both linear and nonlinear (rate limiting) characteristics of servo dynamics prevent getting sharp inputs like given in Figure 3.8.

Since the designed inputs were not obtained in the flight tests, to check the effects of this dissimilarity in verification inputs, the input power spectral density of the inputs, performed in the flight test, and the theoretical inputs are checked. The comparison of input power spectral density is given in Figure 3.9 indicates excitation power as a function of frequency. As seen in Figure 3.9, the 1-2-1 input applied in the flight test has as much excitation power as theoretical one and the doublet has some less power than its theoretical value, but generally their excitation powers are close.

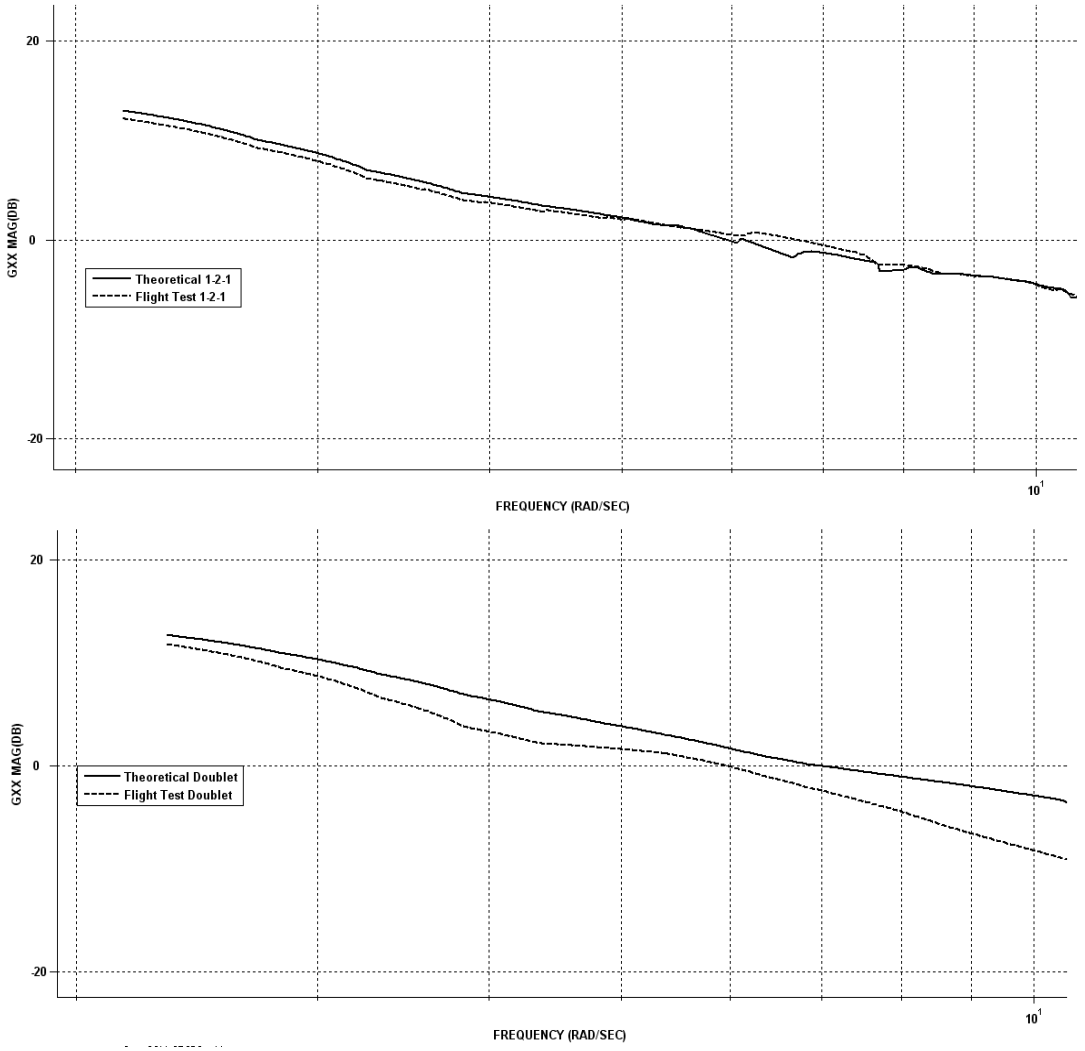

Figure 3.9 Input Power Spectral Density Comparison

In Figure 3.9, at the frequency range of 6 to 8 rad/s, it is seen that the 1-2-1 input applied in flight test has more excitation power than the theoretical one. This situation is possible for a certain frequency range where the flight test data have more information at those frequencies. Especially, it appears if the inputs are performed by pilots instead of automated inputs. Tischler states that the irregularity in the non-automatic input improves the richness of the excitation power spectrum [28].

3.4 Inputs Applied in Flight Tests

In this part, the identification inputs and verification inputs, which were applied in flight test, are shown. In the thesis, inputs given in below are used for both transfer function modeling and state-space modeling.

ElvSw	: Elevator Sweep
ElvVer1 and Ver2	: Verification inputs used to verify elevator sweep
AilSw	: Aileron Sweep
AilVer1 and Ver2	: Verification inputs used to verify aileron sweep
RudSw	: Rudder Sweep
RudVer1 and Ver2	: Verification inputs used to verify rudder sweep

Elevator identification test input lasts 22 seconds. It is seen from Figure 3.10 that in the elevator sweep, the low frequency parts and high frequency parts are applied successfully. Lateral and directional commands seem constant during the elevator sweep. Therefore, any correlation between inputs is not expected. There is a change in throttle while sweep but the amount of change seem small enough to keep the initial trim condition.

Elevator verification test inputs are two sets of doublets, which are totally four doublets. It is seen from Figure 3.11, aileron and rudder deflections seem unchanged during verification inputs are applied. The throttle is different in one doublet, it is expected that the trim condition for that doublet slightly different than others.

Aileron identification test input is applied at a flight leg of 25 seconds. During sweep, some elevator corrections were applied as it is seen in Figure 3.12. Since the corrections are not like a sweep, any correlation between aileron and elevator

commands is not expected. The throttle change before high frequency sweep inputs is seen in Figure 3.12. The change in the throttle seems small.

Aileron verification test inputs are a 1-2-1 input and a doublet given in Figure 3.13. The elevator input can be seen during this verification inputs. There is no change in throttle and rudder.

Rudder identification test input was applied during 16 seconds long flight leg. It is seen from Figure 3.14 that during sweep, both the low frequencies and high frequencies are applied successfully. However, during high frequency excitation, the throttle inputs also change. Since the motor dynamics generally response slowly while aircraft dynamics are concerned, the change in throttle in high frequencies may not affect the trim condition. Therefore, this rudder sweep can be used in identification.

Rudder verification inputs are rudder doublets given in Figure 3.15. During doublets, the throttle value also changes. Therefore, the aircraft dynamics may be affected by the change in the throttle. This rudder doublet data must be used carefully in identification.

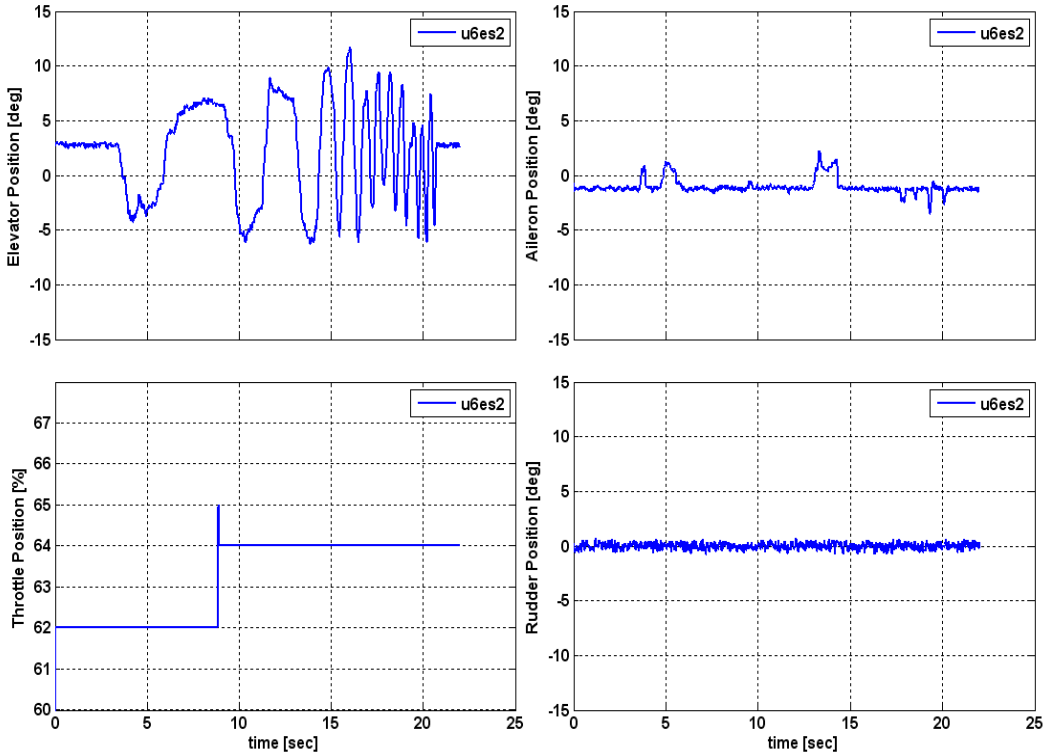

Figure 3.10 Control Surface Deflections during Elevator Sweep

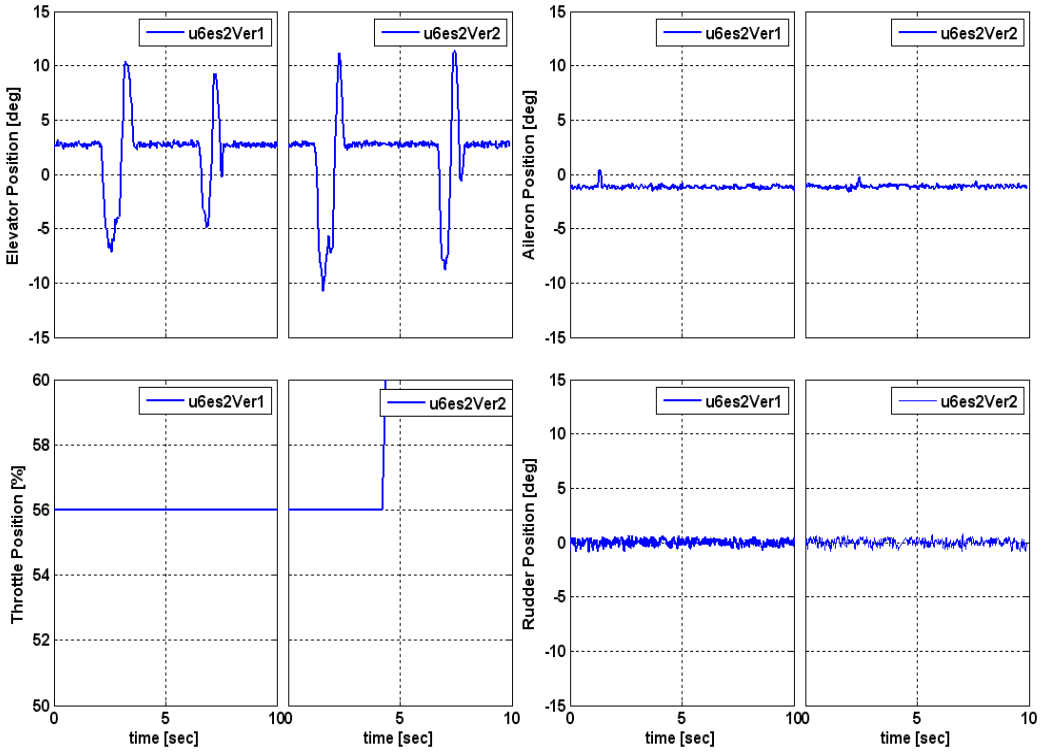

Figure 3.11 Control Surface Deflections during Elevator Verification Inputs

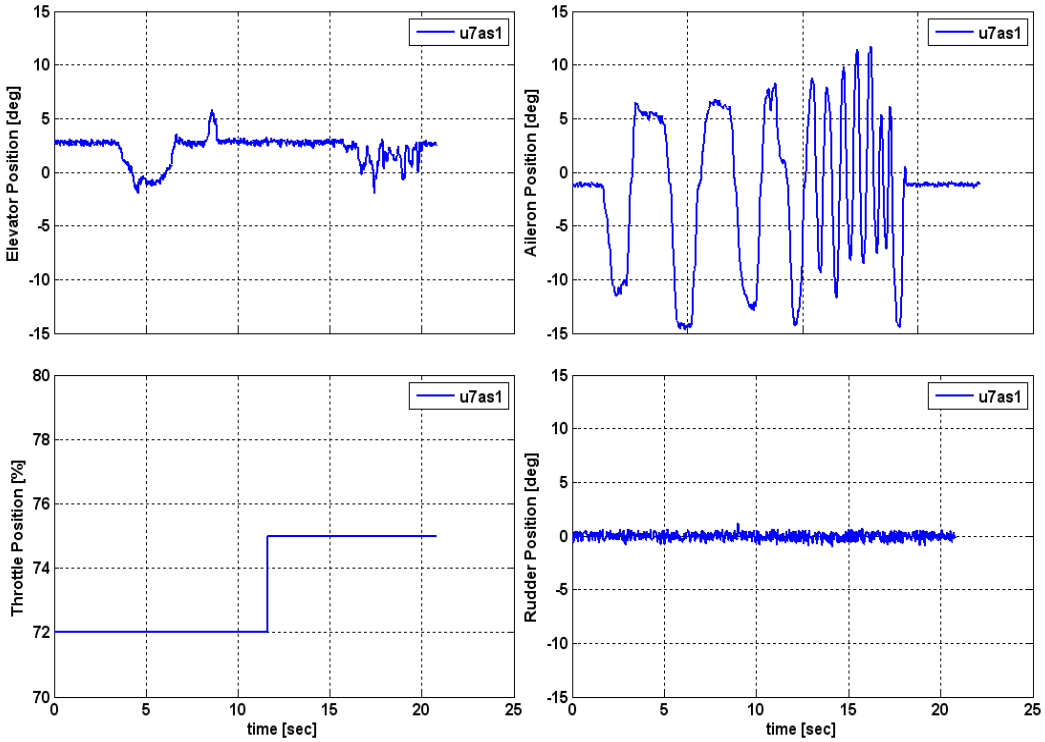

Figure 3.12 Control Surface Deflections during Aileron Sweep

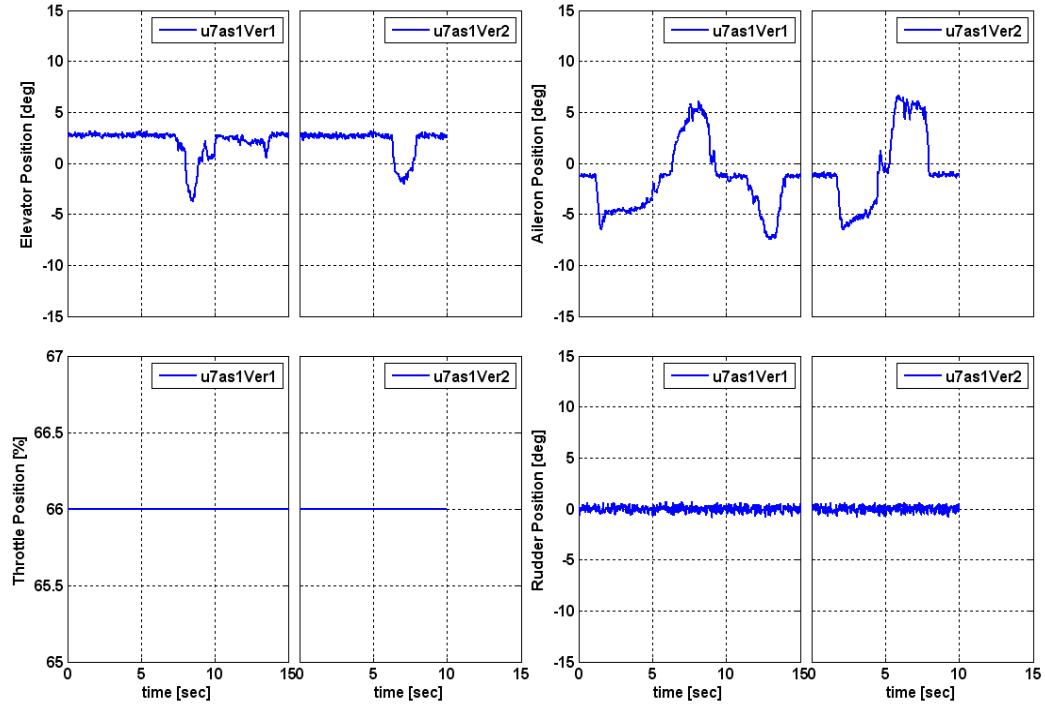

Figure 3.13 Control Surface Deflections during Aileron Verification Inputs

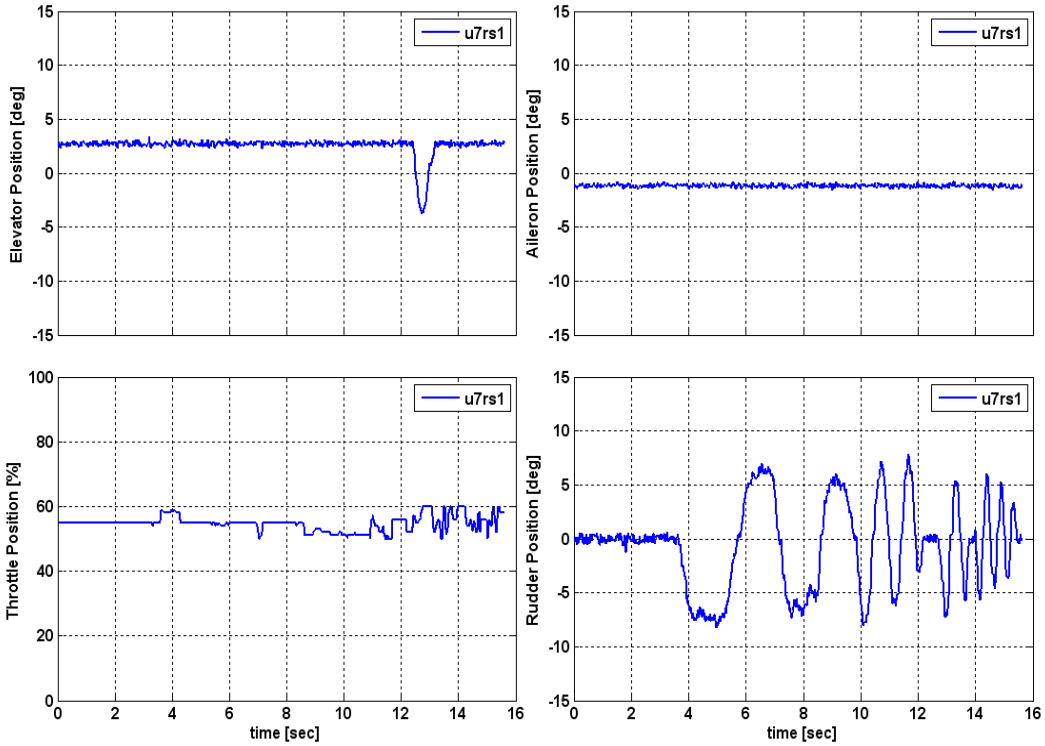

Figure 3.14 Control Surface Deflections during Rudder Sweep

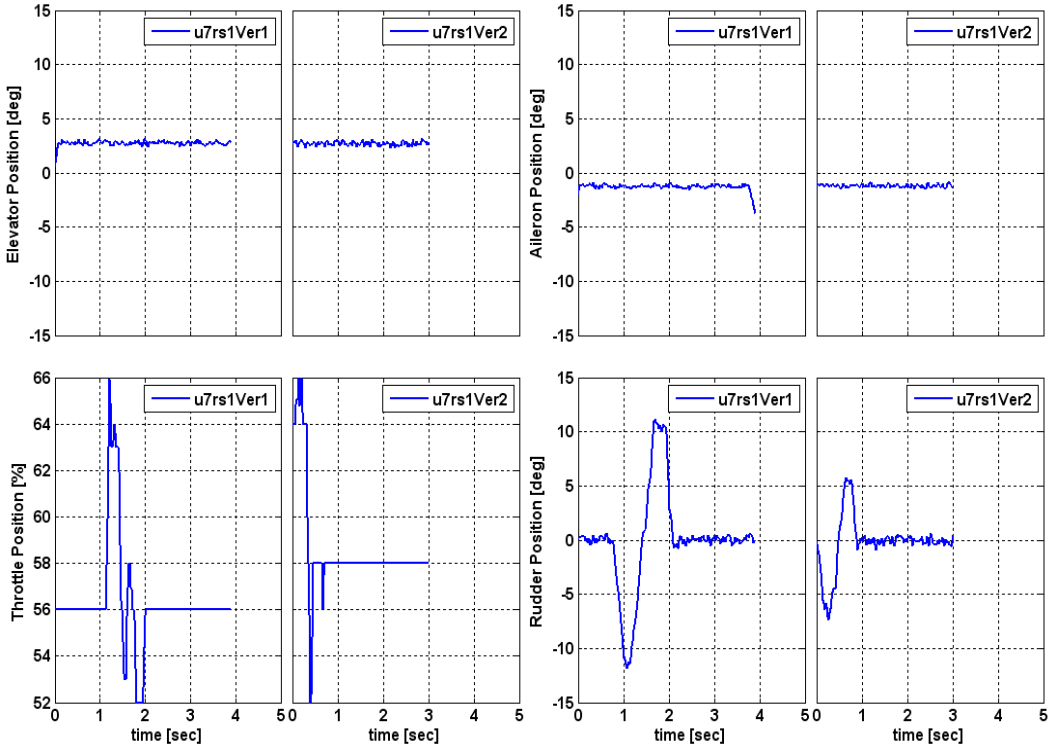

Figure 3.15 Control Surface Deflections during Rudder Verification Inputs

3.5 Flight Path Reconstruction

Before using the flight test data, it is often necessary and timesaving to verify whether the recorded data are compatible or not. This check satisfies determination of any corruption in the data caused by systematic errors like scale factors, zero shift biases and time lags are determined before identification process. Verifying the compatibility of measured data is based on the use of kinematic relationships. A detailed explanation is found in [17] and a good example is found in [16] about compatibility check. In compatibility check, the main aim is matching measured parameter with its computed value using its kinematic equation where its parameters take their measured values. For example, in Eqn. (3.1), measured y is matched by result of y function where parameters in y function take their measured values. This matching process is also termed as Flight Path Reconstruction (FPR). In general, there are two approaches to flight path reconstruction: [10]

- A rigorous one in the stochastic framework based on the extended Kalman filter, and
- A simpler one in the framework of deterministic systems based on the output error method.

When a simple sensor model is considered, the sensor model equation is given in terms of scale factor, bias and time delay as:

$$y_m(t) = K_y y(t - \tau) + \Delta y \qquad (3.1)$$

where

K_y : scale factor

Δy : unknown instrument bias

$y_m(t)$ & $y(t)$: measured output and computed output, respectively

Kinematic equations are valid for parameters values at CG position. Therefore, before reconstruction is applied, the measured parameters must be corrected to CG position since sensors generally are not put at CG due to practical constraints.

For accelerometer measurement correction, the linear accelerations at the center of gravity (a_x^{CG}, a_y^{CG}, a_z^{CG}) are computed from the accelerations measured by the sensor (a_{xm}^s, a_{ym}^s, a_{zm}^s) at a point away from the CG (x_{sCG}, y_{sCG}, z_{sCG}) through the following relation:

$$a_x^{CG} = a_{xm}^s + (q^2 + r^2)x_{sCG} - (pq - \dot{r})y_{sCG} - (pr - \dot{q})z_{sCG} - \Delta a_x \quad (3.2)$$

$$a_y^{CG} = a_{ym}^s - (pq + \dot{r})x_{sCG} + (p^2 + r^2)y_{sCG} - (qr - \dot{p})z_{sCG} - \Delta a_y \quad (3.3)$$

$$a_z^{CG} = a_{zm}^s - (pr - \dot{q})x_{sCG} - (qr + \dot{p})y_{sCG} - (p^2 + q^2)z_{sCG} - \Delta a_z \quad (3.4)$$

The biases in the measurements of (a_{xm}^s, a_{ym}^s, a_{zm}^s) are denoted by (Δa_x, Δa_y, Δa_z) and the angular rates (p, q, r) are given by ($p_m - \Delta p$, $q_m - \Delta q$, $r_m - \Delta r$) obtained by applying the corrections for the biases (Δp, Δq, Δr), to the measured rates (p_m, q_m, rm). The variables ($\dot{p}, \dot{q}, \dot{r}$) are obtained by numerical differentiation of the measured angular rates.

The speeds are measured using nose boom; therefore before using these in reconstruction, they are corrected for CG position using (3.5), (3.6) and (3.7).

$$u_{NB} = u - (r_m - \Delta r)y_{NBCG} + (q_m - \Delta q)z_{NBCG} \quad (3.5)$$

$$v_{NB} = v - (p_m - \Delta p)z_{NBCG} + (r_m - \Delta r)x_{NBCG} \quad (3.6)$$

$$w_{NB} = w - (q_m - \Delta q)x_{NBCG} + (p_m - \Delta p)y_{NBCG} \quad (3.7)$$

When the flight test data are analyzed, it is noticed that the measured variables are too noisy to use in an analysis. Therefore, Savitzky-Golay Filter is used to eliminate the noise in the data. Savitzky and Golay proposed a method of data smoothing based on local least-squares polynomial approximation [27]. The local least-square polynomial approximation is expressed using Eqn. (3.8). The name of local term comes from that Eqn. (3.8) is applied each 2M+1 samples centered at n=0 in the data. The 2M+1 samples are selected starting with M+1 term in the data then new block of 2M+1 samples is obtained by shifting the interval to the right by one sample. As seen in the Eqn. (3.8), the coefficients of the approximated polynomial are estimated to minimize the mean-squared approximation error.

$$\varepsilon_N = \sum_{n=-M}^{M} (p(n) - x[n])^2 \tag{3.8}$$

where

$p(n)$: polynomial approximation for 2M+1 samples $p(n) = \sum_{k=0}^{N} c_k n^k$

$x[n]$: 2M+1 samples

N: is the order of the polynomial approximation

The coefficients of the polynomial that give minimum error are calculated by differentiating Eqn. (3.8) with respect to each unknown coefficients and setting these derivatives equal to zero.

$$\frac{\partial \varepsilon_N}{\partial c_i} = \sum_{n=-M}^{M} 2n^i \left(\sum_{k=0}^{N} c_k n^k - x[n]\right) = 0 \tag{3.9}$$

From Eqn. (3.9)

$$\sum_{k=0}^{N} \left(\sum_{n=-M}^{M} n^{i+k} \right) c_k = \sum_{n=-M}^{M} n^i x[n] \tag{3.10}$$

for $i = 0,1, \dots, N$

To obtain the unique solution of Eqn. (3.10), there must be at least as many data samples as the coefficients in the approximated polynomial, which is written as $N \leq 2M$.

For the matrix representation of Eqn. (3.10), a matrix A is defined as

$$\boldsymbol{A} = \{\alpha_{n,i}\} \tag{3.11}$$

where $\alpha_{n,i} = n^i$

The term $\sum_{n=-M}^{M} n^{i+k}$ in the left hand side of the Eqn. (3.10) is written as

$$\sum_{n=-M}^{M} n^{i+k} = \sum_{n=-M}^{M} n^i n^k = \sum_{n=-M}^{M} \alpha_{n,i}\alpha_{n,k} = \boldsymbol{A}^T\boldsymbol{A} \tag{3.12}$$

The term $\sum_{n=-M}^{M} n^i$ in the right hand side of the Eqn. (3.10) is written as

$$\left\{\sum_{n=-M}^{M} n^i n^k\right\} = \boldsymbol{A}^T \tag{3.13}$$

Then the Eqn. (3.10) is written in matrix form as given:

$$\boldsymbol{A}^T\boldsymbol{A}\,\boldsymbol{a} = \boldsymbol{A}^T\,\boldsymbol{x} \tag{3.14}$$

where

$\boldsymbol{c} = [c_0, c_1, \dots, c_N]^{\boldsymbol{T}}$ is the vector of polynomial coefficients

$\boldsymbol{x} = [x[-M], \dots, x[0], \dots, x[-M]]^{\boldsymbol{T}}$ is the vector of input samples

$\boldsymbol{A} = \begin{bmatrix} 1 & x^1 & \cdots & x^N \\ \vdots & \vdots & \vdots & \vdots \\ 1 & x^1 & \dots & x^N \\ \vdots & \vdots & \vdots & \vdots \\ 1 & x^1 & \dots & x^N \end{bmatrix}$ derived from polynomial order, N and window length 2M+1

The polynomial coefficients are found using Eqn. (3.14)

$$\boldsymbol{c} = (\boldsymbol{A}^T\boldsymbol{A})^{-\mathbf{1}}\boldsymbol{A}^T\,\boldsymbol{x} = \mathbb{A}\boldsymbol{x} \tag{3.15}$$

From Eqn. (3.13), it is seen that $\boldsymbol{A}$ matrix is not depend on input samples; therefore, it is said that in (3.15), the $\mathbb{A}$ depends only M and N, which means that it is independent from the input samples, and it consists constants derived from M and N.

The Savitzky-Golay filter obtains smoothed data by evaluating the polynomial coefficients (Eqn. (3.15)) for the central point of the 2M+1 sample (n=0). Therefore, the filter smooth only n=0 sample by using a polynomial obtained from 2M+1 points. Since $p(n) = \sum_{k=0}^{N} c_k n^k$, the smoothed value is equal to c_0.

The Savitzky-Golay filter has been widely used filter, which is selected as #5 of the top ten articles ever published in Analytical Chemistry journal [27]. This filter is often preferred, because it tends to keep the form of peaks in the signal. Specially, this filter has supremely flat passband, so it satisfies undistorted signal while removing high frequency noise. Moreover, symmetric Savitzky-Golay filter does not cause any phase shift. Also, it improves computational speed significantly when is compares with traditional least square [27].

This filter is applied to speed, angular speed, control surface deflections angel of attack and angle of sideslip measurements. Therefore, the noise in the data is eliminated.

In this study, OEM (output error method) is used for flight path reconstruction and the model for this method is summarized in Table 3.2. OEM is used state and input variables in equations with unknown estimation variables and then obtains calculated values of measurement variables. The estimated values of unknown variables are achieved by matching measured and calculated variables [10].

Table 3.2 Variables for OEM

State Variables	$u, v, w, \phi, \theta, \psi, h$
Measurement Variables	$V_m, \alpha_m, \beta_m, \phi_m, \theta_m, \psi_m, h_m$
Input Variables	$a_x, a_y, a_z, p, q\ , r$
Estimation (Unknown) Variables	$\Delta a_x, \Delta a_y, \Delta a_z, \Delta p, \Delta q, \Delta r, K_\alpha, \Delta\alpha, K_\beta, \Delta\beta$

Jategaonkar gives the detailed information about OEM and procedure for application of OEM in his book comprehensively [10]. Moreover, in this study for FPR, the code given in this book is used to obtain estimated values of unknown variables in Table 3.2. Since frequency domain identifications can remove biases in the data, in this study FPR is used in only calculation of scale factors of angle of attack and angle of

sideslip; however, to use same method for bias and scale factor, the biases of these parameters are also calculated by OEM.

Flight path reconstruction (FPR) is applied for longitudinal and lateral/directional motion separately. In longitudinal motion FPR, the scale factor and bias of AoA are estimated, and in lateral/directional motion, the scale factor and bias of AoS are estimated using Eqn. (3.1). Reconstructed values of AoA and AoS values are shown in Figure 3.16 and Figure 3.17 by comparing with measured values. In the rest of the study, the reconstructed values of AoA and AoS are used in identification. The obtained scale factor values for AoA and AoS are 1.32 and 1.107 respectively and the biases for AoA and AoS are calculated as -0.0017 rad and -0.014 rad respectively.

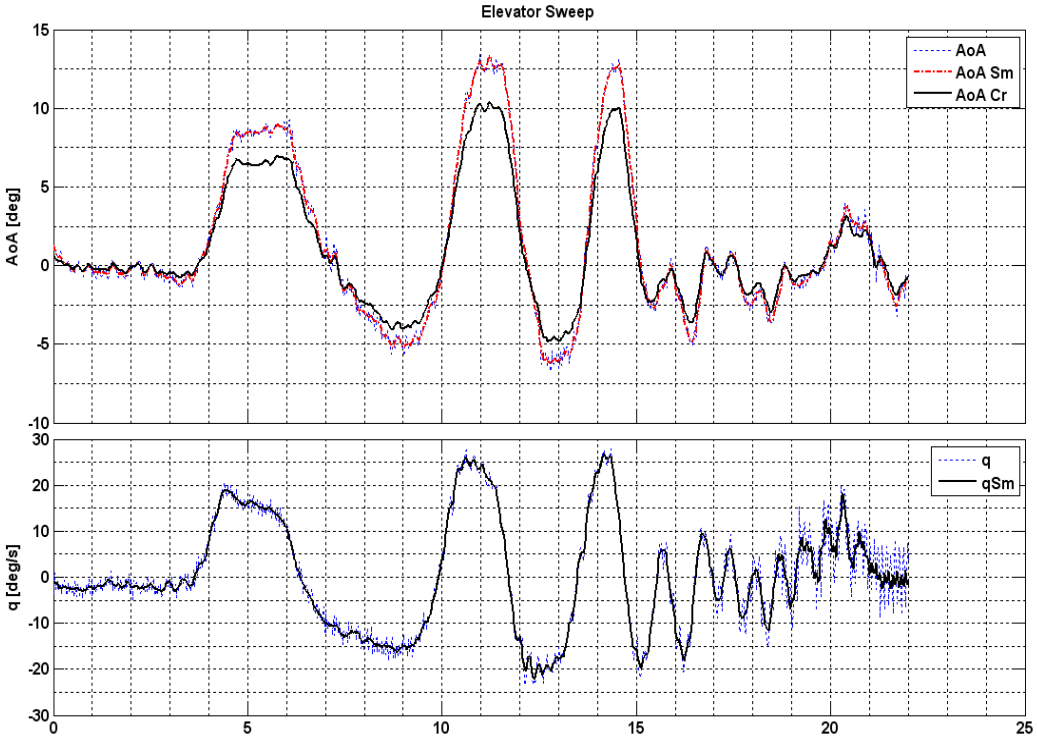

Figure 3.16 Filtered (Sm) and Corrected (Cr) Values - Elevator Sweep

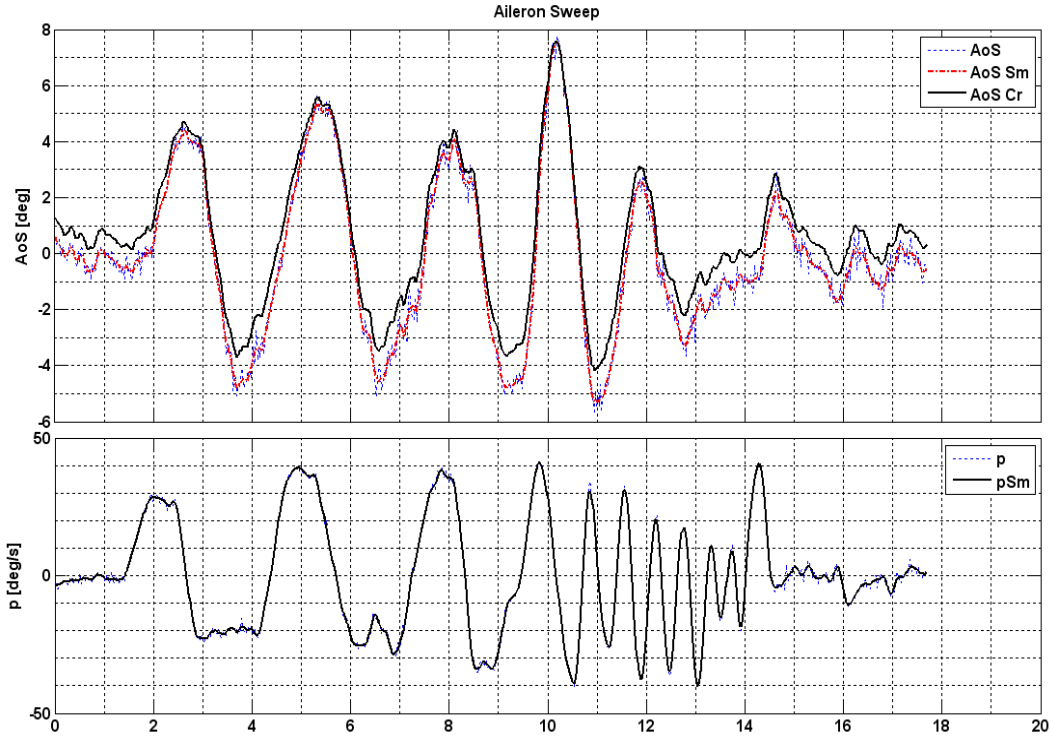

Figure 3.17 Filtered (Sm) and Corrected (Cr) Values – Aileron Sweep

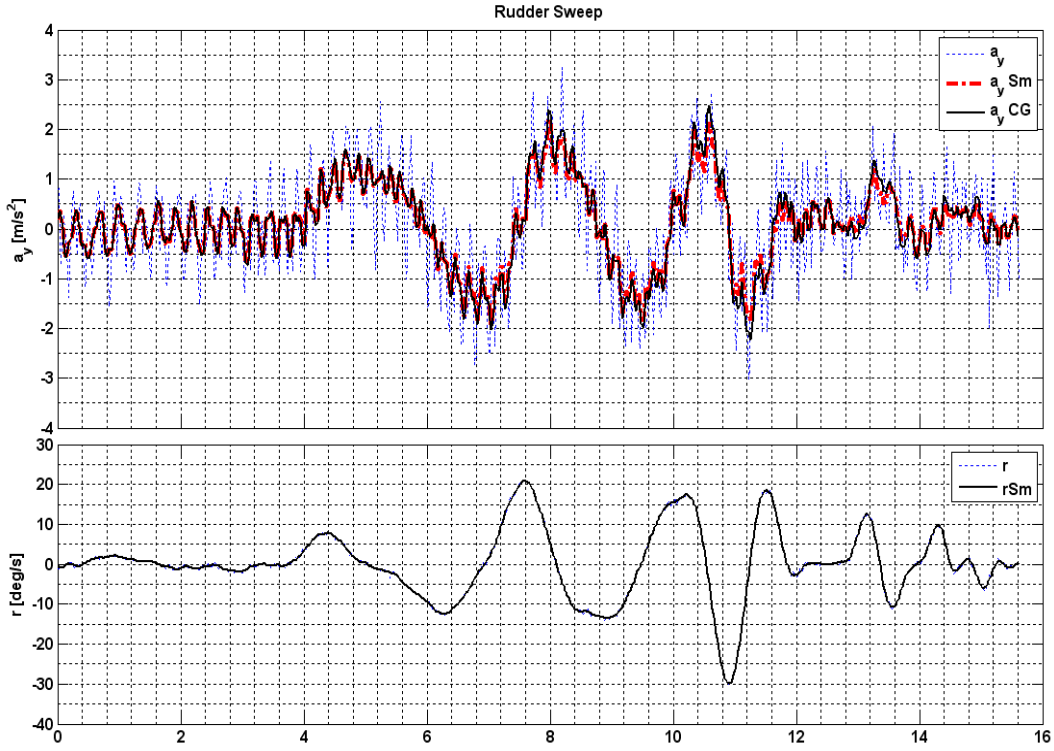

Figure 3.18 Filtered (Sm) and Corrected (CG) Values – Rudder Sweep

CHAPTER 4

TRANSFER FUNCTION MODELING

4.1 Introduction

This chapter presents the transfer function approach to system identification of the UAV. Transfer function model of a system describes input-output relations linearly in terms of poles and zeros, which identify the dynamic characteristics of the system, called as dynamic modes. Moreover, using this approach, control sensitivity is obtained. Transfer function modeling is the simplest way of identification from frequency-domain database and fit the best matches on Bode plot in the frequency range of interest [28].

Although the complete aircraft dynamics include many states, the overall input and output relation is well identified over the frequency range of interest by using transfer function composed modeling, which includes only dominant modes. This is what the LOES modeling based on, which makes transfer function modeling of high order systems like aircrafts possible. Hodgkinson initially studies LOES modeling in 1976. There are lots of studies on LOES modeling of various aircrafts. One of them is given as an example. In that study, LOES models for the closed loop dynamics of an augmented aircraft are identified using flight test data. In that study, two parameter estimation methods in frequency domain are used: Output Error and Equation Error [21].

In transfer function modeling approach, the numerical optimization algorithm, which uses least-square method, estimate the parameters by minimizing the error between phase and magnitude values of data and estimated results. In the algorithm, the errors are formulated in the following cost function:

$$J = \frac{20}{n_\omega} \sum_{\omega_1}^{\omega_{n_\omega}} W_\gamma [W_g \left(\left|\hat{T}_c\right| - |T|\right)^2 + W_p (\angle \hat{T}_c - \angle T)^2] \tag{4.1}$$

where

| | and ∠ : magnitude (dB) and phase (deg) at each frequency ω

n_ω : Number of frequency points where the cost function is calculated

ω_1 and ω_{n_ω} : starting and ending frequencies in identification process

W_γ : Weighting function, which is function of coherence

$$W_\gamma(w) = \left[1.58(1 - e^{-\gamma_{xy}^2})\right]^2$$

W_g and W_p : Weights for magnitude and phase errors, respectively. They are taken constant values of 1.0 and 0.01745 [28].

The transfer function of a linear, time-invariant, differential equation system is defined as the ratio of the Laplace transform of the output (response function) to the Laplace transform of the input (driving function) under the assumption that all the initial conditions are zero [23]. Since transfer function is composed of a numerator and denominator polynomials in Laplace variable s, it is written as:

$$\mathrm{T(s)} = \frac{(\mathrm{b_0 s^m + b_0 s^m + \cdots + b_m})}{(\mathrm{s^n + a_1 s^{n-1} + \cdots + a_n})} \tag{4.2}$$

In transfer function model, a time delay parameter is put into Eqn. (4.2) to identify

- the phase lag due to high frequency dynamics. Since identification model covers a limited frequency range; there may be unmodeled dynamics of the system at out of this range. The effect of this unmodeled high-frequency dynamics is seen as phase lag in the identified model.

- time delays like transport delays arising from control and measurement processing:

$$T(s) = \frac{(b_0 s^m + b_0 s^m + \cdots + b_m)\, e^{-\tau_{eq} s}}{(s^n + a_1 s^{n-1} + \cdots + a_n)} \tag{4.3}$$

The transfer function modeling procedure is drawn in a flowchart in Figure 4.1. In the flowchart, "Flight Test Design", "Flight Tests" and "Evaluation of Flight Tests Results" parts are discussed in Chapter III. Therefore, in this chapter,

- "Model Structure Selection"
- "Parameter Estimation"
- "Time-Domain Verification" parts are covered.

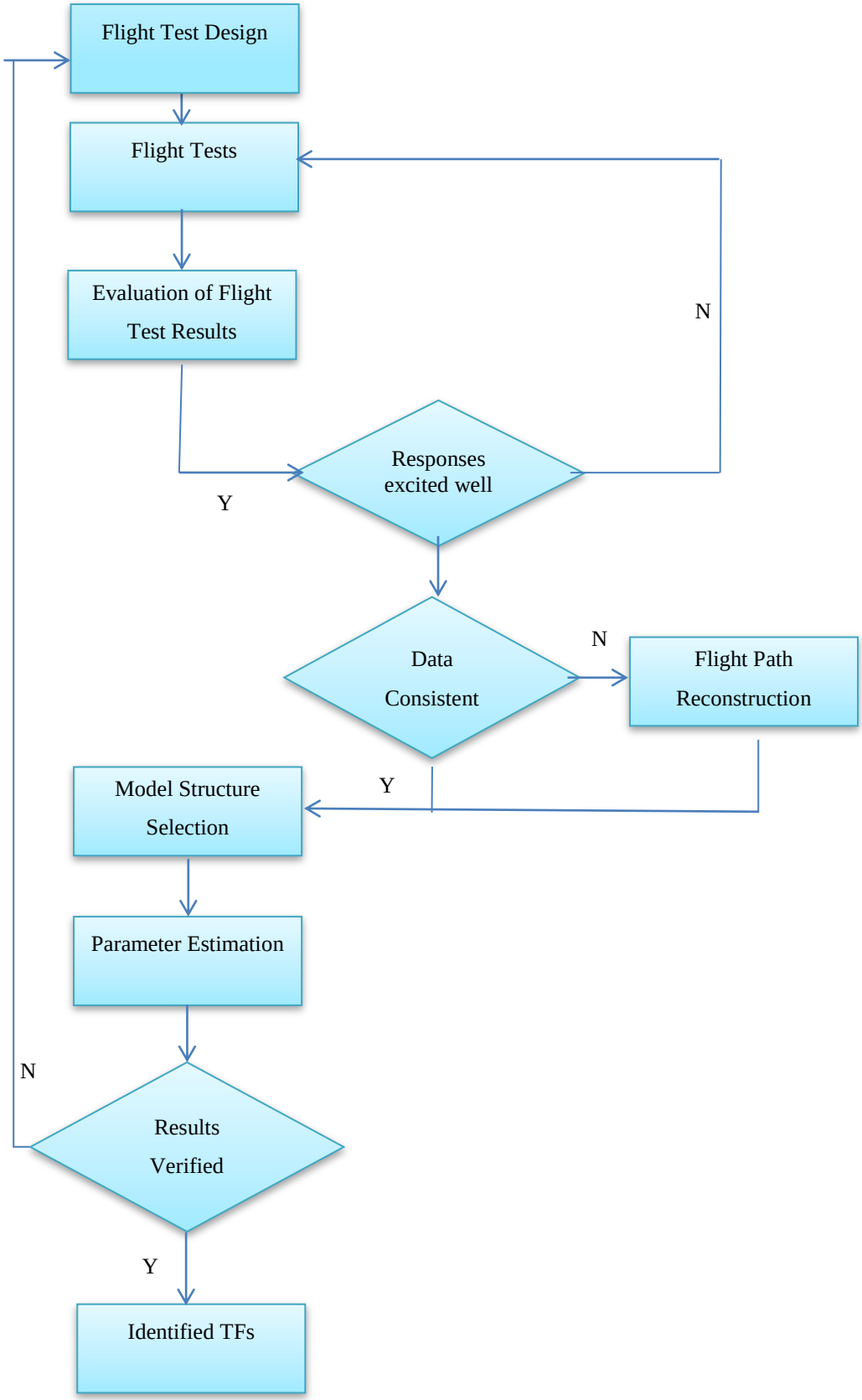

Figure 4.1 Flowchart of Transfer Function Modeling

4.2 Low Order Equivalent System (LOES) Modeling

In the past, handling quality criteria and specifications were derived using open loop unaugmented aircrafts; to be able to use these criteria and specifications for closed loop and augmented aircrafts, which have high order and nonlinear dynamics, Low Order Equivalent System (LOES) modeling was introduced [20].

The main question in LOES modeling was that how the errors between the LOES model and high order systems (HOS) could be modeled. This problem was overcome by introducing equivalent time delay term into LOES modeling.

After that another problem arose since there were no success criteria for LOES models. The difference between HOS and LOES is measured by obtaining the phase and gain error for each frequency; if the errors are zero, it has been known that LOES model perfectly fits the HOS dynamics; however, up to which value the model is accepted as a successful representation of HOS had not been known until Maximum Unnoticeable Added Dynamics (MUAD) boundaries were introduced. [15]

In Section 4.2.1, detailed information about MUAD boundaries and how MUAD boundaries are obtained are discussed. Section 4.2.2 gives explanation about how time delay is used for unmodeled dynamics and its effects on stability and handling quality.

4.2.1 MUAD Boundaries

The major problem in LOES modeling was that an accepted limit for the mismatch between HOS and LOES had not defined. Therefore, it was difficult to give a decision about whether equivalent system represents high order system successfully or not. To overcome this difficulty, the Equivalent System Program (ESP) was started and in the analysis, variable stability NT-33 aircraft in-flight simulation was used [15].

In the ESP, for CTOL aircraft, two fundamental principles of manual control theory: the Neal-Smith experiment and the Landing Approach High Order System (LAHOS) experiment results were used to analyze the contributions of the following added dynamics to base aircraft model [15]:

- First order lead-lag
- First order lags
- Second order lag pre-filters
- A fourth order lag pre-filter
- A second order lag pre-filter – first order lead-lag combination

Both experiments were not run by aiming the evaluation of added dynamics contamination to low order system models at all frequencies. Unluckily, the critical added dynamics at these experiments covered only high frequencies. However, the lack of low frequencies was overcome by estimating low frequencies by using phugoid transfer function in Eqn. (4.4). The low frequency part of the gain and phase envelops of MUAD boundaries were formed using Eqn. (4.4)

$$\frac{\dot{\theta}}{\delta_e} = \frac{(s + {}^{1}/_{T_{\theta_1}})}{(s^2 + 2\zeta_{ph}\omega_{ph} + \omega_{ph}^2)} \tag{4.4}$$

Many cases were formed for each added dynamics in the experiments. To define MUAD, these cases were applied in a simulation and the pilots rated the model, where added dynamics were included, using Cooper-Harper ratings. The Maximum Unnoticeable Dynamics cases were determined by selecting the last case for each added dynamics, where the change in Cooper-Harper rating is below or equivalent to 0.5.

To obtain the boundaries of MUAD, the frequency responses of the critical cases are plotted on a common Bode plot, then lines were drawn by fairing smooth curves either through or tangent to frequency responses of critical cases of each added dynamics. These drawn lines represent the MUAD boundaries. The values of MUAD boundaries were tabulated for each frequency.

Finally, the transfer functions models of these curves were estimated using NAVFIT program. The valid frequency range for these transfer function models are 0.1 to 100 rad/s. The transfer function for gain and phase errors are given in Eqn. (4.5), (4.6), (4.7), (4.8)

$$Upper\ Gain\ Env: \frac{3.16s^2 + 31.61s + 22.79}{s^2 + 27.14s + 1.84} \tag{4.5}$$

$$Lower\ Gain\ Env: \frac{0.0955s^2 + 9.92s + 2.15}{s^2 + 11.6s + 4.95} \tag{4.6}$$

$$Upper\ Phase\ Env: \frac{68.89s^2 + 1100.12s + 275.22}{s^2 + 39.94s + 9.99} e^{-0.0059s} \tag{4.7}$$

$$Lower\ Phase\ Env: \frac{475.32s^2 + 184100s + 29456.1}{s^2 + 11.66s + 0.0389} e^{-0.0072s} \tag{4.8}$$

MUAD boundaries are accepted by the authorities, and these boundaries are given in military standard, MIL-HDBK-1797, which supersedes MIL-STD-1797A [19].

4.2.2 Equivalent Time Delay

For a differential equation given in Eqn. (4.9), time delay in states means that $\dot{x}$ reacts according to past state at $t - \tau$ and current input, which is given in Eqn. (4.10). Moreover, time delay in inputs means that $\dot{x}$ reacts according to current state and past input at $t - \tau$ as given in Eqn. (4.11)

$$\dot{x} + x = u \tag{4.9}$$

$$\dot{x} + x(t - \tau) = u \tag{4.10}$$

$$\dot{x} + x = u(t - \tau) \tag{4.11}$$

The Laplace transforms of the Eqn. (4.10) and (4.11) are written as:

$$H(j\omega) = \frac{1}{(j\omega) + e^{-j\omega\tau}} \tag{4.12}$$

$$H(j\omega) = \frac{1}{(j\omega) + 1} e^{-j\omega\tau} \tag{4.13}$$

As it is seen in the Eqn. (4.12) and (4.13), unlike the time delay in the states, the time delay in the input is transformed as a multiplication term in the transfer function.

The transfer function of the aircraft dynamics can be divided into two:

$$TF_{A/C} = TF_{Modeled} \times TF_{Unmodeled} \tag{4.14}$$

If it is shown that unmodeled dynamics response behavior is similar with time delay characteristics, the aircraft transfer function can be written as a multiplication of transfer function expression and a time delay term.

An example is given below to show the relation between unmodeled dynamics and time delay in frequency domain. In this example, the aircraft dynamics is given in Eqn. (4.15), where the first part is called as modeled part and the second part is called as unmodeled part. The equivalent representation of the A/C dynamics with the time delay term is given in Eqn. (4.16). Another low order representation of the A/C dynamics is given in (4.17).

$$TF_{A/C_1} = K\frac{-8.50}{(s^2 + 4.05s + 8.96)} \times \frac{1}{(s^2 + 16.08s + 144)} \tag{4.15}$$

$$TF_{\frac{A}{C_2}} = K\frac{-8.50}{(s^2 + 4.05s + 8.96)} \times e^{-0.12s} \tag{4.16}$$

$$TF_{A/C_3} = K\frac{-8.50}{(s^2 + 4.05s + 8.96)} \tag{4.17}$$

It is seen form Figure 4.2 that the time delay representation represents the A/C dynamics up to certain frequency. Moreover, it is seen that the magnitude response of TF_{A/C_2} is similar with TF_{A/C_3}; however it is easily noticed that there is a phase shift between the response of the TF_{A/C_2} and TF_{A/C_3}. These relations can be explained by using Euler's theorem:

$$e^{-\tau s}|_{s=j\omega} = \cos(\omega\tau) - j\sin(\omega\tau) \tag{4.18}$$

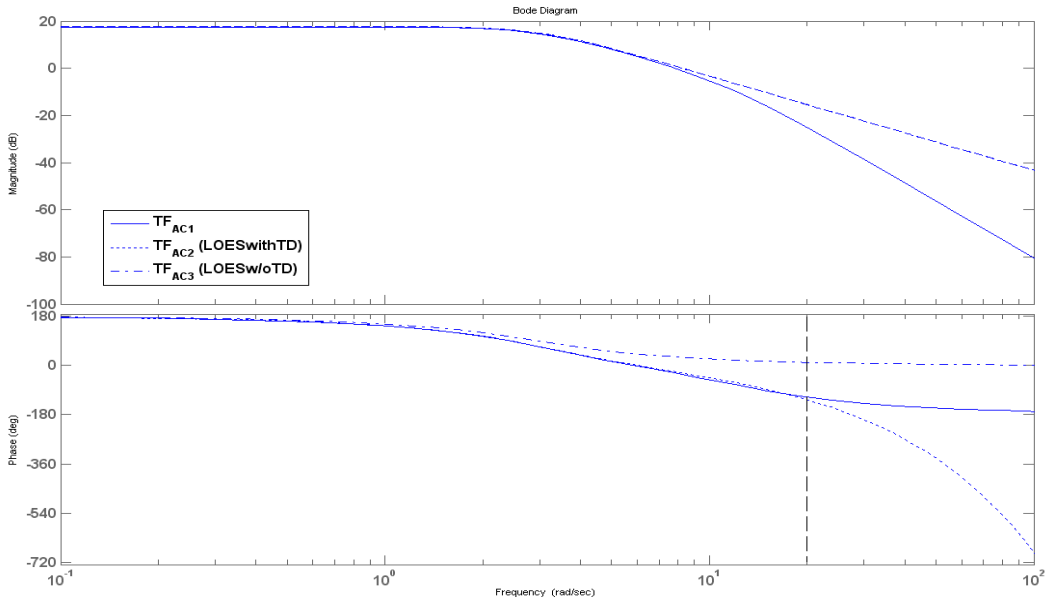

Figure 4.2 Example Transfer Functions for Time Delay Effect

Therefore, the magnitude and phase of $e^{-\tau s}$ is found using Eqns. (2.4) and (2.5) as:

$$|e^{-\tau s}| = 1 \tag{4.19}$$

$$\varphi(\omega) = \angle e^{-\tau s} = -\tau\omega \tag{4.20}$$

When Eqn (4.19) and (4.20) are examined, it is noticed that the time delay in the input has no effect on the magnitude; however, it creates phase shift in the system. The example shows that an unmodeled dynamics can be modeled as time delayed term.

The equivalent time delay represents a frequency-response phase lag as:

$$\varphi = -\tau_{eq}\omega \tag{4.21}$$

Although using time delays in modeling is a successful way of representing the unmodeled high order dynamics in the identified model, it must be considered that time delays causes reduction in stability when closed loop system is concerned where the pilot-in-the-loop or controller-in-the-loop. When an equivalent time delay is used in identification, stability of the system must be checked.

In this study, to check the effect of the time delay, the fundamental limitations of the closed loop system are determined. Fundamental limitation analyses give insight into the subjects that fundamentally limit the performance of the closed loop system. Therefore, determining the fundamental limits is critical in order to know the system performance boundaries. A popular example of fundamental limitation is the design effort to satisfy the phase margin requirement for X-29 advanced experimental aircraft. Massive design effort was spent with many methods but they were not successful to meet the requirement since the fundamental limit of their system for phase margin is below the required value [2].

In this study, only necessary information is given to explain the effect of time delay on stability. More detailed information about the fundamental limitations can be found in the reference [2].

Fundamental limitations was studied by Bode and depends on the crossover frequency inequality

$$\arg L(i\omega_{gc}) = arg P_{nmp}(i\omega_{gc}) + arg P_{mp}(i\omega_{gc}) + arg C(i\omega_{gc}) \geq -\pi + \varphi_m \tag{4.22}$$

where

L : is the loop transfer function $\mathrm{L(s)} = \mathrm{P(s)C(s)}$

C : is the controller transfer function

P : is the system (plant) transfer function and it is written as $P(s) = P_{mp}(s)P_{mp}(s)$

P_{mp} : is the minimum phase part of the plant where all its poles and zeros are in left half plane

P_{nmp} : is the non-minimum phase part of the plant and its phase lag larger than minimum part

arg : is a function that gives the angle between the line joining the point to the origin and positive real axis for complex numbers

ω_{gc} : is the gain crossover frequency

φ_m : is the desired phase margin

After that, assume the multiplication of designed controller and minimum phase part of the plant is equal to Bode's ideal loop transfer function

$$P_{mp}(s)C(s) = \left(\frac{s}{\omega_{gc}}\right)^{n} \tag{4.23}$$

Using the relation in Eqn. (4.24), the following expression can be obtained

$$argP_{mp}(i\omega_{gc}) + argC(i\omega_{gc}) \approx n_{gc}\frac{\pi}{2} \tag{4.24}$$

Therefore, the crossover frequency inequality is written as

$$argP_{nmp}(i\omega_{gc}) \geq -\pi + \varphi_m - n_{gc}\frac{\pi}{2} \tag{4.25}$$

For the system with a time delay, the non-minimum phase part is written as:

$$P_{nmp}(s) = e^{-s\tau} \tag{4.26}$$

$$argP_{nmp}(i\omega) = -\omega\tau \tag{4.27}$$

Then, the crossover frequency inequality in Eqn. (4.25) becomes

$$\omega_{gc}\tau \leq \pi - \varphi_m + n_{gc}\frac{\pi}{2} \tag{4.28}$$

As seen in Eqn. (4.28), time delays give an upper bound on the achievable bandwidth, where the bandwidth defines the frequency range at which the system can follow the input. Therefore, since time delay reduces the frequency, which the system can follow, the closed loop performance is reduced.

If the system is gain limited, where gain bandwidth frequency is less than phase bandwidth frequency, or desired phase margin is given and gain crossover frequency is asked, then Eqn. (4.29) becomes [8]:

$$\omega_{gc} \leq \frac{\pi - \varphi_m + n_{gc}\frac{\pi}{2}}{\tau} \tag{4.29}$$

For example, for a desired phase margin of 45° ($\varphi_m = {\pi}/{4}$) and a slope of $n_{gc} = {-1}/{2}$, the Eqn. (4.30)

$$\omega_{gc} \leq \frac{1.57}{\tau} \tag{4.30}$$

If the system is phase limited or phase margin is asked, the Eqn. (4.31) becomes:

$$\varphi_m \leq \pi - \omega_{gc}\tau + n_{gc}\frac{\pi}{2} \tag{4.31}$$

As seen in Eqn. (4.29) and (4.31), the time delay decreases upper limit value for phase margin and gain crossover frequency, which means that the maximum available performance of closed loop system is reduced. Therefore, the decision of time delay usage must be given by taking closed loop performance criteria into consideration.

4.3 Model Structure Selection

The model structure determination is important for transfer function modeling, since model structure determines response characteristics to inputs. If it is identified correctly, then the rest is estimating the transfer function coefficients. Since transfer functions do not provide any information about physical structure of the system, the model structure is determined using following steps by concerning the possible physical structure of the system:

- the input-output pairs,
- frequency range of interest,
- order of numerator and denominator,
- equivalent time delay

Then the identifiable parameters, which are coefficients of numerator and denominator and time delay τ_{eq}, are estimated.

Input-Output Pairs

For a dynamic mode, which will be identified, proper input-output pair(s) for that mode must be selected from data. The dominant pairs that have most available information about the desired dynamic mode are found by [28]:

- using dominant pairs in flight mechanics approximations like short period and phugoid approximations. For example; for longitudinal motion, α/δ_e and u/δ_t are used. Moreover, for lateral/directional motion, the pairs p/δ_a and β/δ_r are used when roll mode and Dutch roll mode approximations are concerned.
- using pairs that have high coherence. For example, the coherence of attitude rates at low frequencies is relatively smaller than ones at high frequencies due to high signal to noise ratio. If coherence value is so small that it creates difficulty in identification, instead of attitude rate transfer function, attitude transfer function is used for these low frequency ranges.

Considering these explanations, in this study, β/δr is chosen for directional motion, p/δa is chosen for lateral motion, α/δe is chosen for short period motion.

Frequency Range of Interest

The frequency range used in identification is defined by frequency range of interest where the model is wanted to be valid. For the handling quality analysis, the frequency range of interest is taken as 0.1 – 10 rad/s [28]. If the aircraft is excited properly through the desired frequency range and the input/output pairs have high coherence then the whole frequency range of interest is used in identification. If this transfer function model is used for flight control design, the model must be accurate for frequencies near crossover frequency ω_c, generally 0.3 ω_c to 3 ω_c [28]. Another point, which must be remembered, is that the identified model is valid in the frequency range used in identification. Therefore, for the low frequencies such as steady state (ω=0) or higher frequencies then identified range (ω>10rad/s), the model is used carefully [28].

Order of Numerator and Denominator

The order of numerator and denominator is the main factor that represents response characteristics. An appropriate transfer function model of fixed wing A/C dynamics is based on the classical flight mechanics approaches. Therefore, for the pairs p/δa and β/δr the transfer function models are chosen as [26]:

$$\frac{p}{\delta_a}(s) = \frac{s(A_\emptyset s^2 + B_\emptyset s + C_\emptyset)}{A_2 s^4 + B_2 s^3 + C_2 s^2 + D_2 s + E_2} \tag{4.32}$$

$$\frac{\beta}{\delta_r}(s) = \frac{A_\beta s^3 + B_\beta s^2 + C_\beta s + D_\beta}{A_2 s^4 + B_2 s^3 + C_2 s^2 + D_2 s + E_2} \tag{4.33}$$

The third zero in β/δr transfer function is at higher frequency than the upper limit of range of interested frequency [5]. Therefore, the third zero is not given in the model structure.

For the pairs α/δe and u/δt the transfer function models are chosen as [26]:

$$\frac{\alpha}{\delta_e}(s) = \frac{A_\alpha s^3 + B_\alpha s^2 + C_\alpha s + D_\alpha}{A_1 s^4 + B_1 s^3 + C_1 s^2 + D_1 s + E_1} \tag{4.34}$$

$$\frac{u}{\delta_t}(s) = \frac{A_u s^3 + B_u s^2 + C_u s + D_u)}{A_1 s^4 + B_1 s^3 + C_1 s^2 + D_1 s + E_1} \tag{4.35}$$

4.4 Parameter Estimation

After the model structure is built up, the coefficients of transfer function are estimated by using frequency domain system identification program: CIFER®.

CIFER® (Comprehensive Identification from Frequency Responses) is software created by the US Army Aeroflightdynamics Directorate (AFDD at Ames Research Center). CIFER® is the only integrated package for the end-to-end frequency-response identification method. CIFER® has proven to be a very effective tool for the system identification and has used widely in both fixed-wing and rotary-wing identification.

The procedure applied in CIFER® is explained as following:

The user specifies the individual records to be processed in frequency domain. FRESPID tool determines and removes the average value (biases) and linear drift from each individual record and then concatenates these records into a single linked record. The concatenated inputs and outputs are then digitally filtered to eliminate the high-frequency noise. Then, the linked records are segmented and weighted using the overlapped windowing method for the window size specified by the user. These overlapped windows of data are transformed into the frequency domain, using the chirp z-algorithm. Finally, in COMPOSITE tool, the frequency-responses and associated coherence functions are obtained for the optimum window size from defined window sizes. Then, this frequency responses are used in NAVFIT to obtain transfer function model and DERIVID is used to obtain state space model.

Another program, Simulink® Parameter Estimation, is used to check and tune the parameters, obtained from CIFER®. Unlike CIFER®, SimPE estimates the parameters in time-domain. In both program, same flight test data are used. To check the parameters identified by CIFER®, the model structure and the initial conditions for SimPE are taken from CIFER® results. Therefore, the identified transfer function by CIFER® is checked by using different program in different domain.

Simulink® Parameter Estimation (SimPE) is a Simulink-based product used to estimate the parameters in Simulink model. Simulink Parameter Estimation compares empirical data with data generated by the model. Using optimization techniques, Simulink® Parameter Estimation estimates the parameter and optionally initial conditions of states such that a user-selected cost function is minimized. The cost function typically calculates a least-square error between the empirical and model data. In this study nonlinear least square method is used. Simulink Parameter Estimation requires MATLAB®, Simulink®, and Optimization Toolbox. Transfer function approach is best suited to SISO (Single-Input-Single-Output) system modeling [28]. Therefore, the identification procedure is applied to SISO system in this study. The fixed-wing aircraft is assumed that it has planar symmetry and longitudinal and lateral/directional DoF are not coupled. Therefore, the analyses are separated in two parts:

- Longitudinal : Longitudinal and vertical translation and pitch rotation
- Lateral : Lateral translation, roll and yaw rotations

4.4.1 Longitudinal Transfer Function Modeling

For three DoF longitudinal modeling, two modes dominate the longitudinal dynamics, which are short period and phugoid. The phugoid mode is a longer period mode where kinetic energy and potential energy are interchanged. Therefore, the oscillation occurs at speed, pitch and altitude while angle of attack remains constant. Hodgkinson approximates the phugoid frequency for subsonic flight as a function of x component of airspeed and gravitational acceleration. He also approximates the damping of phugoid mode as a function of the drag of the aircraft [14]. Therefore, it is easily noticed that, the phugoid mode frequency is approximately independent from aircraft configuration. Moreover, damping of phugoid mode is depended on drag only.

Since, pitch angle and speed are the parameters where the oscillation of phugoid mode is seen, the transfer function for phugoid mode is identified by estimating θ/δ_e and/or u/δ_t.

Short-period mode is an underdamped mode where the oscillation lasts few seconds. The transient changes and oscillations are seen in pitch, normal load factor and especially in angle of attack. Since short period mode lasts few seconds, it is assumed that the speed does not change during short period mode. The transfer function for short period mode is modeled as [14]:

$$\frac{\alpha}{\delta_e}(s) = \frac{M_{\delta_e}}{(s^2 + \zeta_{sp}\omega_{sp}s + \omega_{sp}^2)} \tag{4.36}$$

Then the model structure for α/δ_e is chosen as given in Eqn. (4.36) and for this structure, CIFER estimates the transfer function as given in Eqn. (4.37) with cost value obtained using Eqn. (4.1):

$$\frac{\alpha}{\delta_e}(s) = \frac{-8.50}{s^2 + 4.35s + 6.96} \tag{4.37}$$

CIFER Cost: *15*

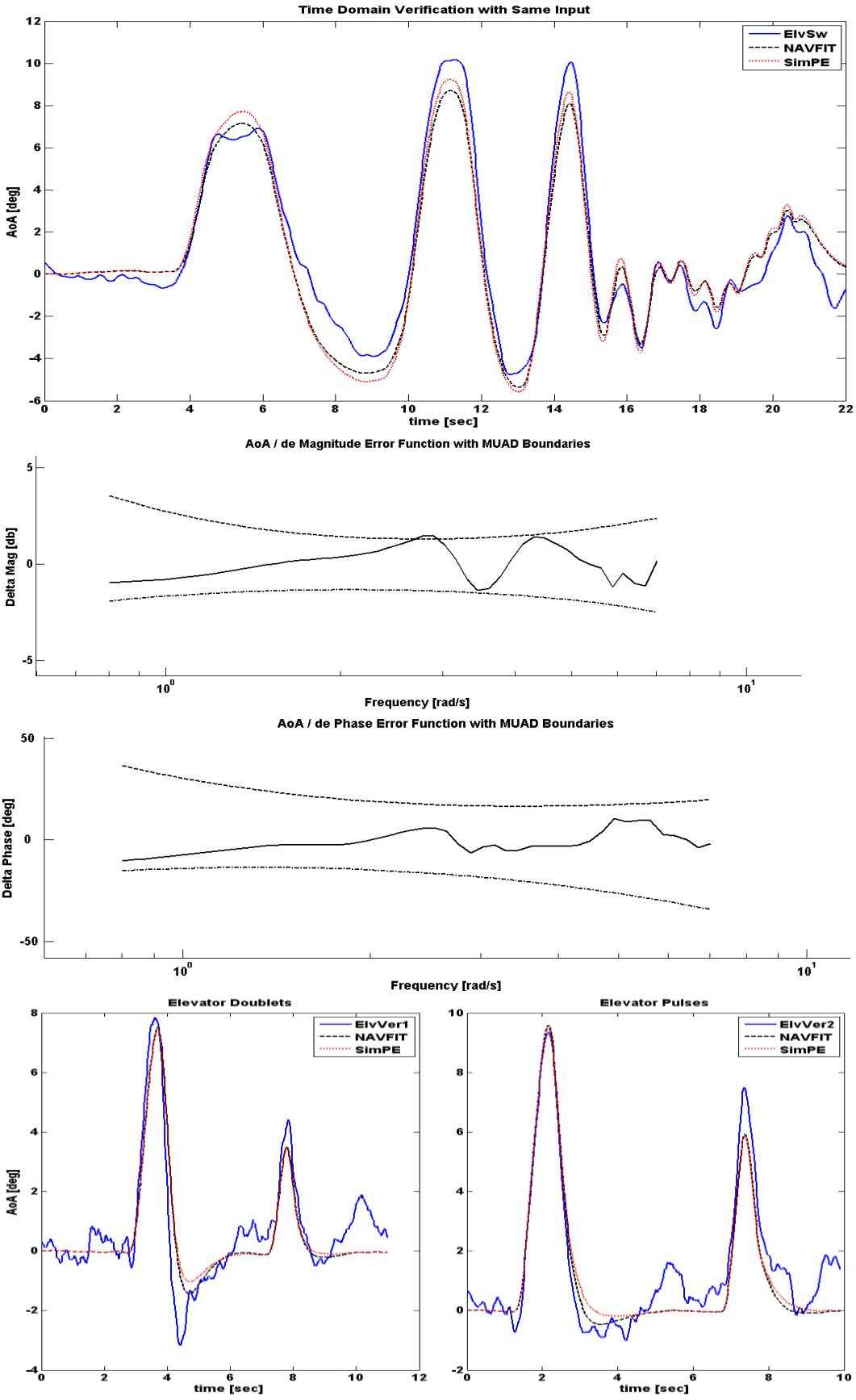

Figure 4.3 Angle of Attack Response to Elevator Input (AoA/δe)

The first graph in Figure 4.3 shows the flight test data, AoA response to elevator sweep, and responses obtained using estimated transfer functions of NAVFIT and SimPE. The aim of this graph is to show the time domain verification of the identified model responses to the identification input by comparing them flight data. The verification done by using identification shows the accuracy of the model.

The second and third graphs show the magnitude and phase error between the identified model and flight test data, with MUAD boundaries. The error between the real A/C dynamic and identified dynamic within the MUAD boundaries is not detectable for pilots. That means a model within MUAD boundaries is a proper model to use in pilot training and handling quality analysis. The graphs also show that at which frequencies, the identified model matches the real A/C dynamics well.

The last two graphs in Figure 4.3 are time domain verification of identified model with flight test data. The difference from the first graph is that in these graphs, different input types are used for verification since the aim is to show the robustness of identified model. In flight tests, 1-2-1 inputs, doublet inputs and pulses are applied for verification purposes. In Figure 4.3, a doublet and a pulse are shown.

When the first and last graphs in Figure 4.3 are examined, it is noticed that the identified transfer functions of AoA response match fairly well with real A/C response. Moreover, the identified responses are within the MUAD boundaries in the frequency range of interest. It also shows that in the defined frequency range, the identified model matches the real A/C dynamics well.

This graph set is used to show the transfer function modeling results. In Figure 4.3, AoA response to elevator inputs are shown, in Figure 4.6 and Figure 4.9, roll rate response to aileron inputs are shown, in Figure 4.8 and Figure 4.10, sideslip response to rudder inputs are shown.

4.4.2 Lateral-Directional Transfer Function Modeling

If the transfer function model structure decided in Section 4.2 is applied to NAVFIT®, which is a module in CIFER® used for transfer function identification, the transfer function is estimated for p/δa is given in Eqn. (4.38) with the result of cost function given in Eqn. (4.1):

$$\frac{p}{\delta_a}(s) = \frac{-27.6s^3 + 183.54s^2 - 306.91s}{s^4 + 8.4s^3 + 36.7s^2 - 62.8s - 192.5} \tag{4.38}$$

CIFER cost: *6*

The equation can be written as pole zero representation:

$$\frac{p}{\delta_a}(s) = \frac{-27.6s(s^2 - 6.65s^2 + 11.12)}{(s + 2.34)(s - 1.79)(s^2 - 8.95s^2 + 45.82)} \tag{4.39}$$

As seen in the equation, due to the positive root in the denominator, the system is unstable, although the cost function is very low.

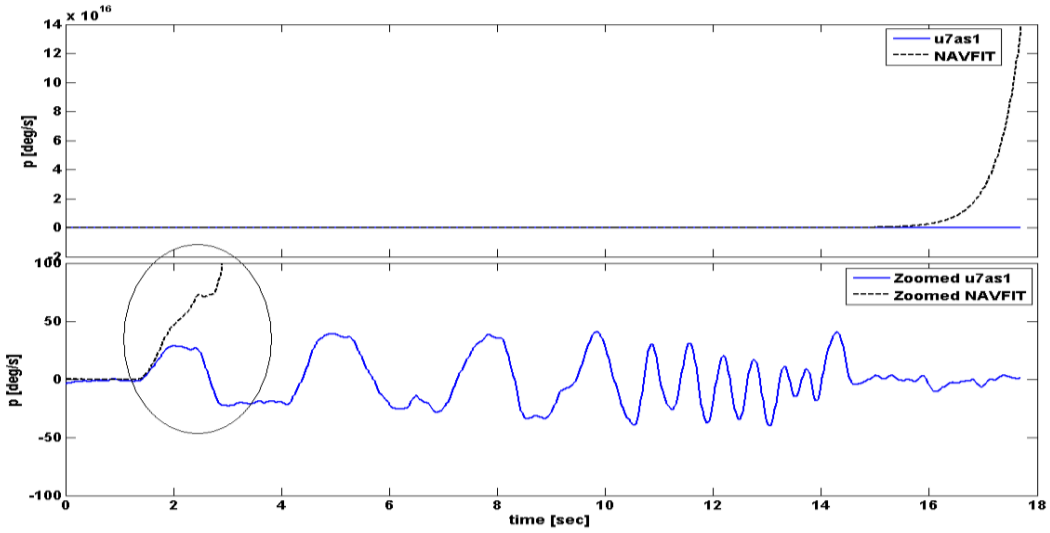

Figure 4.4 Roll Rate Response to Aileron Input (p/δa) CIFER Result

Figure 4.4 shows that for the selected model structure, roll rate response to aileron input is not identified successfully. In the first input excitation, the identified model has diverged. Then, same model structure is used for Simulink® Parameter Estimation. The estimation of p/δa transfer function is:

$$\frac{p}{\delta_a}(s) = \frac{-124.57s^3 + 633.34s^2 - 812.11s}{s^4 + 41.32s^3 - 7.88s^2 - 175.16s + 47.73} \tag{4.40}$$

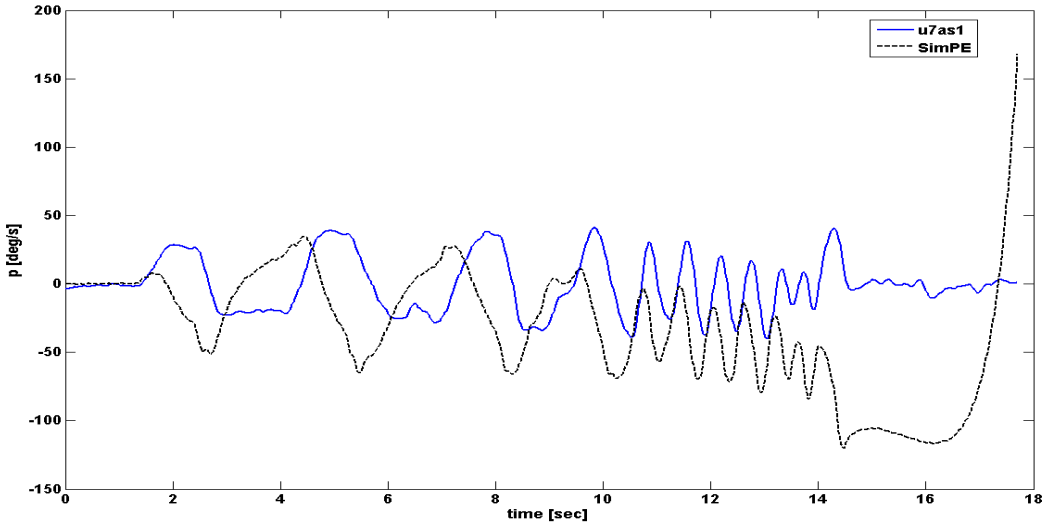

Figure 4.5 Roll Rate Response to Aileron Input (p/δa) SimPE Result

Although the classical flight mechanics approach defines roll rate response with the model structure given in Eqn. (4.4), the graphs show that identification result based on this structure does not match with the flight data. Therefore, the model structure is reconsidered. The new model is formed according to dominant dynamic modes. For lateral motion, the relation between input and output is defined by roll mode, Dutch-roll mode, and spiral mode. The representations of the transfer functions in terms of modes are given as:

$$\frac{p}{\delta_a}(s) = \frac{K_\emptyset s(s^2 + \zeta_\emptyset \omega_\emptyset s + \omega_\emptyset^2)}{(T_R s + 1)(T_s s + 1)(s^2 + \zeta_d \omega_{n_d} s + \omega_{n_d}^2)} \tag{4.41}$$

$$\frac{\beta}{\delta_r}(s) = \frac{K_{\beta_r}(T_{\beta_{r1}} s + 1)(T_{\beta_{r2}} s + 1)(T_{\beta_{r3}} s + 1)}{(T_R s + 1)(T_s s + 1)(s^2 + \zeta_d \omega_{n_d} s + \omega_{n_d}^2)} \tag{4.42}$$

If the roll and sideslip dynamics are assumed to be completely decoupled [14], then it is assumed that rolling motion is created by only aileron input and Dutch-roll motion (with no roll rate) is created by rudder input. Therefore, the relation between roll rate and aileron deflection, and the relation between sideslip and rudder deflection are written as [5]:

$$\frac{p}{\delta_a}(s) = \frac{L_{\delta_a}}{s - L_p} \tag{4.43}$$

$$\frac{\beta}{\delta_r}(s) = \frac{Y_{\delta_r}}{s^2 + (-Y_v - N_r)s + N_\beta} \tag{4.44}$$

Then the model structure for p/δa is chosen as given in Eqn. (4.43) and for this structure, estimated transfer function by CIFER software is given in Eqn. (4.45) with the result of cost function given in Eqn. (4.1):

$$\frac{p}{\delta_a}(s) = \frac{-33.1996}{s + 9.5967} \tag{4.45}$$

CIFER cost: *61*

The result of NAVFIT is used for the initial condition values of parameters in Simulink® Parameter Estimation (SimPE). The estimated transfer function using SimPE is given in Eqn. (4.46) with the result of cost function given in Eqn. (4.1):

$$\frac{p}{\delta_a}(s) = \frac{-29.418}{s + 8.7068} \tag{4.46}$$

SimPE cost: *65*

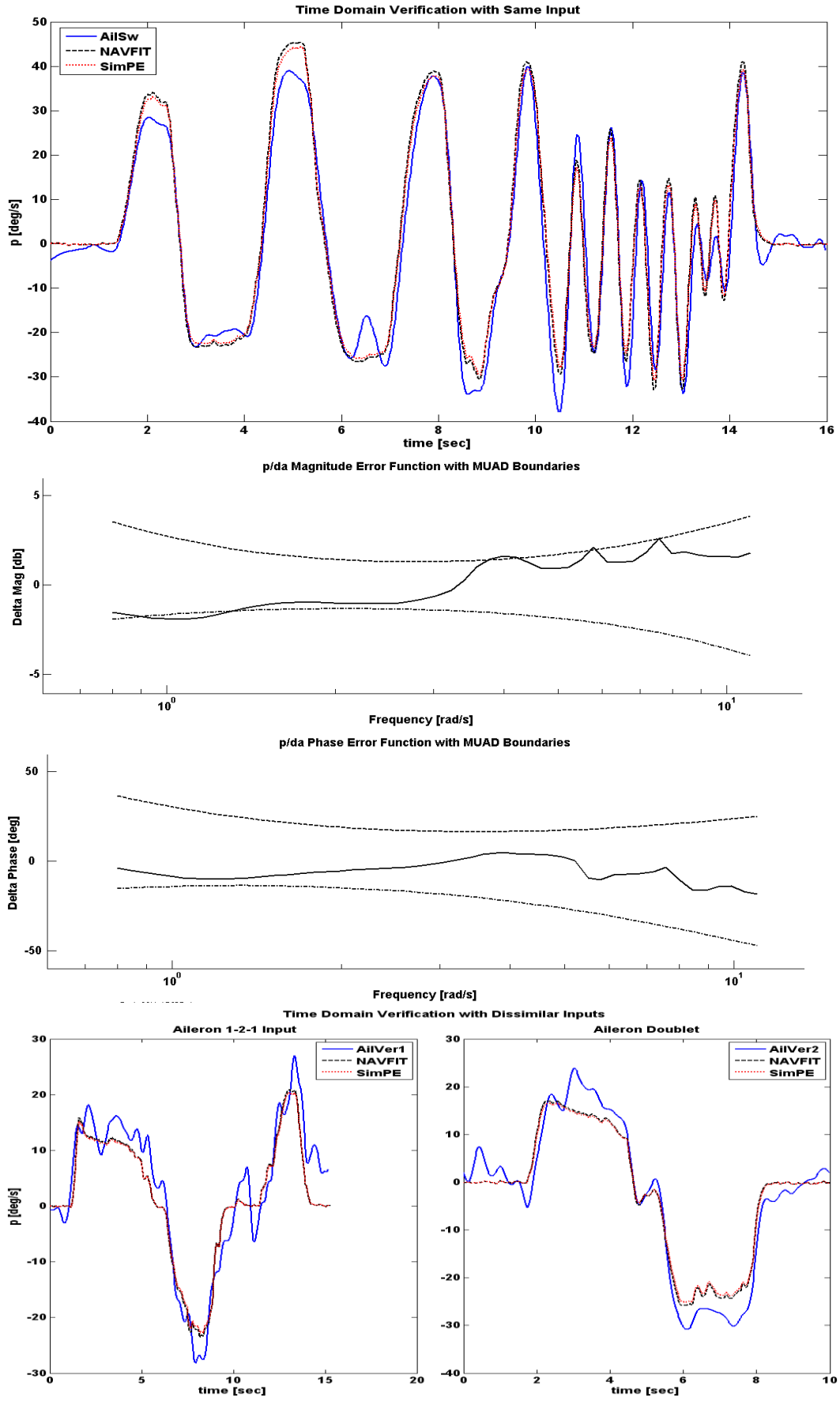

Figure 4.6 Roll Rate Response to Aileron Input (p/δa)

The first graph in Figure 4.6 shows the flight test data, which is a roll rate response to aileron sweep, and responses obtained using estimated transfer functions of NAVFIT and SimPE. The aim of this graph is to show the time domain verification of the identified model responses to the identification input by comparing them flight data. The verification done by using identification shows the accuracy of the model.

After identification, validation procedure is applied by using both time domain verification and MUAD (Maximum Unnoticeable Added Dynamics) boundaries for error values [19]. The MUAD boundaries show the limit where the high order aircraft dynamics and its low order equivalent system are accepted as matched [19]. The second and third graphs show the magnitude and phase error between the identified model and flight test data, with MUAD boundaries.

The last two graphs in Figure 4.6 are time domain verification of identified model with flight test data. The difference from the first graph is that in these graphs, different input types are used since the aim is to verify the robustness of identified model. In flight tests, 1-2-1 inputs, doublet inputs and pulses are applied for verification purposes. In Figure 4.6, a 1-2-1 input and a doublet are applied for p/δ_a verification.

When Figure 4.6 is examined, the time verification results are matched fairly well. However, in the magnitude phase error graph, some points are beyond the MUAD boundaries even though they are considerably close to boundaries. The main reason of that is in identified model, the Dutch-roll mode does not take place. Therefore, the identified model cannot represent the all the dynamics modes in the aircraft response.

According to assumptions accepted for this part of study, β/δ_r input-output pair is used to identify the dutch-roll dynamics. For this pair when the coherence values are concerned, the frequency range for the identification is chosen as 0.8-8 rad/s, which can be seen in Figure 4.7. The frequencies below coherence value of 0.6 are not used in identification.

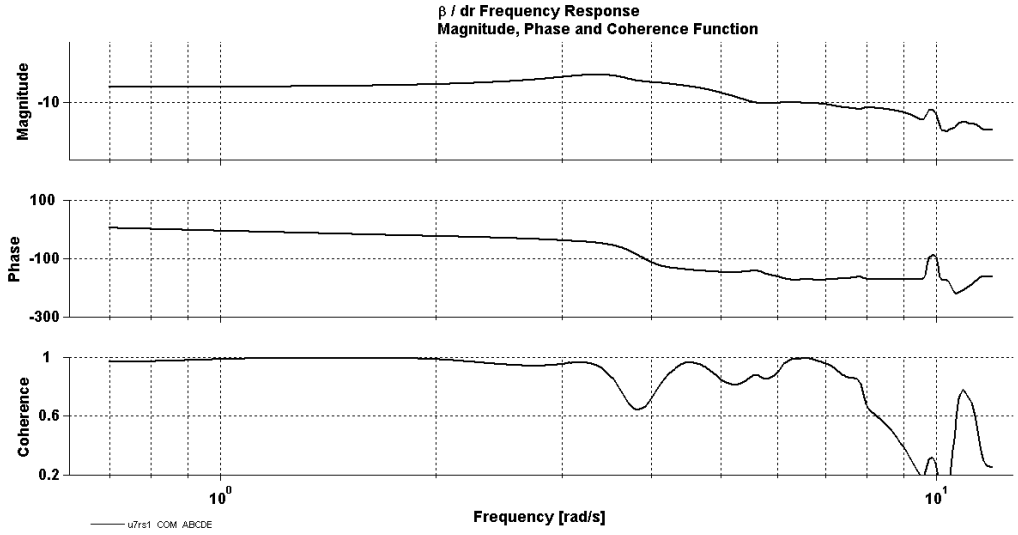

Figure 4.7 Mag, Phase and Coherence Functions of β/δr

Then the model structure for β/δr is chosen as given in Eqn. (4.44) and for this structure, estimated transfer function by CIFER software is given in Eqn. (4.47) with the result of cost function given in Eqn. (4.1):

$$\frac{\beta}{\delta_r}(s) = \frac{-9.16}{s^2 + 1.68s + 13.32} \qquad (4.47)$$

CIFER cost: *38*

The result of NAVFIT is used for the initial condition values of parameters in Simulink Parameter Estimation (SimPE). The estimated values are given as:

$$\frac{\beta}{\delta_r}(s) = \frac{-8.48}{s^2 + 1.38s + 12.89} \qquad (4.48)$$

SimPE cost: 46

When Figure 4.8 is examined, the time verification by using the same input and time verification with dissimilar inputs results match with aircraft responses fairly well. However, in the magnitude error graph and phase error graph, some points are beyond the MUAD boundaries. The maximum error in magnitude is 1 dB and in phase is 9 deg. The main reason of that is the data set used for identification is not proper for identification since all frequencies in frequency range of interest cannot be excited. When the first graph is concerned, the lack of high frequencies can be seen in frequency sweep.

So far, the roll mode and Dutch-roll mode are identified separately by using suitable transfer function models with low cost values and it is seen that the identified models match with flight test data well. In this part, spiral mode identification is explained. The poles of the identified roll mode and Dutch-roll mode are written in Eqn. (4.41), the expression in Eqn. (4.49) is obtained:

$$\frac{p}{\delta_a}(s) = \frac{K_\emptyset s(s^2 + \zeta_\emptyset \omega_\emptyset s + \omega_\emptyset^2)}{(s + 9.5967)(s + {}^1/_{T_s})(s^2 + 1.68s + 13.32)} \tag{4.49}$$

Since the NAVFIT has not a capability to identify a parameter in simplify expression of polynomial (ex: Ts term in Eqn. (4.49)). In NAVFIT, the only identified parameters are coefficients of s terms and time delay. Therefore, NAVFIT cannot be used to estimate a mode by taking poles or zeros of other modes constant. To overcome this, Tischler suggests using arithmetic manipulation of the frequency-response functions at each identification frequency ω [28]. The example of this is given as:

$$(s^2 + \zeta_d \omega_{n_d} s + \omega_{n_d}^2)\frac{p}{\delta_a}(s) = \frac{L_\emptyset s(s^2 + \zeta_\emptyset \omega_\emptyset s + \omega_\emptyset^2)}{(s + {}^1/_{T_r})(s + {}^1/_{T_s})} \tag{4.50}$$

Using the structure given in Eqn. (4.50), the spiral mode is estimated and roll mode is updated by taking the parameters of Dutch roll mode constant.

$$(s^2 + 1.68s + 13.32)\frac{p}{\delta_a}(s) = \frac{-26.984s(s^2 + 1.807s + 11.79)}{(s + 8.052)(s - 0.11)} \tag{4.51}$$

When Eqn. (4.45) an Eqn. (4.51) is compared, it is seen that the roll mode constant value is changed from 9.5967 to 8.052. And the spiral mode time constant is identified. Then p/δa transfer function is formed using Eqn. (4.47) and (4.51) as:

$$\frac{p}{\delta_a}(s) = \frac{-26.984s(s^2 + 1.807s + 11.79)}{(s + 8.052)(s - 0.11)(s^2 + 1.68s + 13.32)} \tag{4.52}$$

CIFER cost: *28*

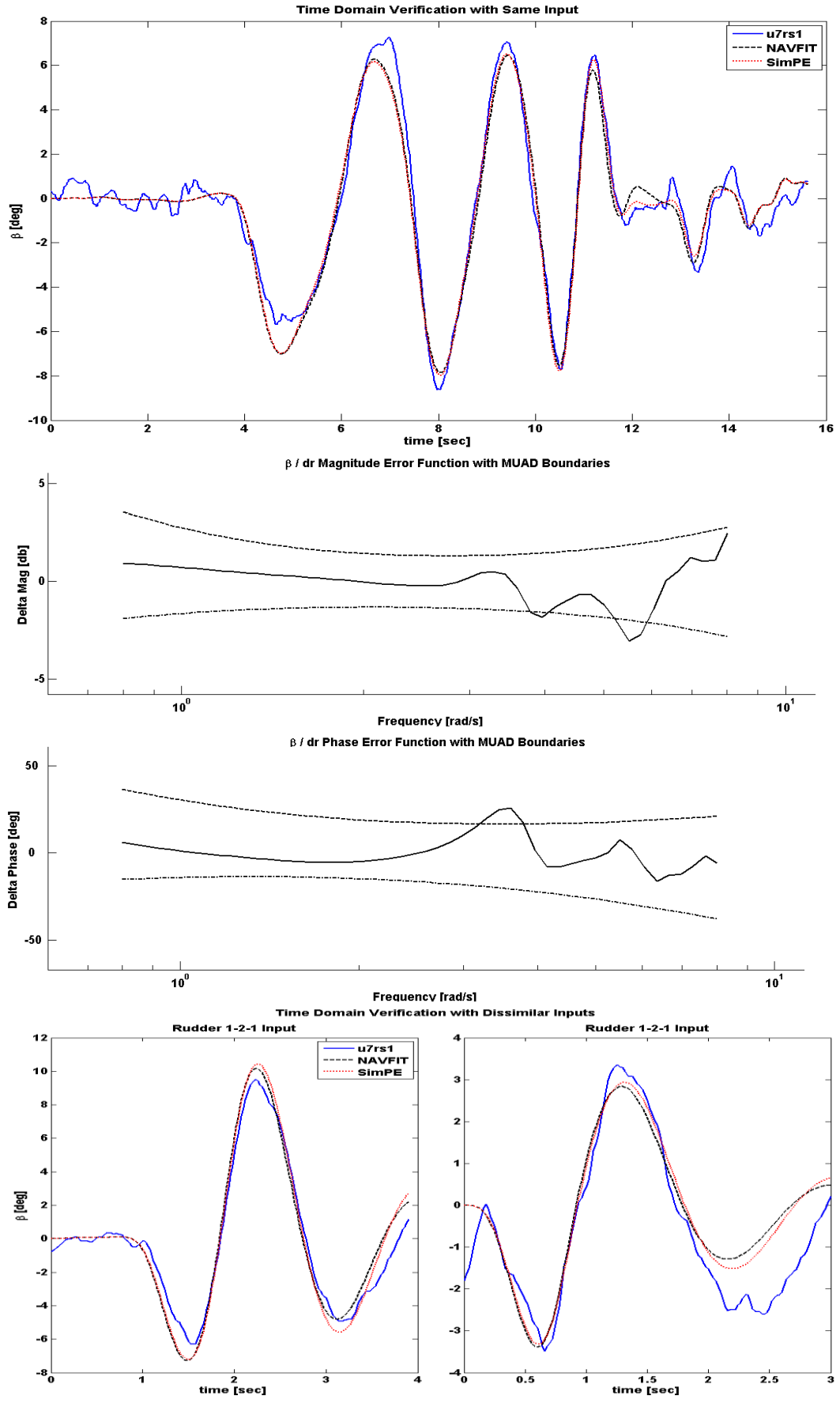

Figure 4.8 Sideslip Response to Rudder Input (β/δr)

In this study, SimPE is also used to identify the spiral mode by using Eqn. (4.49), which is formed by using Eqn. (4.46) and (4.48)

$$\frac{p}{\delta_a}(s) = \frac{K_\emptyset s(s^2 + \zeta_\emptyset \omega_\emptyset s + \omega_\emptyset^2)}{(s + 8.7068)(s + {}^1/_{T_s})(s^2 + 1.38s + 12.89)} \tag{4.53}$$

When the numerator and denominator expanded, the expression in Eqn. (4.54) is obtained:

$$\frac{p}{\delta_a}(s) = \frac{A_1 s^3 + B_1 s^2 + C_1 s}{s^4 + (10 + C_s)s^3 + (25 + 10C_s)s^2 + (112 + 24C_s)s + 112C_s} \tag{4.54}$$

To estimate spiral mode, C_s is setting as free parameter for estimation. Moreover, coefficients of the numerator part are setting as free parameter to estimate the numerator of p/δa. The roll mode and Dutch roll mode parameters are kept fixed. The estimation result is given in Eqn. (4.55):

$$C_s = {}^1/_{T_s} = -0.049\ rad/s$$

$$\frac{p}{\delta_a}(s) = \frac{-31.562s(s^2 + 1.333s + 11.77)}{s^4 + 9.95s^3 + 24.5s^2 + 110.8s - 15.6} \tag{4.55}$$

SimPE cost: *38*

The denominators in Eqn. (4.32) and Eqn. (4.33) show that lateral and directional motions have common denominators. By taking this denominator constant for β/δr response, numerator of β/δr can be obtained using CIFER and SimPE. The obtained results are given as:

$$\frac{\beta}{\delta_r}(s) = \frac{8.1729(s - 0.2514)(s + 9.261)}{(s + 8.052)(s - 0.11)(s^2 + 1.68s + 13.32)} \tag{4.56}$$

CIFER cost: *43*

$$\frac{\beta}{\delta_r}(s) = \frac{6.33(s - 0.1358)(s + 11.73)}{(s + 8.608)(s - 0.049)(s^2 + 1.39s + 13.02)} \tag{4.57}$$

SimPE cost: *24*

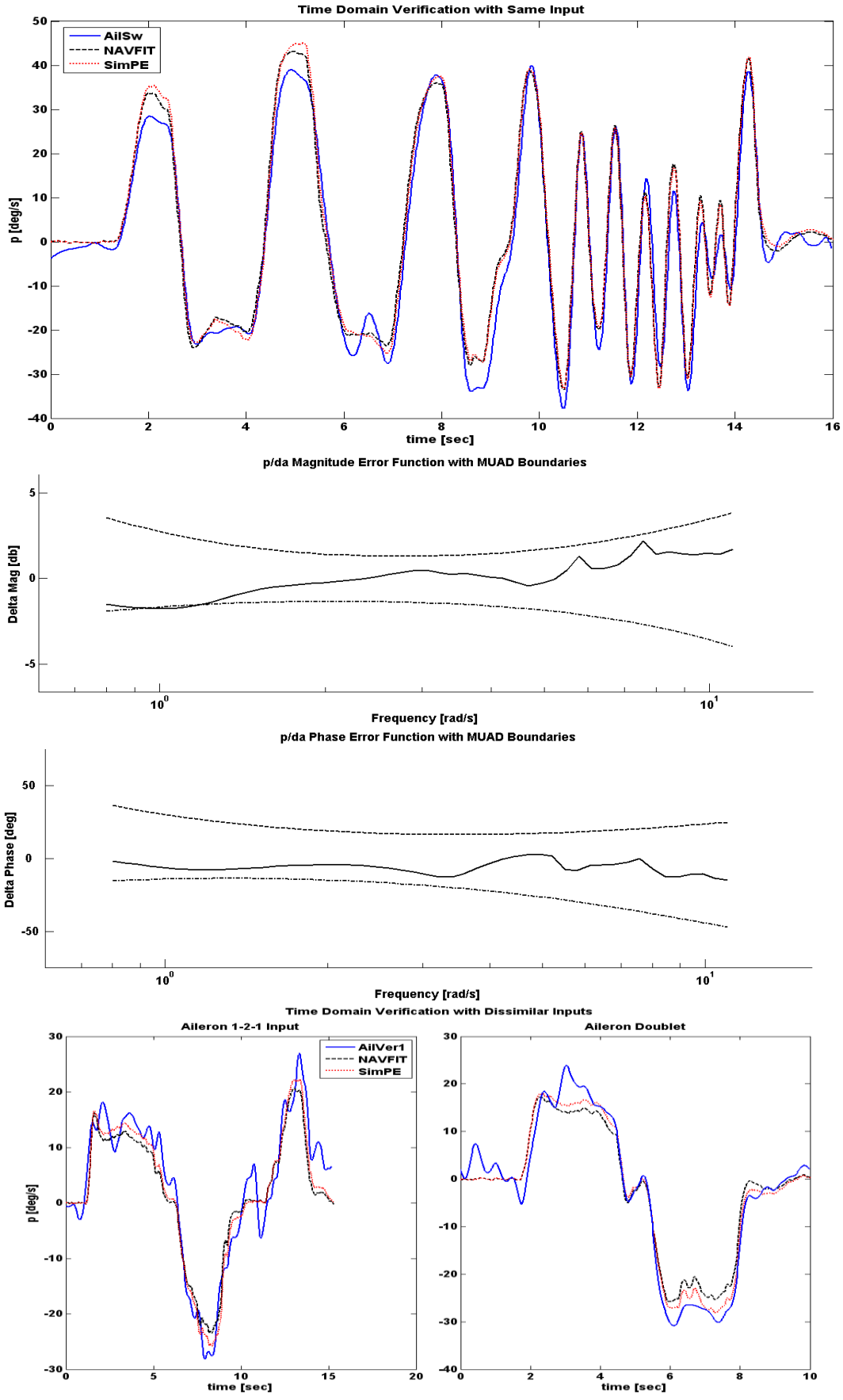

Figure 4.9 Roll Rate Response to Aileron Input (p/δa)

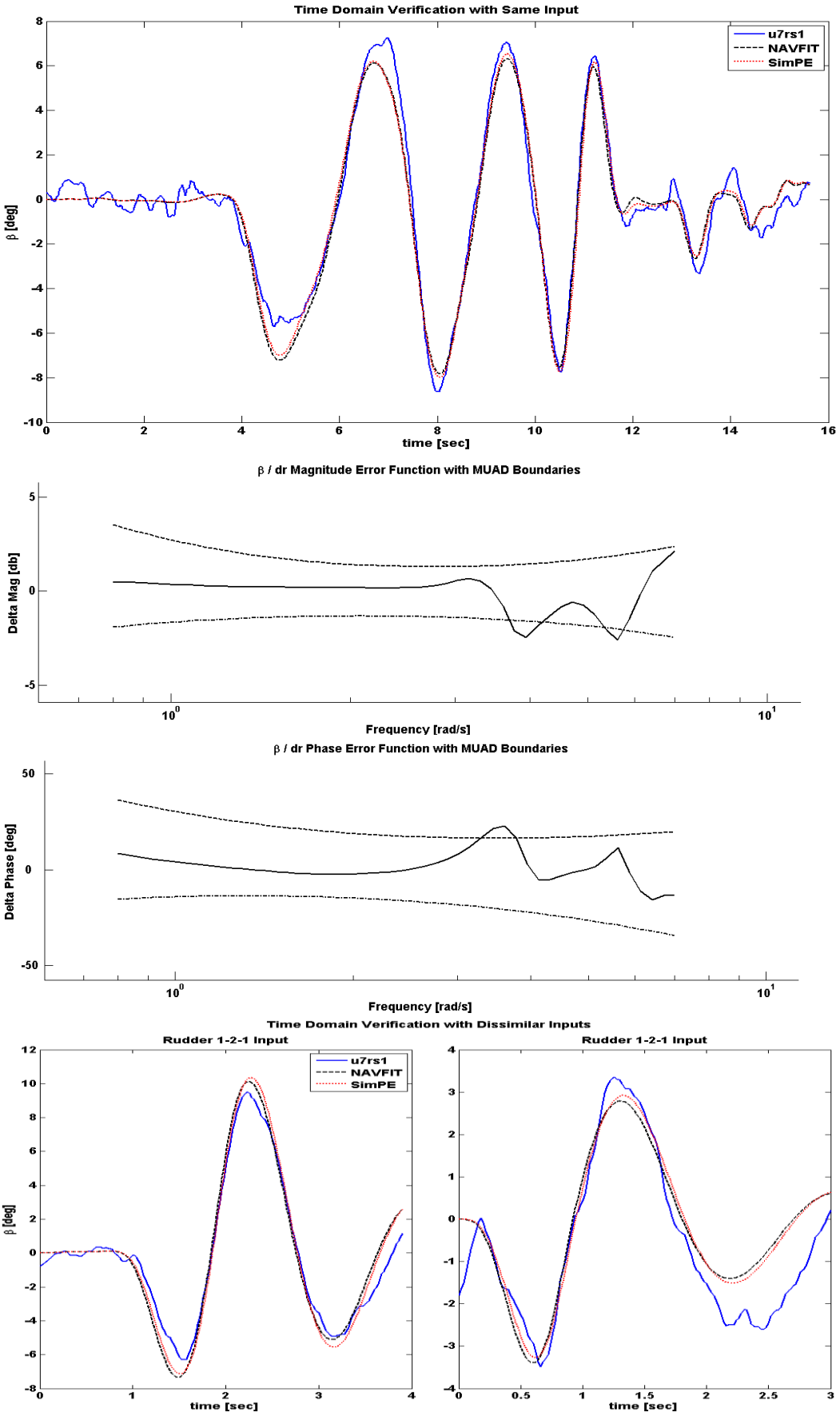

Figure 4.10 Sideslip Response to Rudder Input (β/δr)

The first graphs in Figure 4.9 and Figure 4.10, show the flight test data, which are lateral/directional responses of aircraft (p and β) and responses obtained using estimated transfer functions from NAVFIT and SimPE. The aim of this graph is to show the time domain verification of the identified model responses to the identification input by comparing them flight data. The verification done by using identification shows the accuracy of the model.

The second and third graphs show the magnitude and phase error between the identified model and flight test data, with MUAD boundaries. In MUAD boundaries graphs, it is seen that the error between the real A/C dynamic and identified dynamic in the specified frequency range is generally in the limits, some points are beyond the MUAD boundaries. The main reason of that is explained before, as the data set used for identification is not proper for identification since all frequencies in frequency range of interest cannot be excited. When the first graph is concerned, the lack of high frequencies is seen in frequency sweep.

The last graphs in Figure 4.9 and Figure 4.10 are time domain verification of identified model with flight test data. The difference with first graphs is that in these graphs, different input types are used since the aim is to verify the robustness of identified model. It is seen that the match between identified model and aircraft response is well and this shows that robustness of the model is verified. Another point deduced from the graphs is that the linear identified model is valid up to high values of responses such as 10° sideslip and 30°/s roll rate although the linear models are known as they are valid for small perturbations at the trim condition.

4.5 Handling Quality Analysis

Transfer function modeling is well suited to handling qualities applications because both the pilot opinion about dynamic responses and pilot-in-the-loop performance needs only relations between responses and control inputs; moreover, detailed stability and control derivatives are not required.

Handling quality analysis is done by applying the procedure, given in the flying quality standard, to the identified transfer functions. The handling quality requirements are specified by concerning vehicle class and flight phase category.

Vehicle Class: The vehicle class of the UAV is **Class 1**.

The vehicle class is determined by considering UAV weight and maneuvering. For the aircraft, has weight less than 136kg (300lbs), the maneuverability is not a parameter to determine the vehicle class. Since the weight of Pelikan is 65kg, the vehicle class is specified as Class 1.

Flight Phase Category: The flight phase category is **Category B.**

The handling quality is analyzed for Category B since the flight tests have been done in cruise flight. In [28], cruise flights are defined as Category B, takeoff and landing are defined as Category C and missions are put in Category A.

Level of Handling Quality: Level of handling quality defines the acceptable level of the ability to complete the operational mission for which the vehicle is designed. There are 3 levels for automatic and manual control. The classification of levels is found in Table 4.1.

Table 4.1 Classification of Levels of Flying Qualities [24]

AUTOMATIC LEVELS			MANUAL LEVELS		
1	2	3	1	2	3
Accomplish Flight Phase Normal Operation	Degraded Flight Phase Degrading Failures	Recoverable Minimum Backup Mode Req.	Accomplish Flight Phase Normal Operation ***CH Scale:*** 1 - 3.5	Degraded Flight Phase Increased Operator Workload ***CH Scale:*** 3.5 - 6.5	Recoverable Minimum Manual Req. ***CH Scale:*** 6.5 - 9+
				*CH: Cooper-Harper	

According to vehicle class and flight phase category of Pelikan, the levels of flying qualities for longitudinal motion are obtained by comparing mode characteristics of Pelikan with the requirements. The levels of flying qualities for longitudinal motion are given in Table 4.2, together with the requirements.

Table 4.2 Longitudinal Response Characteristics

	Flight Phase					
SHORT-PERIOD	Level	Category	Class	Min ζ_{sp}	Max ζ_{sp}	*Pelikan*
	1	B	I	0.30	2.00	
	2	B	I	0.20	2.00	*1.649*
	3	B	I	0.15	-	

As seen in Table 4.2, the level of short period damping is Level 1. From Eqn. (4.37), the short period frequency is found as 3 rad/s. According to the book [24], it is pointed out that for $\omega_{n_{sp}} = 3.0$, Level 1 handling quality for frequency of short period is obtained by at least n/α value of 2.5 rad/s.

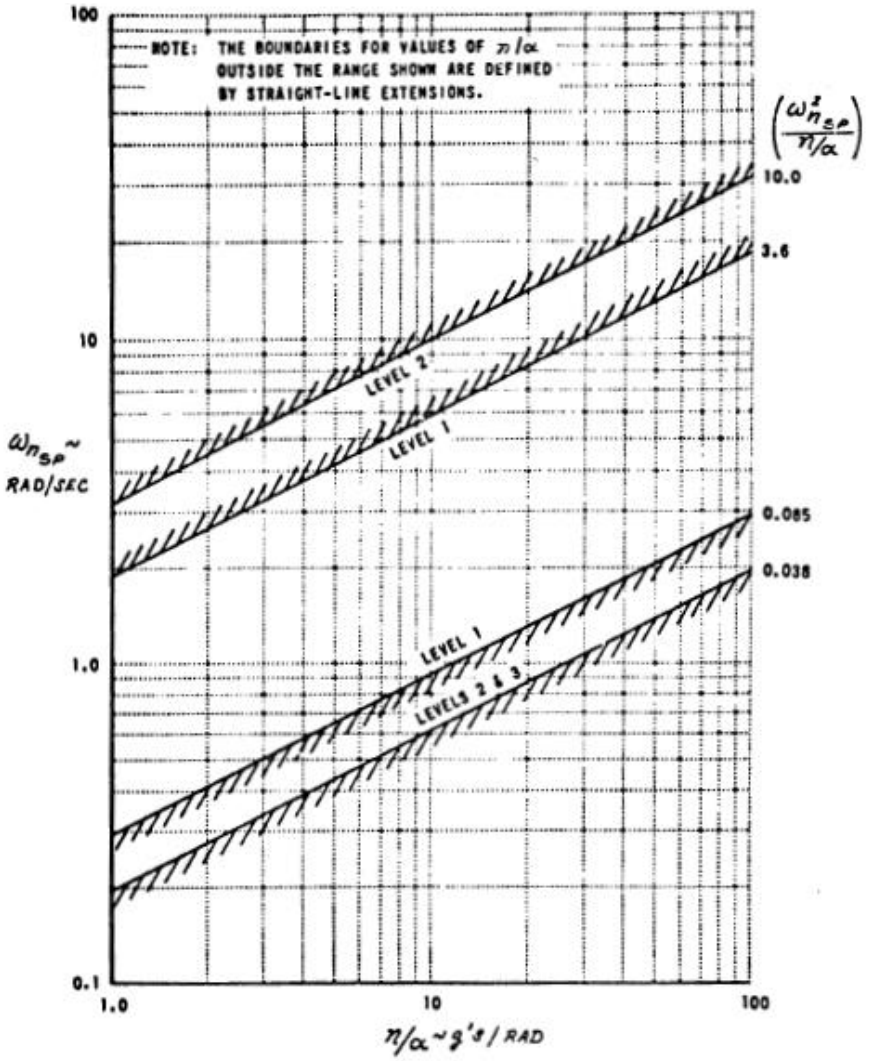

Figure 4.11 Short period frequency requirements – Category B flight phase

According to the vehicle class and flight phase category of Pelikan, the levels of flying qualities for lateral-directional motion are obtained by comparing mode characteristics of Pelikan with the requirements. The requirements for lateral/directional motion together with Pelikan results are given in Table 4.3.

Table 4.3 Lateral-Directional Response Characteristics

	Level	Flight Phase Category	Class	Min ζ_d	*Pelikan*	Min $\zeta_d\omega_{nd}$	*Pelikan*	Min ω_{nd}	*Pelikan*
DUCTH-ROLL	1	B	I	0.08	*0.460*	0.15	*1.68*	1.0	*3.650*
	2	B	I	0.02		0.05		0.4	
	3	B	I	0.02		-		0.4	

	Level	Flight Phase Category	Class	Max T_r	*Pelikan*
ROLL	1	B	I	1.4	*0.124*
	2	B	I	3	
	3	B	I	10	

	Level	Flight Phase Category	Class	Min t_{double}	*Pelikan*
SPIRAL	1	B	I	20	*6.341*
	2	B	I	12	
	3	B	I	4	

	Level	Flight Phase Category	Class	Min ζ_{sp}	Max ζ_{sp}	*Pelikan*
SHORT-PERIOD	1	B	I	0.30	2.00	*1.649*
	2	B	I	0.20	2.00	
	3	B	I	0.15	-	

As seen in Table 4.3, the Dutch-roll and roll response characteristics are Level 1. Although the spiral mode of this UAV is unstable, handling quality level of this mode is Level 3. In MIL-HDBK-1797, the values beyond the Level 3 has discussed by using Cornell Aero Lab TB-574-F-6 test results [19]. They state that the pilot can control the aircraft where spiral t_{double} values are between 2 and 4, if the pilot devotes full attention to flying the aircraft. This situation is exactly the same with situation in Pelikan, since Pelikan is only used as a test platform, so there is nothing to distract the pilot's attention like missions etc. Therefore, for a test platform, Level 3 HQ level for unstable spiral mode is assumed to be tolerable.

CHAPTER 5

STATE SPACE MODELING

5.1 Introduction

This chapter presents state-space model identification of the UAV. Since transfer function modeling primarily characterizes the SISO (single input single output) systems, it is not easy to extend this modeling to MIMO (multi input multi output) systems; therefore, state-space modeling is used to identify more complex, high order and MIMO systems [10]. Moreover, in transfer function modeling, the correlations and over parameterized models cannot be detected easily. Therefore, state-space modeling is much more preferred model in the identification, especially for MIMO systems. The MIMO flight control systems such as LQR are based on state space representation and since the accuracy of state space model is important for such system design, state space identification is generally required [28]. Moreover, since control and stability derivatives are modeled and from them, aerodynamic derivatives are derived, state space identification is also needed for simulation model development and verification [28].

5.2 State-Space Model Structure

The state-space model structure is formulated from the first order differential equation of motion. A general model of a dynamic system in terms of the differential equation of motion can be written as:

$$m_{11}\dot{x}_1 + \cdots + m_{1n}\dot{x}_n = (f_{11}x_1 + \cdots + f_{1n}x_n) + \left(g_{11}u_1 + \cdots + g_{1n}u_{n_c}\right) \quad (5.1)$$

This equation has n states (x), n_c inputs (u), n stability derivatives (f) and n_c control derivatives (g). Expression in Eqn. (5.1) is written in a matrix form after some calculation as given in Eqn. (5.2):

$$\begin{aligned} \dot{\boldsymbol{x}} &= \boldsymbol{Ax} + \boldsymbol{Bu} \\ \boldsymbol{y} &= \boldsymbol{Cx} + \boldsymbol{Du} \end{aligned} \quad (5.2)$$

In CIFER®, state space model structure is formed as given in Eqn. (5.3) and the GUIs in the program are formed according to this structure.

$$\begin{aligned} \boldsymbol{M\dot{x}} &= \boldsymbol{Fx} + \boldsymbol{Gu} \\ \boldsymbol{y} &= \boldsymbol{H_0 x} + \boldsymbol{H_1 \dot{x}} \end{aligned} \quad (5.3)$$

The expression given in Eqn. (5.3) is obtained by using the relations given as

$$\begin{aligned} \boldsymbol{A} &= \boldsymbol{M^{-1}F} \\ \boldsymbol{B} &= \boldsymbol{M^{-1}G} \\ \boldsymbol{C} &= \boldsymbol{H_0} + \boldsymbol{H_1 M^{-1} F} \\ \boldsymbol{D} &= \boldsymbol{H_1 M^{-1} G} \end{aligned} \quad (5.4)$$

The matrices M, F, G contain both the parameters to be identified and the constants. The initial conditions of the parameters to be identified are obtained from transfer function modeling and/or simulation model if it exists. A measurement vector, y, is given for immeasurable states. The matrices H_0 and H_1 include known constants like unit conversions, kinematics, etc.

State space identification algorithm is based on comparing the resulting MIMO frequency responses of the state space model with those of the flight test data. The identification algorithm finds the frequency response matrix by minimizing the following cost function [28]:

$$J = \sum_{l=1}^{n_{TF}} \left\{ \frac{20}{n_\omega} \sum_{\omega_1}^{\omega_{n_\omega}} W_\gamma [W_g \left(\left|\hat{T}_c\right| - |T|\right)^2 + W_p (\angle \hat{T}_c - \angle T)^2] \right\} \tag{5.5}$$

where

$\|\ \|$ and $\angle$	:	magnitude (dB) and phase (deg) at each frequency ω
n_ω	:	number of frequency points where the cost function is calculated
n_{TF}	:	number of transfer functions chosen for state-space representation
ω_1 and $\omega_{n\omega}$	:	starting and ending frequencies for identification process
$\hat{T}_c$	:	frequency response matrix obtained from flight tests
T	:	frequency response obtained from the state space matrices, **M**, **F**, **G**

The frequency response is obtained from the state space matrices, **M**, **F**, and **G** by using the following expression [28]:

$$\boldsymbol{T}(s) = [\boldsymbol{H_0} + s\boldsymbol{H_1}][(s\boldsymbol{I} - \boldsymbol{M}^{-1}\boldsymbol{F})^{-1}\boldsymbol{M}^{-1}\boldsymbol{G}] \tag{5.6}$$

As seen in Eqn. (5.5), state space modeling use the same cost function with transfer function modeling. The only difference is that to calculate cost function of state space model, the costs of n_{TF} transfer functions are summed. Then, the cost function of state space model is then represented as average of these summed cost functions [28].

$$J_{ave} = {}^{J}/_{n_{TF}} \tag{5.7}$$

Since the cost function is calculated by using the cost function of each transfer function, it gives chance to choose proper frequency range of interest for each transfer function separately. As a consequence, the cost function value is made smaller by using the proper frequency ranges for each frequency response for identification.

An identification result with average cost function $J_{ave} \leq 50$ is expected to represent a model that is nearly indistinguishable from A/C dynamics [28].

Force Equations:

The force equation in body fixed frame is written as given in Eqn. (5.8) by using Newton's Second Law:

$$\frac{d^B \boldsymbol{V}}{dt} = -(\boldsymbol{\omega} \times \boldsymbol{V}) + {\boldsymbol{F}_{gravity}}/{m} + {\boldsymbol{F}_{aero}}/{m} \tag{5.8}$$

In trim condition, the Euler angles is assumed as $\Theta = \Theta_0 \quad \Phi = 0 \quad \Psi = 0$

The equations are linearized for small perturbation inputs, then aerodynamic forces are expanded in Taylor series for perturbations using the state and control terms.

$$\dot{u} = -W_0 q + V_0 r - (g cos\Theta_0)\theta + X_u u + X_v v + \cdots + X_q q + \cdots + X_{\delta_e}\delta_e + X_{\delta_a}\delta_a \tag{5.9}$$

$$\dot{v} = -U_0 r + W_0 p + (g cos\Theta_0)\phi + Y_u u + Y_v v + Y_{\dot{v}}\dot{v} + \cdots + Y_q q + \cdots + Y_{\delta_e}\delta_e + Y_{\delta_a}\delta_a \tag{5.10}$$

$$\dot{w} = -V_0 p + U_0 q - (g sin\Theta_0)\theta + Z_u u + Z_v v + \cdots + Z_q q + \cdots + Z_{\delta_e}\delta_e + Z_{\delta_a}\delta_a \tag{5.11}$$

Moment Equations:

The moment equation in body fixed frame is written as given in Eqn. (5.12) by using Newton's Second Law:

$$\frac{d^B \boldsymbol{I\omega}}{dt} = -(\boldsymbol{\omega} \times \boldsymbol{I\omega}) + \boldsymbol{M}_{aero} \tag{5.12}$$

The equations are linearized for small perturbation inputs, then aerodynamic forces are expanded in Taylor series for perturbations using the state and control terms.

$$\dot{p} = L'_u u + L'_v v + \cdots + L'_p p + \cdots + L'_{\delta_e}\delta_e + L'_{\delta_a}\delta_a + \cdots \tag{5.13}$$

$$\dot{q} = M_u u + M_v v + \cdots + M_{\dot{w}}\dot{w} + M_q q + \cdots + M_{\delta_e}\delta_e + M_{\delta_a}\delta_a + \cdots \tag{5.14}$$

$$\dot{r} = N'_u u + N'_v v + \cdots + N'_r r + \cdots + N'_{\delta_e}\delta_e + N'_{\delta_a}\delta_a + \cdots \tag{5.15}$$

Euler Angle Relations:

In time Δt, an infinitesimal rotation from the position defined by Θ, Φ, Ψ to the position corresponding to (Θ +ΔΘ), (Φ +ΔΦ), (Ψ +ΔΨ). The vector representing the rotation is [18]:

$$\begin{bmatrix} \dot{\phi} \\ \dot{\theta} \\ \dot{\psi} \end{bmatrix} = \begin{bmatrix} 1 & sin\phi\ tan\theta & cos\phi\ tan\theta \\ 0 & cos\phi & -sin\phi \\ 0 & sin\phi\ sec\theta & cos\phi\ sec\theta \end{bmatrix} \begin{bmatrix} p \\ q \\ r \end{bmatrix} \tag{5.16}$$

In trim condition, the Euler angles are assumed as $\Theta = \Theta_0 \quad \Phi = 0 \quad \Psi = 0$ [18]. Then the relations in Eqns (5.17), (5.18), (5.19) are obtained from Eqn. (5.16) using this assumption.

$$\dot{\phi} = p + r tan\Theta_0 \tag{5.17}$$

$$\dot{\theta} = q \tag{5.18}$$

$$\dot{\psi} = \frac{r}{(cos\Theta_0)} \tag{5.19}$$

5.3 Accuracy Analysis & Model Structure Determination

Accuracy analysis is important to define the model structure determination used in identification. The necessity of the parameter accuracy analysis arises from the following reasons [28]:

- The confidence of a parameter value may be low due to lack of information about that parameter in test data and/or correlation with another parameter. In that case, that parameter is kept apart from identification procedure by eliminating it from model structure or keeping it fixed at a value that is reasonable from physical point of view.

- The accuracy analysis of parameters provides information about robustness, which is used in control system design. Therefore, by this analysis, the expected uncertainty of parameters is estimated more realistically, thus the degradation on control performance due to robustness is kept as small as possible.

The accuracy analyses are done by using scatter analysis or theoretical accuracy analysis. Scatter analysis is hard to apply for aircraft system identification test; because it is not feasible to make so many flight tests that enough numbers of data samples are obtained for scatter analysis. Therefore, to obtain the parameter's accuracy, theoretical analyses are applied. The metric, which is used in this study to represent the accuracy of parameters theoretically, is Cramér-Rao Bound.

5.3.1 Accuracy Analysis Metrics

Cramér-Rao (CR) bound, named in honor of Harald Cramér and Calyampudi Radhakrishna Rao, presents the minimum expected standard deviation σ_i in parameter estimate θ_i. For any unbiased estimator [28]:

$$\sigma_i \geq CR_i \tag{5.20}$$

Since Eqn. (5.20) is valid for unbiased estimator and due to colored noise in the flight data and modeling errors in identification analysis, the following scale factors are used:

For time domain [10]

$$\sigma_i \geq 5 * CR_i \tag{5.21}$$

For frequency domain [28]

$$\sigma_i \geq 2 * CR_i \tag{5.22}$$

When Eqn. (5.21) and (5.22) are compared, it is seen that smaller scale factor is used in frequency domain system identification. The reason of that is in spectral analysis, the noise is eliminated. [28].

The CR bound of ith-identified parameter of the converged solution $\boldsymbol{\Theta_0}$ is determined from the associated diagonal element of the inverse of the Hessian matrix, $\mathcal{H}$.

$$CR_i = \sqrt{(\mathcal{H}^{-1})_{ii}} \tag{5.23}$$

$$\mathcal{H} = \nabla^2_{\boldsymbol{\Theta}} J = \frac{\partial^2 J}{\partial \boldsymbol{\Theta}\, \partial \boldsymbol{\Theta^T}} \tag{5.24}$$

The CR bound is expressed as a percentage of the converged identification value:

$$\overline{CR}_i = \left|\frac{CR_i}{\theta_i}\right| \times 100\% \tag{5.25}$$

Tischler formed reasonable criteria for CR value and cost function limits from the experiments [28]:

$$\overline{CR}_i \leq 20\% \tag{5.26}$$

$$J_{ave} \leq 100 \tag{5.27}$$

Identification result within the limits given in Eqns (5.26) and (5.27) reflects highly reliable state-space model identification with good predictive accuracy. Several of the largest Cramér-Rao bounds may be in the range of 20%-40% without loss of reliability or cause for concern [28].

The level of confidence in the accuracy of an identified parameter is observed directly from Cramér-Rao percentage. The high values of Cramér-Rao percentage indicate two problems: insensitivity and correlation.

Insensitivity:

Insensitivity occurs when [28]

- a parameter θ_i have little or no effect on the cost function J($\boldsymbol{\Theta}$), where $\boldsymbol{\Theta}$ is the parameter set to be identified. Therefore, insensitivity shows that the parameter θ_i is not an identifiable parameter for that identification model structure.
- there is insufficient information content in the data. Therefore, to overcome this, a proper frequency range for identified parameter must be defined and in flight test, the dynamic mode involving the identified parameter must be excited well.

Parameter insensitivity is determined from the diagonal elements of Hessian matrix:

$$I_i = \frac{1}{\sqrt{\mathcal{H}_{ii}}} \tag{5.28}$$

The parameter insensitivities are also best presented as normalized percentages of the converged parameter values:

$$\bar{I}_i = \left|\frac{I_i}{\theta_i}\right| \times 100\% \tag{5.29}$$

Much experience shows that a reasonable goal for insensitivities as obtained from the frequency-response method is given in Eqn. (5.30) [28]:

$$\bar{I}_i < 10\% \tag{5.30}$$

Several of the largest insensitivities are typically in the range of 10-20% without loss of reliability or cause for concern.

Correlation:

A correlation occurs when two or more parameters vary in a linear relationship. The main reason of the correlation is forming an over parameterized model structure.

The pair-wise correlation is found by using correlation coefficient expression given in Eqn. (5.31) for ith and jth parameters [28]:

$$\rho_{ij} = \frac{(\mathcal{H}^{-1})_{ij}}{\sqrt{(\mathcal{H}^{-1})_{ii}(\mathcal{H}^{-1})_{jj}}} \tag{5.31}$$

Correlation coefficient takes values between -1 and 1. The values of -1 and 1 show perfect correlation between two parameters. For multiple parameters, confidence ellipsoid provides the correlation between parameters [28].

$$\bar{\boldsymbol{\Theta}}_{CR_i} = \frac{\boldsymbol{\mathcal{T}}^{-1}\boldsymbol{\mathcal{H}}^{-1}(:,i)}{CR_i} \tag{5.32}$$

A correlation is notable for a parameter whose CR value is high and insensitivity is low. In that case, large relative component of $\bar{\boldsymbol{\Theta}}_{CR_i}$ shows the contribution of the correlated parameter, which is the reason of correlation.

5.3.2 Model Structure Determination Using Accuracy Analysis Metrics

The metrics given in 5.3.1 show two important relations between parameters and identification model structure: insensitivity and correlation. Before identification procedure is applied, all the parameters, which are used to model the dynamic characteristics of the system, are determined according to Equations of Motion. However, not all the determined parameters are proper for the identification model; therefore the model structure is reconstructed according to aircraft dynamics and test data. The approach to determination of model structure is summarized as [28]:

1) Irrelevant parameters are removed or fixed a reasonable value

The first thing to do is that the parameters which not affect the cost function, in other words parameters whose insensitivity is high, are removed from the model structure. The elimination of parameters is done one by one and for each step, the cost function and sensitivities are calculated again. At each time, the parameter with the largest insensitivity, which excesses the given limit (~10%), is removed. When the parameters' insensitivities become close to the limit, the decision of removing the parameter are given according to increase in cost function. If the change in the cost function is greater than the following values then the parameter are not removed.

$$\Delta J_{ave} \approx 1 \text{ to } 2 \tag{5.33}$$

$$\Delta J_1 \approx 10 \text{ to } 20 \tag{5.34}$$

where

ΔJ_{ave} : Change in average cost function

ΔJ_1 : Change in cost function of individual frequency response pair

A parameter is eliminated in identification model structure by taking that parameter constant in identification model (fixed). If this constant is taken zero, then the dynamic effect is also removed. However, if the parameter is estimated or known somehow and a reasonable value is assigned, then the parameter is removed only identification model, but its effect on dynamic model exists.

2) Correlation is eliminated:

The parameters used in identification model have acceptable sensitivity after first step is completed. In this step, Cramér-Rao (CR) values of parameters are concerned. High value CR of a parameter shows that this parameter is correlated with other parameter(s). Therefore, to identify the correlation, confidence ellipsoids of parameters with high CR values are used. Generally, the parameters with highest CR, which excess the CR limit (~ 20), are eliminated. However, if the high CR values of parameters are close to each other, then the best way is figuring out the most correlated one by trial and error and then that parameter is eliminated.

The elimination of high CR value parameters is done one by one, for each step the cost functions and CR values are calculated. The important thing when the elimination is applied is that the cost functions are grown at the beginning of the iterations, but the cost function is going to fall after a few iterations since the eliminated parameter with high CR has low insensitivity value. If the highest Cramér-Rao value of parameter is close to the given limit, then decision of removing the parameter is given according to increase in cost function. If the change in the cost function is smaller than the limits in Eqns. (5.33) and (5.34) then the parameter are not removed.

5.4 State-Space Identification

The equations of motion are cast in state space form as:

$$\begin{aligned} \boldsymbol{M}\dot{\boldsymbol{x}} &= \boldsymbol{F}\boldsymbol{x} + \boldsymbol{G}\boldsymbol{u}(t-\boldsymbol{\tau}) \\ \boldsymbol{y} &= \boldsymbol{H_0}\boldsymbol{x} + \boldsymbol{H_1}\dot{\boldsymbol{x}} \end{aligned} \tag{5.35}$$

where

$$\boldsymbol{x} = \begin{bmatrix} u \\ v \\ w \\ p \\ q \\ r \\ \phi \\ \theta \end{bmatrix} \qquad \boldsymbol{u} = \begin{bmatrix} \delta_a \\ \delta_e \\ \delta_r \\ \delta_t \end{bmatrix} \qquad \boldsymbol{y} = \begin{bmatrix} u \\ v \\ w \\ p \\ q \\ r \\ a_x \\ a_y \\ a_z \end{bmatrix} \tag{5.36}$$

By using equations of motion and it is assumed that the fixed-wing aircraft has planar symmetry and longitudinal and lateral/directional DoF are not coupled; the longitudinal and lat/dir model structures are formed in Sec 5.4.1 and 5.4.2.

5.4.1 Longitudinal Model Structure

The longitudinal states are

$$\boldsymbol{x} = \begin{bmatrix} u \\ w \\ q \\ \theta \end{bmatrix} \tag{5.37}$$

The measurements are

$$\boldsymbol{y} = \begin{bmatrix} \alpha \\ q \\ a_x \\ a_z \end{bmatrix} \tag{5.38}$$

The inputs are

$$\boldsymbol{u} = \begin{bmatrix} \delta_e \\ \delta_t \end{bmatrix} \tag{5.39}$$

With the assumptions of a rigid body vehicle, inertial and aerodynamic symmetry, no coupling between longitudinal and lateral-directional DoF, the Equations of Motion are given as:

$$\dot{u} = -W_0 q - (g cos\Theta_0)\theta + X_u u + X_w w + X_q q + X_{\delta_e}\delta_e + X_{\delta_t}\delta_t \tag{5.40}$$

$$\dot{w} = +U_0 q - (g sin\Theta_0)\theta + Z_u u + Z_w w + Z_q q + Z_{\delta_e}\delta_e + Z_{\delta_t}\delta_t \tag{5.41}$$

$$\dot{q} = M_u u + M_w w + M_q q + M_{\delta_e}\delta_e + M_{\delta_t}\delta_t \tag{5.42}$$

$$\dot{\theta} = q \tag{5.43}$$

The measurement relations are given as:

$$\alpha = \frac{w}{U_0} \tag{5.44}$$

$$q = q \tag{5.45}$$

$$a_x = \dot{u} + W_0 q + (g cos\Theta_0)\theta \tag{5.46}$$

$$a_z = \dot{w} - U_0 q + (g sin\Theta_0)\theta \tag{5.47}$$

By using the above equations the M, F, G, H_0, H_1 matrices are written as:

Table 5.1 Longitudinal State Space Model Structure Arrays

M Matrix

	u	w	q	θ
u	1	0	0	0
w	0	1	0	0
q	0	0	1	0
θ	0	0	0	1

F Matrix

	u	w	q	θ
u	X_u	X_w	X_q-W_0	-(gcosΘ$_0$)
w	Z_u	Z_w	Z_q+U_0	-(gsinΘ$_0$)
q	M_u	M_w	M_q	0
θ	0	0	1	0

G Matrix

	δ_e	δ_t
u	$X_{\delta e}$	$X_{\delta t}$
w	$Z_{\delta e}$	$Z_{\delta t}$
q	$M_{\delta e}$	$M_{\delta t}$
θ	0	0

H0 Matrix

	u	w	q	θ
α	0	1/U_0	0	0
q	0	0	1	0
a_x	0	0	W_0	(gcosΘ$_0$)
a_z	0	0	-U_0	(gsinΘ$_0$)

H1 Matrix

	u	w	q	θ
α	0	0	0	0
q	0	0	0	0
a_x	1	0	0	0
a_z	0	1	0	0

In the flight test, trim condition of the frequency sweep applied is

$$(V_{tot})_0 = 35.8\ m/s \qquad U_0 = 35.4\ m/s$$

$$\Theta_0 = -0.8\ deg \qquad W_0 = -0.2\ m/s$$

The start and end frequencies of the frequency pairs used in system identification are determined according to their coherence values. The frequency range where frequency response pair has greater than coherence value, 0.6, is selected for the identification process. When the flight test data is examined, it is seen that throttle sweeps are not suitable for the identification process, since all the coherence values are smaller than 0.6.

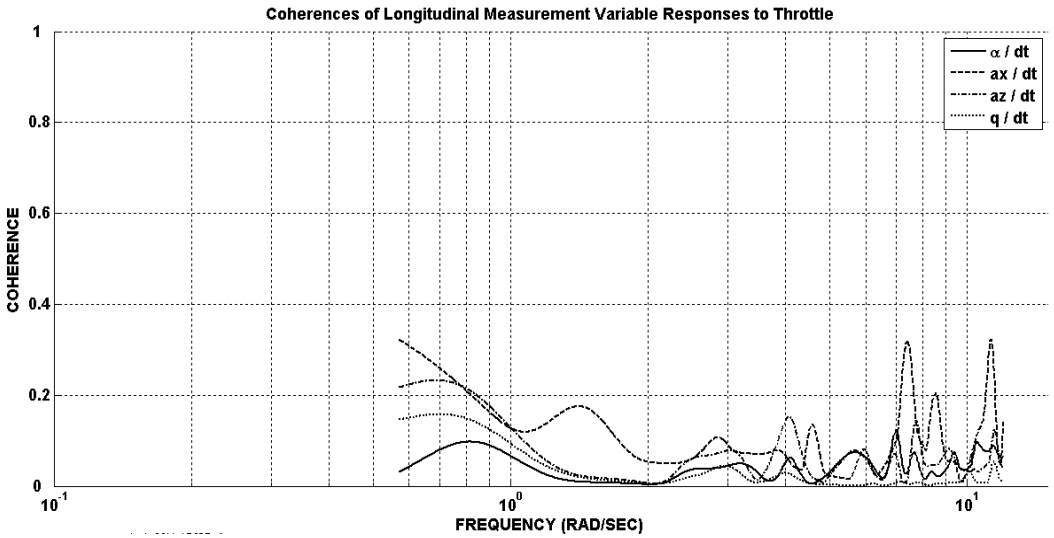

Figure 5.1 Coherence Values of Responses of Longitudinal Variables to Throttle Input

Since the throttle inputs are not suitable for identification, the identification of longitudinal state space model is done by using elevator input only. Therefore, δ_t term in Eqn. (5.39) is dropped. For elevator sweep, the coherence values input-output pairs are given in Figure 5.2.

From Figure 5.2, it is seen that the frequency responses have information at frequency ranges that start at 0.8 rad/s. When the phugoid mode is concerned, it is known that this mode is valid at low frequencies, below 0.8 rad/s as it is shown in Figure 5.3. Therefore, it is stated that with these flight test data, the identification of phugoid mode is not possible. As a result, it is decided that the longitudinal model of the UAV includes only short period mode and its A matrix has 3x3 matrix form. Therefore, u term in Eqn. (5.37) and $a_x$term in Eqn. (5.38) are dropped from the model structure

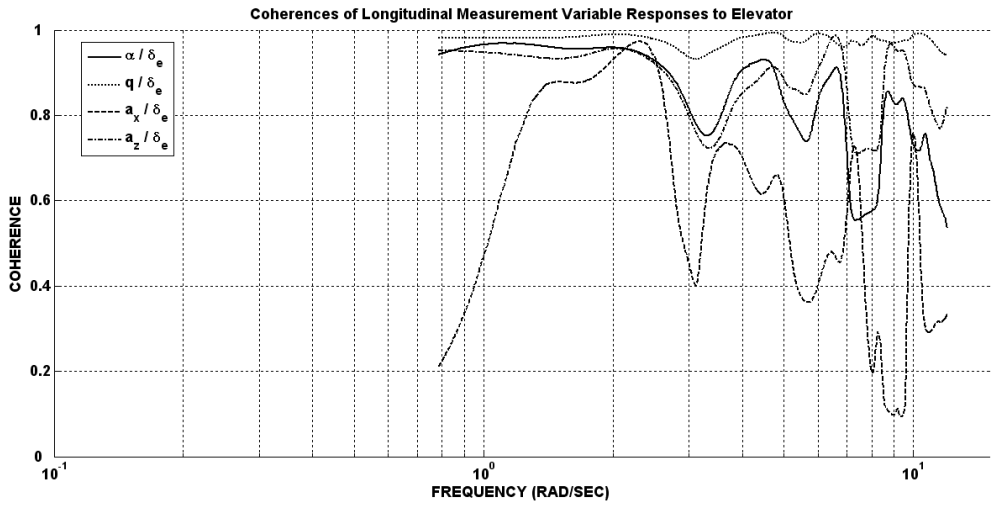

Figure 5.2 Coherence Values of Responses of Longitudinal Variables to Elevator Input

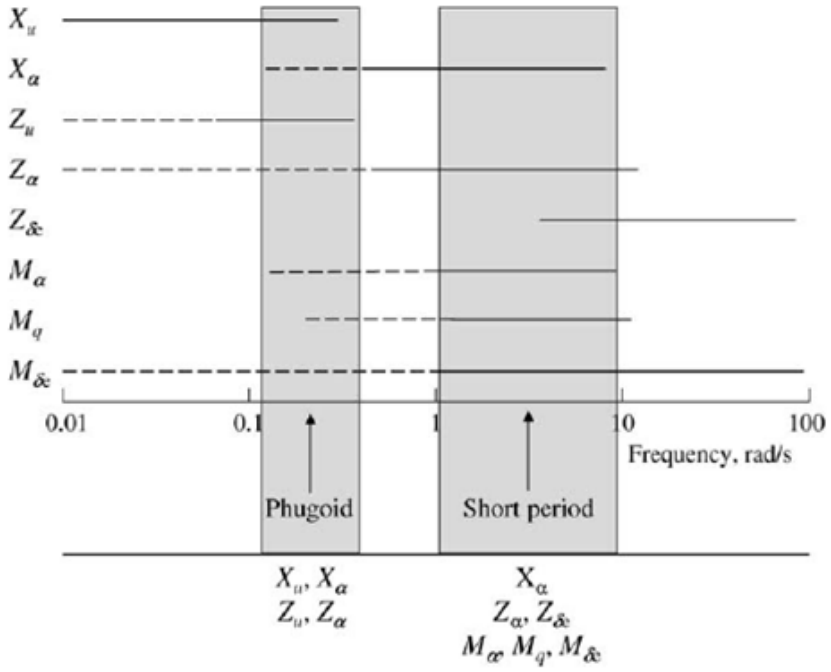

Figure 5.3 Regions of Identifiability for Longitudinal Parameters [10]

The model structure given in Table 5.1 is updated according to discussions about longitudinal model of the UAV, and then the updated model structure is given in Table 5.2.

Table 5.2 Modified Longitudinal State Space Model Structure Arrays

M Matrix

	w	q	θ
w	1	0	0
q	0	1	0
θ	0	0	1

F Matrix

	w	q	θ
w	Z_w	Z_q+U_0	$-(g\sin\Theta_0)$
q	M_w	M_q	0
θ	0	1	0

G Matrix

	δ_e
w	$Z_{\delta e}$
q	$M_{\delta e}$
θ	0

H0 Matrix

	w	q	θ
α	$1/U_0$	0	0
q	0	1	0
a_z	0	$-U_0$	$(g\sin\Theta_0)$

H1 Matrix

	w	q	θ
α	0	0	0
q	0	0	0
a_z	1	0	0

The initial guesses for the identification parameters are obtained from the linearized output of the Pelikan simulation model, which is determined using numerical perturbations. Then, MIMO (Multi-input/Multi-output) state space system identification is obtained by using DERIVID toolbox of CIFER®. The models of systems which can be Linear-Time-Invariant (LTI) differential equations are formed with up to 40 states and 100 unknown parameters. To identify the parameters, DERIVID uses an iterative, robust secant search algorithm by aiming to obtain minimum error between state space model and frequency response of flight test data. By using DERIVID, initial identification results are obtained as in Table 5.3 with average cost of 39.2:

Table 5.3 Longitudinal State Space Identification Result – Step 1

Parameter	*Value*	*CR Bound*	*CR %*	*Insensitivity %*
Zw	-2,816	0,187	6,64	1,63
Zq	-3,117	1,812	58,14	13,01
Mw	-0,058	0,014	25,06	5,00
Mq	-1,888	0,231	12,21	1,636
Zde	4,645	2,712	58,39	17,01
Mde	-9,091	0,395	4,35	0,89

COST FUNCTIONS	
α / δe	25,0
q / δe	54,7
az / δe	28,5
w / δe	48,4
Average	39,2

When the results are examined, it is noticed that $Z_{\delta e}$ has the highest insensitivity value. Therefore, this parameter is eliminated from state space model by fixing it a constant. After that, the identification is renewed using remaining parameters. The new results are given in Table 5.4:

Table 5.4 Longitudinal State Space Identification Result – Step 2

Parameter	*Value*	*CR Bound*	*CR %*	*Insensitivity %*
Zw	-2,593	0,138	5,32	1,71
Zq	0,797	1,281	160,80	50,23
Mw	-0,063	0,013	20,75	4,54
Mq	-1,834	0,213	11,63	1,71
Zde	0	-	-	-
Mde	-8,978	0,367	4,09	0,91

COST FUNCTIONS		*Delta*	*Limit*
α / δe	25,7	0,7	<10
q / δe	55,4	0,7	<10
az / δe	22,1	-6,4	<10
w / δe	59,4	11,0	<10
Average	40,7	1,5	<1-2

In Table 5.4, the Delta column shows the change in the cost functions values. The limit values are taken in Eqn. (5.33) and (5.34). If the changes in the cost functions are in the limits, it is shown that the model reduction is successful. As seen in Table 5.4, dropping $Z_{\delta e}$ term from model structure is successfully done. In step 2, Z_q term has insensitivity value greater than limit, therefore it is fixed and the identification is renewed. The updated results are given in Table 5.5.

In Table 5.5, it is seen that the change in the cost functions are in the limit; therefore, Z_q term is successfully dropped from the model structure. In this step it is also seen that the both insensitivities and Cramer-Rao bounds of the remaining parameters are in the limit. However, the Cramer-Rao bound of M_w term is very close to the limit, which is 20. Therefore, to see the effect of dropping this term in model structure, it is fixed in Step 4.

Table 5.5 Longitudinal State Space Identification Result – Step 3

Parameter	*Value*	*CR Bound*	*CR %*	*Insensitivity %*
Zw	-2,537	0,102	4,02	1,72
Zq	0	-	-	-
Mw	-0,064	0,013	19,90	4,51
Mq	-1,845	0,21	11,37	1,7
Zde	0	-	-	-
Mde	-9,067	0,345	3,81	0,91
COST FUNCTIONS		***Delta***	***Limit***	
α / δe	26,8	1,1	<10	
q / δe	54,9	-0,5	<10	
az / δe	23,6	1,5	<10	
w / δe	58,2	-1,2	<10	
Average	40,8	0,1	<1-2	

Table 5.6 Longitudinal State Space Identification Result – Step 4

Parameter	*Value*	*CR Bound*	*CR %*	*Insensitivity %*
Zw	-3,029	0,123	4,08	1,89
Zq	0	-	-	-
Mw	0	-	-	-
Mq	-2,214	0,458	12,51	2,43
Zde	0	-	-	-
Mde	-7,155	0,1755	2,453	1,108
COST FUNCTIONS		***Delta***	***Limit***	
α / δe	36,7	36,7	<10	
q / δe	74,4	81,6	<10	
az / δe	37,6	37,6	<10	
w / δe	54,3	17,6	<10	
Average	50,7	-23,7	<1-2	

It is seen that dropping M_w term adversely affect the model structure since the change in the cost functions are beyond the limits. Therefore the model structure in Table 5.5 is selected as final model structure of longitudinal state space model of the UAV.

After the model structure is determined, it is tried to obtained 4x4 matrix, which includes the phugoid mode. Therefore, the model structure is extended to the model in Table 5.1. However, the model structure in Table 5.1 is not applied exactly, the throttle term in G matrix are dropped, the identified parameters in Table 5.5 are fixed and the dropped parameters Table 5.5 do not take place in this model structure. Then, the identification parameters are assigned as X_u, X_w, X_q, $X_{\delta e}$, Z_u and M_u. Then, the modified model structure is given in Table 5.7. By using DERIVID, the parameters and cost function are calculated in Table 5.8.

Table 5.7 Longitudinal State Space Model Structure Arrays to Identify Phugoid Mode

M Matrix

	u	w	q	θ
u	1	0	0	0
w	0	1	0	0
q	0	0	1	0
θ	0	0	0	1

F Matrix

	u	w	q	θ
u	X_u	X_w	X_q-W_0	-(gcosΘ_0)
w	Z_u	-2,537	U_0	-(gsinΘ_0)
q	M_u	-0,064	-1,845	0
θ	0	0	1	0

G Matrix

	δ_e
u	$X_{\delta e}$
w	0
q	-9,067
θ	0

H0 Matrix

	u	w	q	θ
u	1	0	0	0
α	0	1/U_0	0	0
q	0	0	1	0
a_z	0	0	-U_0	(gsinΘ_0)

H1 Matrix

	u	w	q	θ
u	0	0	0	0
α	0	0	0	0
q	0	0	0	0
a_z	0	1	0	0

Table 5.8 Longitudinal State Space Identification Result – Step 5

Parameter	*Value*	*CR Bound*	*CR %*	*Insensitivity %*
Xu	0,359	0,078	21,72	5,75
Xw	0,705	0,094	13,40	1,11
Xq	2,934	1,645	56,06	2,89
Zu	-0,316	0,212	67,14	25,77
Mu	0,053	0,010	19,83	7,08
Xde	13,840	3,011	21,76	1,85

COST FUNCTIONS	
u / δe	2560,7
α / δe	19,5
q / δe	62,7
az / δe	28,3
Average	921,4

As specified in Eqn. (5.27), the cost function must be below than 100 to represent the dynamics of the aircraft. Therefore, it is seen in Table 5.8 that the identified model of speed response to elevator input is unrealistic. As discussed in this section, to identify the phugoid mode and its parameters, data must have information at frequency range of 0.1 rad/s and 0.6 rad/s [10]. As seen in Table 5.8, it is not possible to identify the phugoid mode.

5.4.2 Lateral/Directional Model Structure

The lateral/directional states are

$$\boldsymbol{x} = \begin{bmatrix} v \\ p \\ r \\ \phi \end{bmatrix} \tag{5.48}$$

The measurements are

$$\boldsymbol{y} = \begin{bmatrix} p \\ r \\ a_y \\ \beta \end{bmatrix} \tag{5.49}$$

The inputs are

$$\boldsymbol{u} = \begin{bmatrix} \delta_a \\ \delta_r \end{bmatrix} \tag{5.50}$$

Using the assumptions of a rigid body vehicle, inertial and aerodynamic symmetry, no coupling between longitudinal and lateral-directional DoF, the Equations of Motion are obtained as:

$$\dot{v} = -U_0 r + W_0 p + (g cos\Theta_0)\phi + Y_v v + Y_p p + Y_r r + Y_{\delta_a}\delta_a + Y_{\delta_r}\delta_r \tag{5.51}$$

$$\dot{p} = L'_v v + L'_p p + L'_r r + L'_{\delta_a}\delta_a + L'_{\delta_r}\delta_r \tag{5.52}$$

$$\dot{r} = N'_v v + N'_p p + N'_r r + N'_{\delta_a}\delta_a + N'_{\delta_r}\delta_r \tag{5.53}$$

$$\dot{\phi} = p + r tan\Theta_0 \tag{5.54}$$

where L_i' and N_i' are defined as [18]

$$L_i' = \frac{L_i + (I_{xz}/I_{xx})N_i}{1 - [I_{xz}^2/(I_{xx}I_{zz})]} \tag{5.55}$$

$$N_i' = \frac{N_i + (I_{xz}/I_{zz})L_i}{1 - [I_{xz}^2/(I_{xx}I_{zz})]} \tag{5.56}$$

The measurement relations are

$$p = p \tag{5.57}$$

$$r = r \tag{5.58}$$

$$a_y = \dot{v} + U_0 r - W_0 p - (g cos\Theta_0)\phi \tag{5.59}$$

$$\beta = \frac{v}{(V_{tot})_0} \tag{5.60}$$

By using the above equations the M, F, G, H_0, H_1 matrices are written as:

Table 5.9 Lateral-Directional State Space Model Structure Arrays

M Matrix

	v	ϕ	p	r
v	1	0	0	0
ϕ	0	1	0	0
p	0	0	1	0
r	0	0	0	1

F Matrix

	v	ϕ	p	r
v	Y_v	$g\cos\Theta_0$	Y_p	Y_r-U_0
ϕ	0	0	1	$\tan\Theta_0$
p	L_v'	0	L_p'	L_r'
r	N_v'	0	N_p'	N_r'

G Matrix

	δ_a	δ_r
v	$Y_{\delta a}$	$Y_{\delta r}$
ϕ	0	0
p	$L_{\delta a}'$	$L_{\delta r}'$
r	$N_{\delta a}'$	$N_{\delta r}'$

H0 Matrix

	v	ϕ	p	r
p	0	0	1	0
r	0	0	0	1
a_y	0	-($g\cos\Theta_0$)	-W_0	U_0
β	$1/(V_{tot})_0$	0	0	0

H1 Matrix

	v	ϕ	p	r
p	0	0	0	0
r	0	0	0	0
a_y	1	0	0	0
β	0	0	0	0

In the flight test, trim condition of the frequency sweep applied is

$$(V_{tot})_0 = 38\ m/s \qquad U_0 = 37.9\ m/s$$

$$\Theta_0 = 3\ deg \qquad W_0 = 0.5\ m/s$$

The start and end frequencies of the frequency pairs used in system identification are determined according to their coherence values. The frequency range where frequency response pair has greater than coherence value, 0.6, is selected for the identification process. When the flight test data is examined, the following frequency ranges for pairs are decided to use.

Table 5.10 Frequency Range of Interests of Frequency Response Pairs

	Frequency of Interests	
	δ_a	δ_r
p	***0.7 - 12*** rad/s	***1 - 3*** rad/s
r	***0.7 - 12*** rad/s	***0.7 - 12*** rad/s
a_y	***0.7 - 3*** rad/s	***0.7 - 8*** rad/s
β	***0.7 - 3*** rad/s	***0.7 - 7*** rad/s

By using DERIVID, initial identification results are obtained as in Table 5.11 with average cost of 68.98.

When the results are examined, it is noticed that Y_r has the highest insensitivity value. Therefore, this parameter is eliminated from state space model by taking it constant. After that, the identification is renewed using remaining parameters. The new results are given in Table 5.12:

Table 5.11 Lateral/Directional State Space Identification Result – Step 1

Parameter	*Value*	*CR Bound*	*CR %*	*Insensitivity %*
Yv	-0.3453	0.01378	3.99	1.395
Yp	0.7198	0.3597	49.98	5.112
Yr	0.1331	0.2545	191.2	57.17
Lv	-0.07523	0.02016	26.8	3.898
Lp	-5.536	0.3853	6.96	1.104
Lr	1.908	0.2271	11.9	3.253
Nv	0.2646	5.86E-03	2.214	0.694
Np	-0.961	0.07431	7.732	1.493
Nr	-1.287	0.07218	5.607	2.096
Yda	2.699	1.305	48.35	4.569
Ydr	2.315	0.4237	18.31	7.65
Lda	-20.82	1.287	6.184	0.9902
Ldr	-0.3195	0.8461	264.8	32.35
Nda	-0.265	0.1951	73.63	16.34
Ndr	-8.596	0.2833	3.296	0.9483

$$J_{ave} = 68.98$$

Table 5.12 Lateral/Directional State Space Identification Result – Step 2

Parameter	*Value*	*CR Bound*	*CR %*	*Insensitivity %*
Yv	-0.344	0.01356	3.942	1.406
Yp	0.8356	0.2828	33.84	4.418
Yr	0	0	-	-
Lv	-0.07489	0.02005	26.77	3.918
Lp	-5.525	0.384	6.95	1.112
Lr	1.913	0.2271	11.87	3.249
Nv	0.2645	5.85E-03	2.212	0.6942
Np	-0.9606	7.44E-02	7.744	1.496
Nr	-1.284	0.07165	5.581	2.1
Yda	3.176	0.9152	28.81	3.892
Ydr	2.23	0.3987	17.87	7.928
Lda	-20.77	1.282	6.17	0.9978
Ldr	-0.3278	0.8402	256.3	31.47
Nda	-0.2643	0.1956	74.01	16.39
Ndr	-8.581	0.2822	3.289	0.9501

$$J_{ave} = 69.04$$

As seen in the table, the highest sensitivity value belongs to L_{dr} parameter, and that value is higher than the sensitivity limit. Therefore, this parameter is eliminated from identification model. After that, the identification is renewed using remaining parameters. The results are given in Table 5.13.

Table 5.13 Lateral/Directional State Space Identification Result – Step 3

Parameter	*Value*	*CR Bound*	*CR %*	*Insensitivity %*
Yv	-0.3434	0.01345	3.915	1.408
Yp	0.839	0.2822	33.64	4.411
Yr	0	0	-	-
Lv	-0.08241	8.81E-03	10.68	3.568
Lp	-5.501	0.3714	6.751	1.119
Lr	1.98	0.1585	8.007	3.166
Nv	0.2637	5.61E-03	2.127	0.6922
Np	-0.961	7.40E-02	7.703	1.501
Nr	-1.286	0.07126	5.541	2.093
Yda	3.186	0.9134	28.67	3.878
Ydr	2.194	0.388	17.68	8.055
Lda	-20.77	1.279	6.157	0.9984
Ldr	0	0	-	-
Nda	-0.2633	0.195	74.05	16.5
Ndr	-8.545	0.2681	3.137	0.944

$$J_{ave} = 69.08$$

When the results in Table 5.13 are examined, it is seen that all the insensitivity values are in the limit; therefore the second step in model reduction is applied. In that step, Cramér-Rao values are checked to determine any correlation between parameters in the identification model structure. The highest CR value is seen at N_{da} parameter. Since CR value is higher than the defined limit, this parameter is dropped from the model structure. After that, the renewed results are given in Table 5.14.

Table 5.14 Lateral/Directional State Space Identification Result – Step 4

Parameter	*Value*	*CR Bound*	*CR %*	*Insensitivity %*
Yv	-0.3442	0.01351	3.924	1.403
Yp	0.7877	0.2705	34.34	4.665
Yr	0	0	-	-
Lv	-0.07833	7.94E-03	10.14	3.614
Lp	-5.264	0.3182	6.045	1.158
Lr	1.934	0.1506	7.785	3.133
Nv	0.2654	5.49E-03	2.068	0.6883
Np	-0.8938	5.25E-02	5.875	1.61
Nr	-1.297	0.07056	5.441	2.073
Yda	2.991	0.8787	29.38	4.141
Ydr	2.188	0.3871	17.69	8.059
Lda	-20.13	1.15	5.711	1.031
Ldr	0	0	-	-
Nda	0	0	-	-
Ndr	-8.551	0.268	3.134	0.9439

$$J_{ave} = 69.58$$

When the results are examined, all the parameters have acceptable CR and insensitivity values. Moreover, dropping N_{da} parameter causes less than 1 change in cost function, this shows that although dropping N_{da} parameter affects the cost function, change in cost function is in limit due to its sensitivity value; therefore, it is correct to eliminate N_{da}.

5.5 Verification

After the identification is accomplished, to represent the model fidelity, robustness and limitation in linear model, time domain verification is applied to the identification result. Time domain verification is based on the direct integration of the equations of motion. In verification step, the identified parameters obtained by frequency domain system identification are kept fixed.

It is known that in state space representation, the control inputs and reference outputs are the perturbation values from trim conditions. The trim values are taken from trim duration at beginning of the frequency sweep or other test inputs. However, obtaining a steady-state condition in trim duration is difficult due to turbulence and other disturbances. Therefore, for control inputs, residual errors in the estimate of the reference control are included as an unknown acceleration bias vector [10]:

$$\boldsymbol{M}\dot{\boldsymbol{x}} = \boldsymbol{F}\boldsymbol{x} + \boldsymbol{G}\boldsymbol{u}(t - \boldsymbol{\tau}) + \dot{x}_b \tag{5.61}$$

This constant bias term also provides a first-order correction for the effects of process noise such as turbulence, unmeasured secondary controls, and numerical integration errors. For reference output, residual errors in output estimate are included as a constant reference shift vector [10]:

$$\boldsymbol{y} = \boldsymbol{H_0}\boldsymbol{x} + \boldsymbol{H_1}\dot{\boldsymbol{x}} + \boldsymbol{y_{ref}} \tag{5.62}$$

This constant reference shift term also provides contributions to measured output due to sensor bias, instrumentation misalignment, etc. These equations are applied in the identification results using the Simulink model given in Figure 5.4:

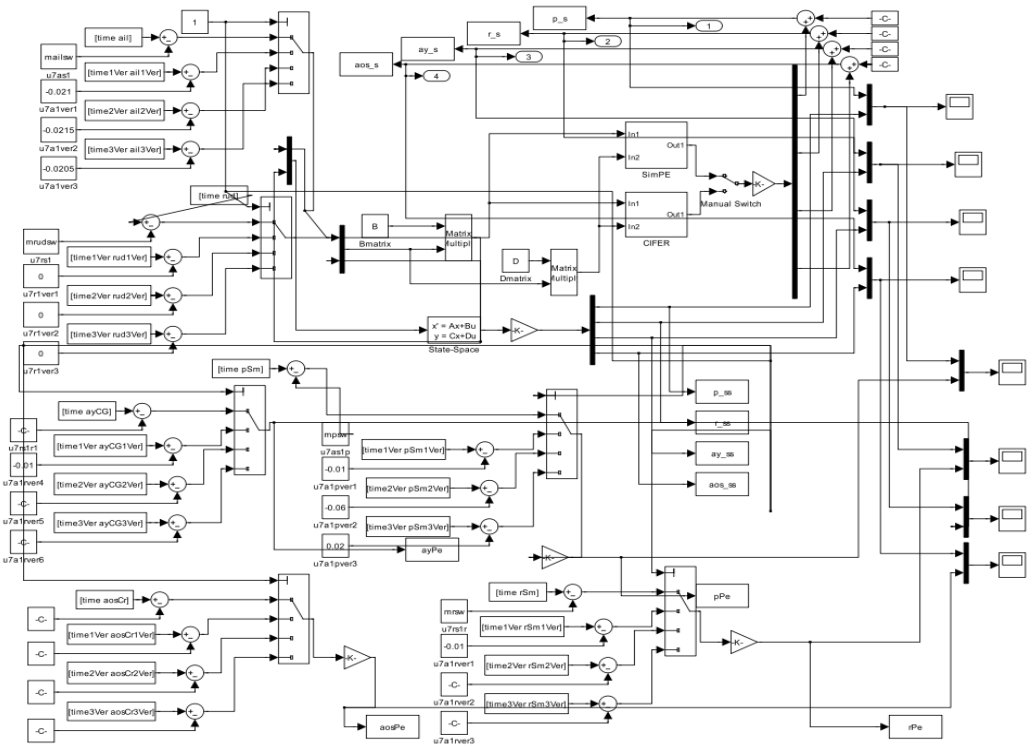

Figure 5.4 Simulink Model for calculating bias and reference shifts

In the graphs, given in this section, legends are given as:

ElvSw : responses to elevator sweep

RudSw : responses to rudder sweep

AilSw : responses to aileron sweep

ElvVer1 and ElvVer2 : responses to elevator verification input

RudVer1 : responses to rudder verification input

AilVer2 : responses to aileron verification input

Id w/o corr : Identification results without bias or reference shift correction

Id w corr : Identification results with bias and reference shift correction

The effect of estimated bias and reference shift on identification results are shown following graphs. In the graphs, the responses of measurement vector elements to elevator input, aileron input and rudder input take place. For longitudinal motion, the graphs are separated two: state space model results to identification input and their time domain comparison with flight test data and state space model results to verification input and their time domain comparison with flight test data. For lateral/directional motion, in the graph set, the first graph is for responses to rudder input, used in identification; the second graph is for responses to aileron input, used in identification; third graph is for response to rudder and aileron input, which are dissimilar then identification inputs. In this study, doublets are used as a dissimilar input.

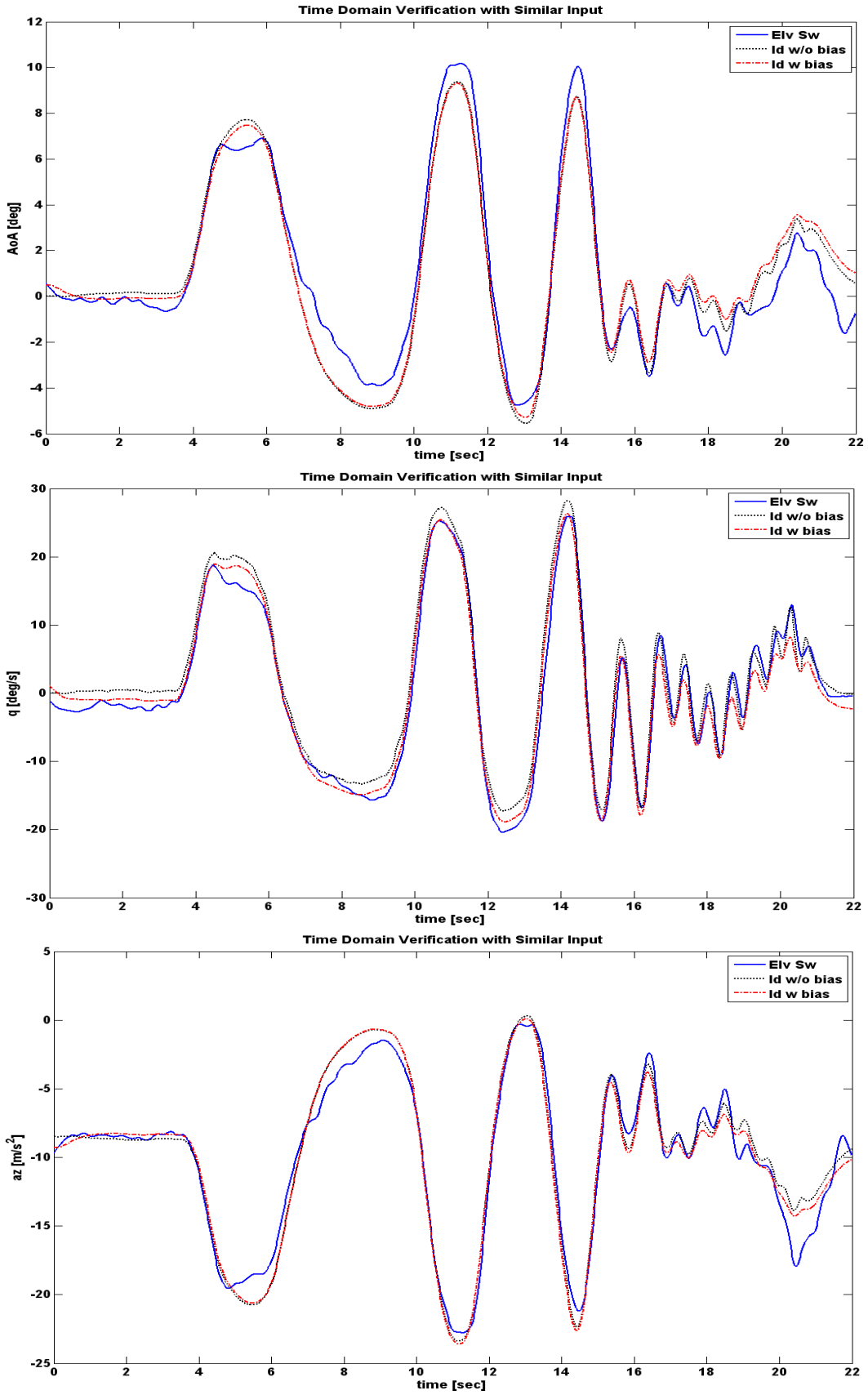

Figure 5.5 Longitudinal SS Model Responses to Elevator Sweep

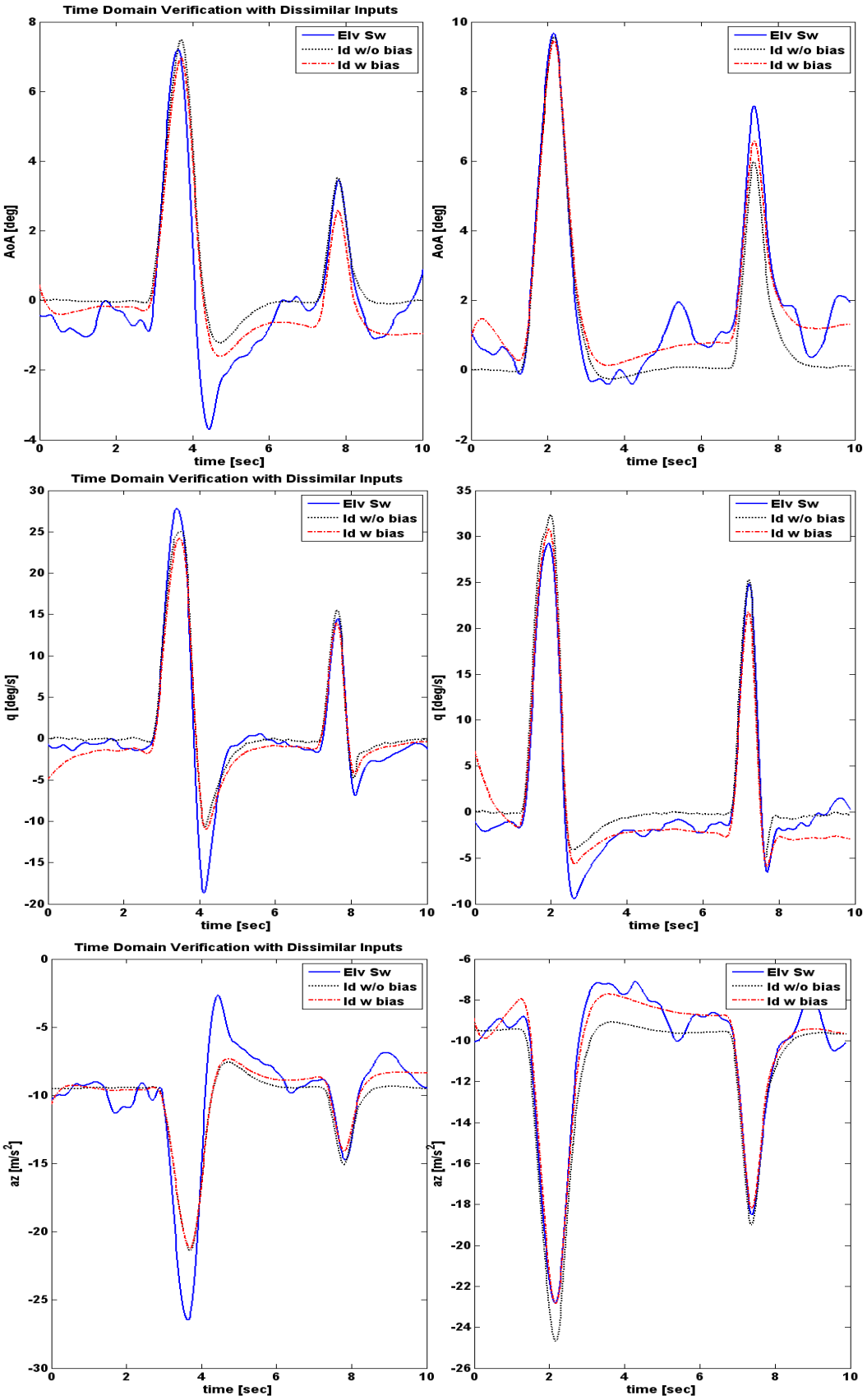

Figure 5.6 Longitudinal SS Model Responses to Verification Inputs

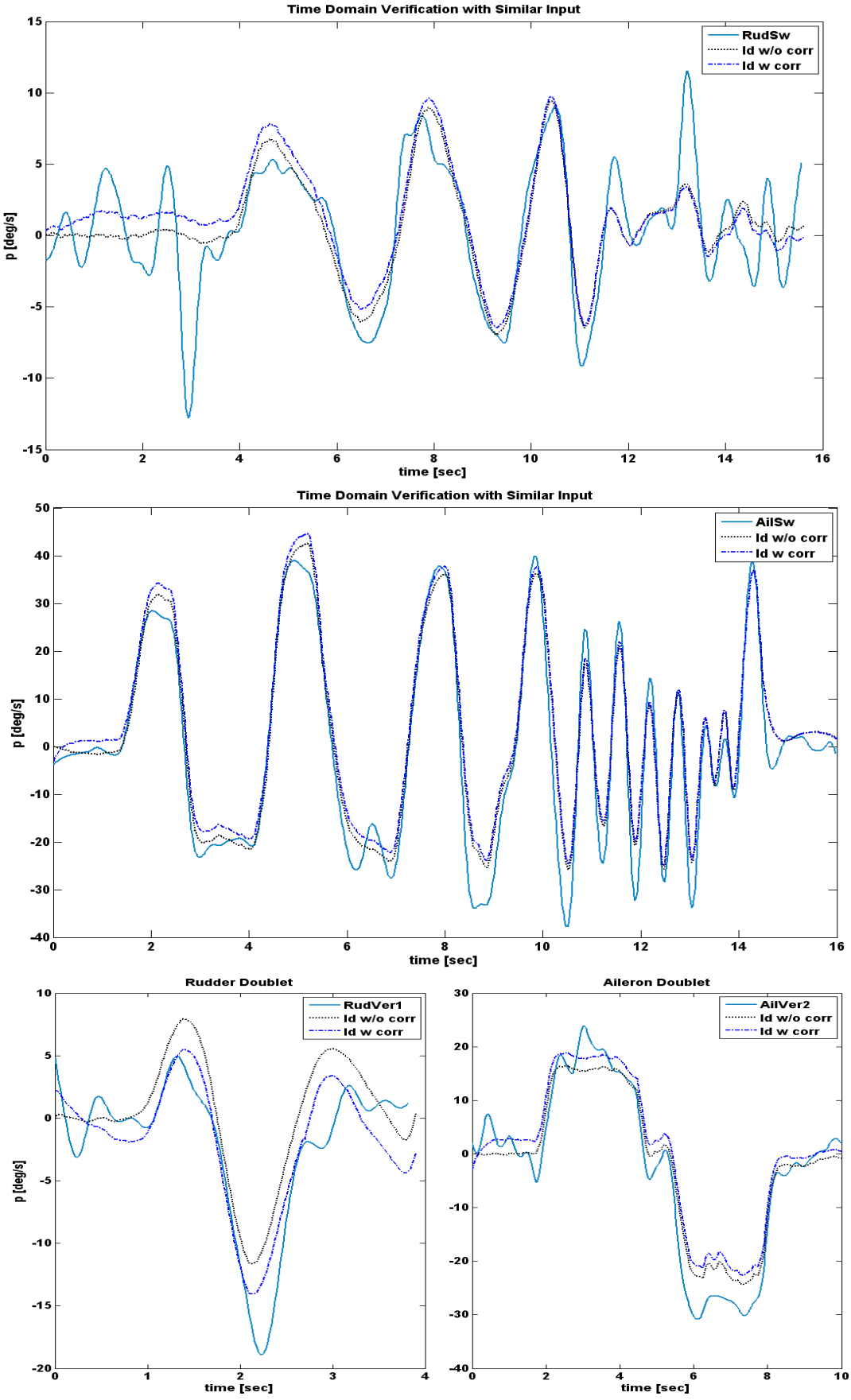

Figure 5.7 Roll Rate Responses to Lateral/Directional Inputs

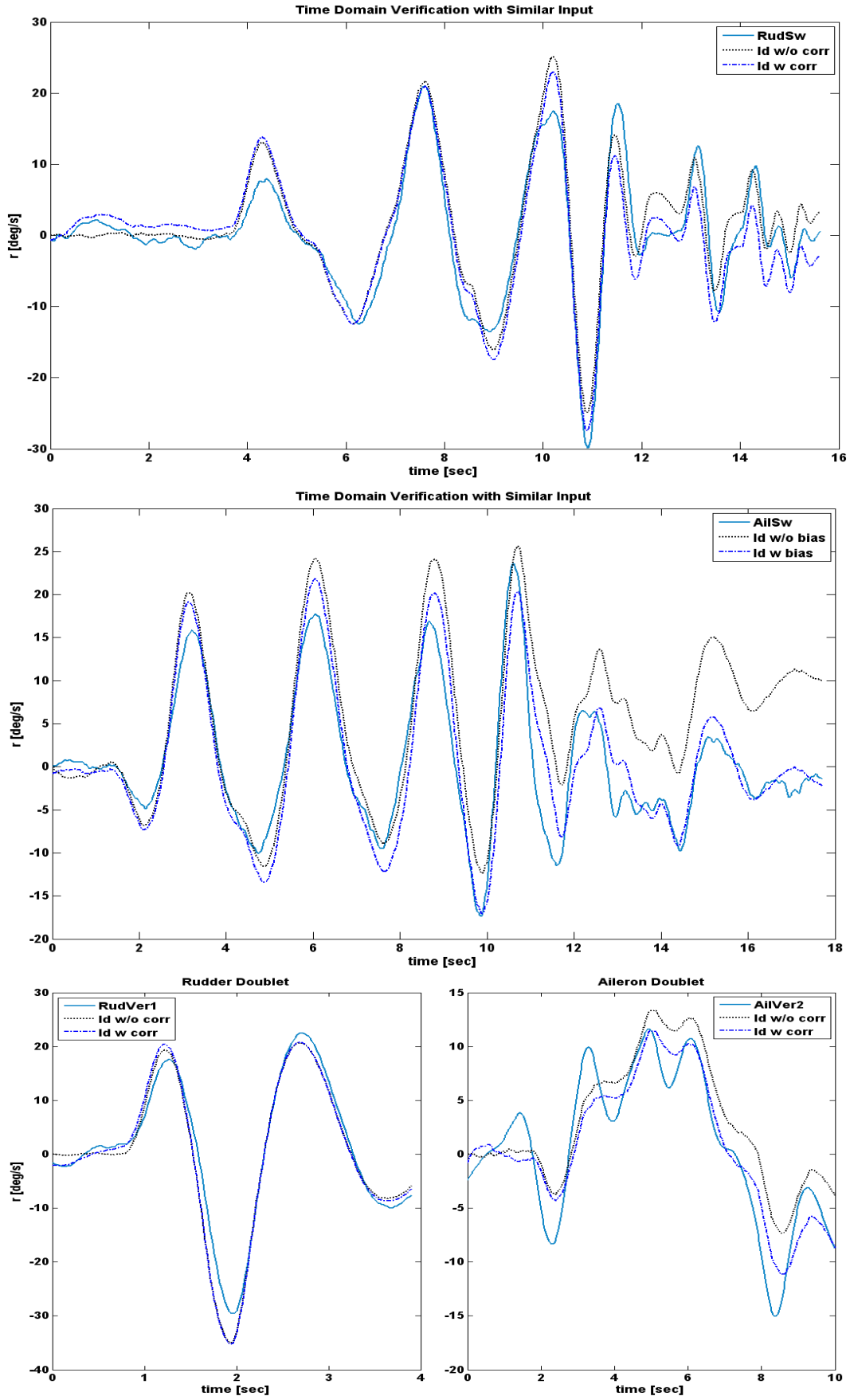

Figure 5.8 Yaw Rate Responses to Lateral/Directional Inputs

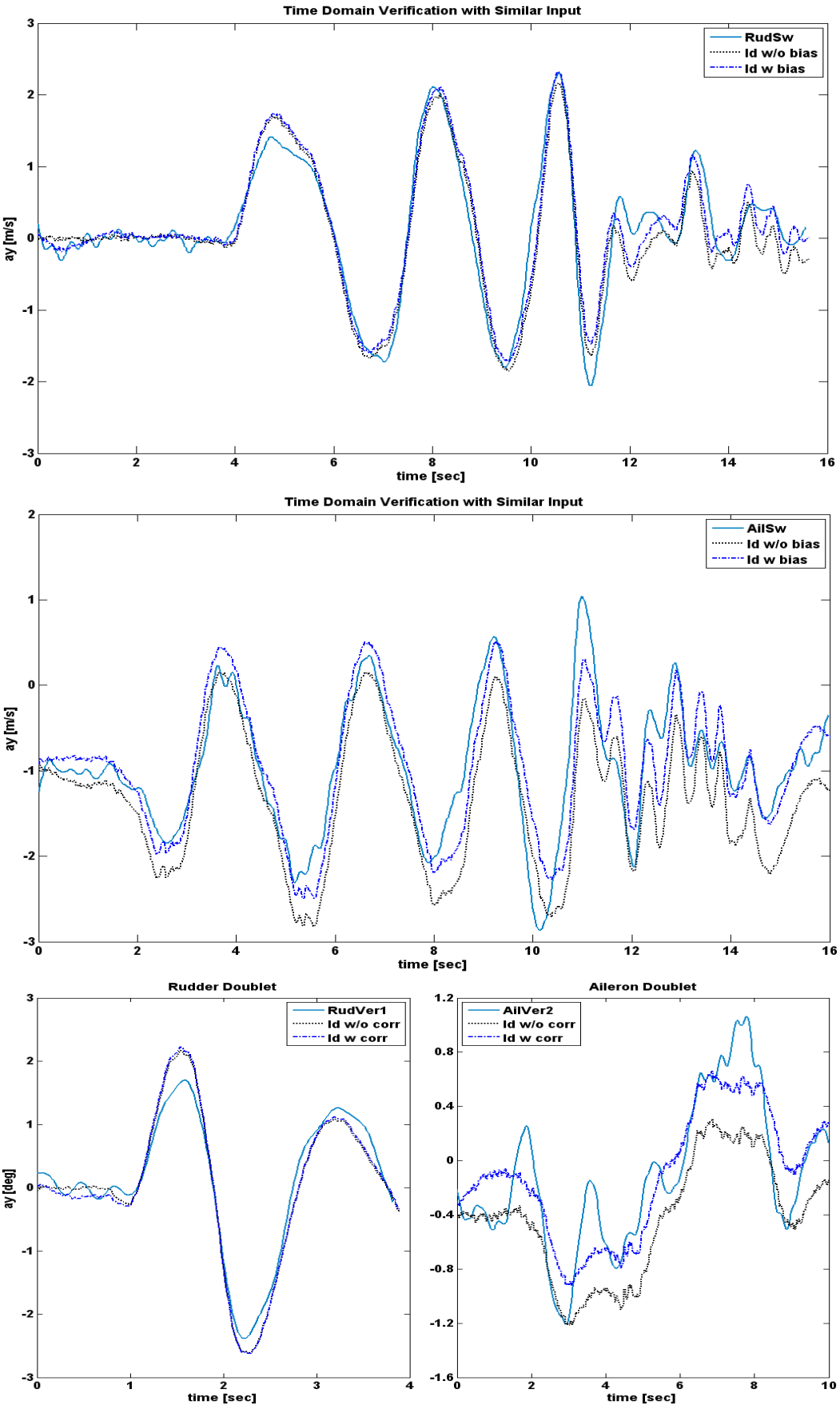

Figure 5.9 Y Acceleration Responses to Lateral/Directional Inputs

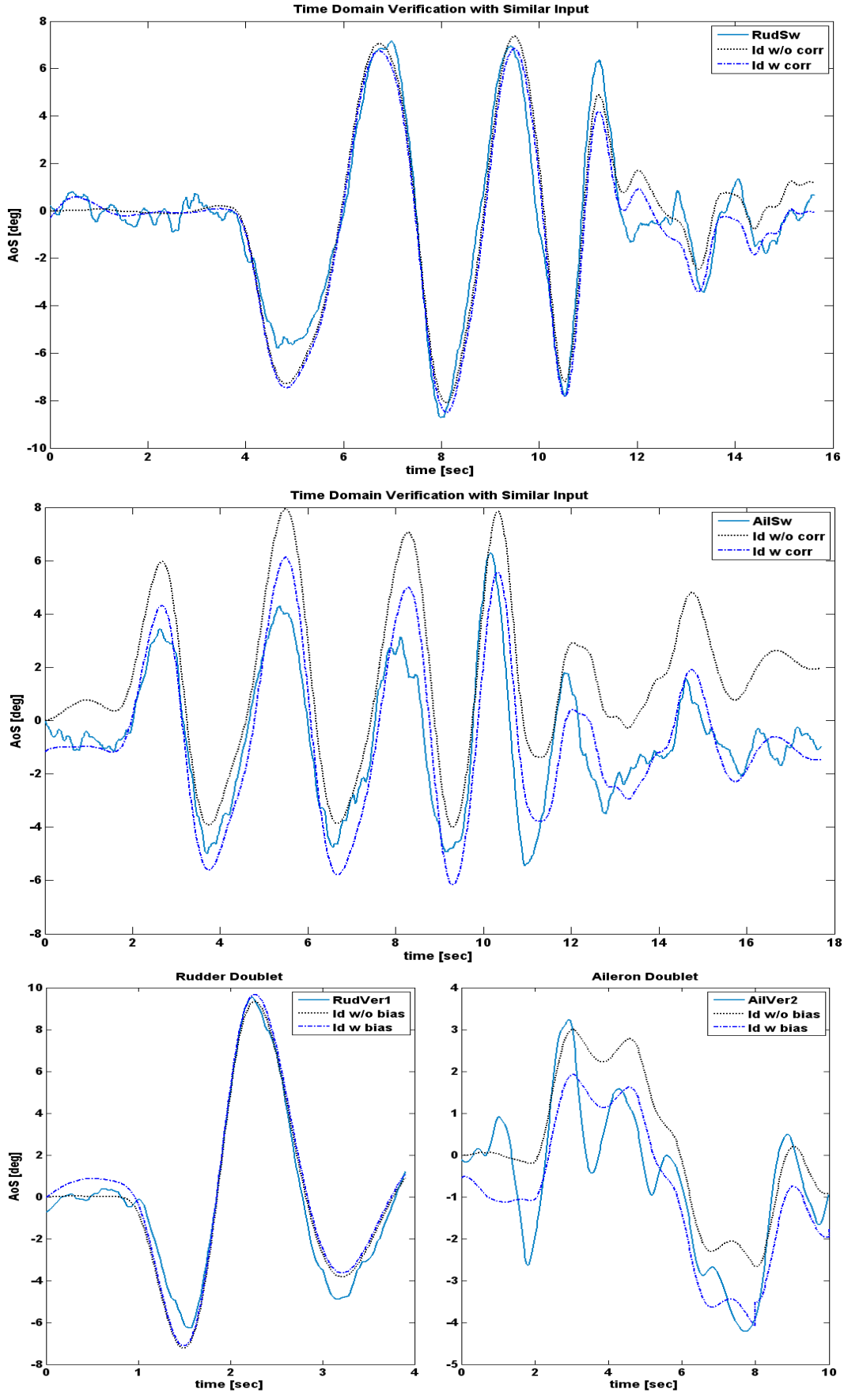

Figure 5.10 Sideslip Angle Responses to Lateral/Directional Inputs

In Figure 5.5 and Figure 5.6, the longitudinal responses of the aircraft (α, q and a_z) and their state space model values are compared. In Figure 5.5, time domain verification of the model responses to identification input is given. The verification done by identification input shows the model accuracy that is high for each response in this case. In Figure 5.6, time domain verification of the model responses to verification input is given. This verification shows the model robustness.

The first graphs in Figure 5.7, Figure 5.8, Figure 5.9 and Figure 5.10 show the flight test data, which are lateral/directional responses of aircraft (p, r, a_y and β) to *rudder* frequency sweep and responses obtained using estimated state space model. The aim of these graphs is to show the time domain verification of the identified model with the identification inputs. It is seen that the match between identified model and aircraft responses are well and this shows that the model is very accurate. In the graphs, the results of the state space identification with bias and/or reference shift correction and without correction are also compared. It is seen that the effect of the correction on the identification results is very important.

The second graphs in Figure 5.7, Figure 5.8, Figure 5.9 and Figure 5.10 show the flight test data, which are lateral/directional responses of aircraft (p, r, a_y and β) to *aileron* frequency sweep and responses obtained using estimated state space model. The aim of these graphs is to show the time domain verification of the identified model with the inputs used in the identification process. It is seen that the match between identified model and aircraft responses are well and this shows that the model is accurate.

The last graphs in Figure 5.7, Figure 5.8, Figure 5.9and Figure 5.10 are time domain verification of identified model with flight test data. The difference with first graphs is that in these graphs, different input types are used since the aim is verifying the robustness of identified model. It is seen that the match between identified model and aircraft response is well and this shows that robustness of the model is verified. Another point deduced from the graphs is that the linear identified model is valid up to high values of responses such as 10° sideslip, 30°/s yaw rate and roll rate although the linear models are recognized as they are valid for a trim condition with small perturbation.

5.6 State Space and Transfer Function Model Comparison

The comparison of the results of the both model is done by the following two methods:

1) By plotting the outputs of the two models to inputs applied in flight test, then comparing these outputs with the flight test data.
2) By comparing the TFs of the both transfer function model and state space model

5.6.1 Comparison of the Graphs of Model Outputs and Flight Test Data

The results of transfer function modeling and state space modeling are compared with flight test data. The graphs of the transfer function model and state space model comparison are prepared by using both identification and verification inputs. When Figure 5.11 and Figure 5.12 are examined, it is seen that the response of the aircraft and the models are close to each other.

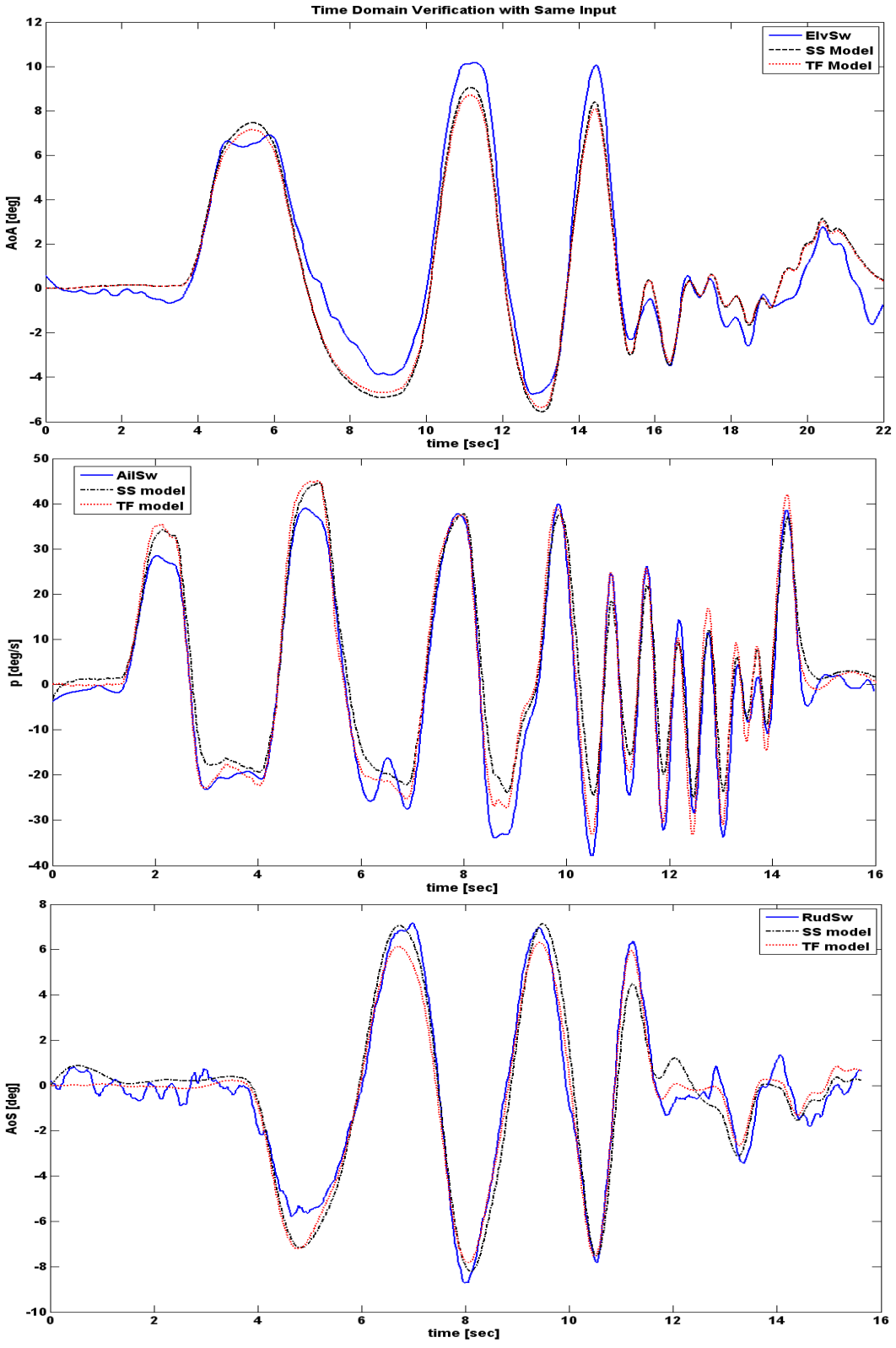

Figure 5.11 Comparison of Results and Flight Data – Responses to Identification Inputs

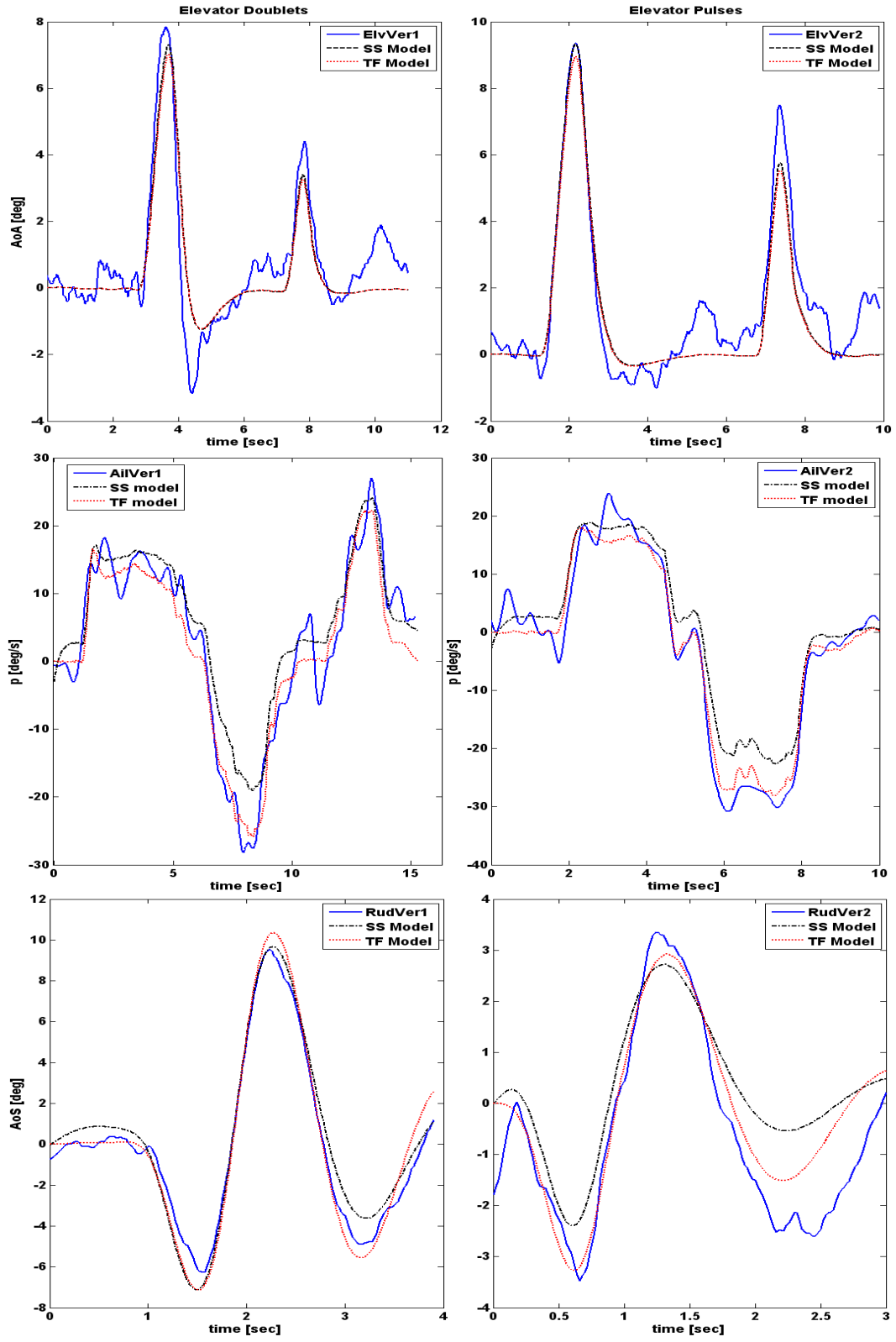

Figure 5.12 Comparison of Results and Flight Data – Responses to Verification Inputs

5.6.2 Comparison of the Transfer Functions of Both Models

To compare the transfer functions; firstly, A matrix of the longitudinal state space model is reduced to 2x2 model, to make state space results comparable with transfer function modeling since in transfer function modeling, only short period mode is identified and short period approximation has 2x2 matrix form [14]. The longitudinal state space model is reduced to 2x2 matrix form by dropping the θ term. Then the transfer function of the reduced longitudinal state space model, which is given in Eqn (5.63).

$$\frac{\alpha}{\delta_e}(s) = \frac{-8.97}{s^2 + 4.42s + 7.01} \tag{5.63}$$

The transfer function modeling of AoA response to elevator input is given as

$$\frac{\alpha}{\delta_e}(s) = \frac{-8.50}{s^2 + 4.35s + 6.96} \tag{5.64}$$

As it is seen in Eqn. (5.63) and (5.64), the state space model and transfer function model has nearly same transfer function. The comparison of the dynamics modes is given in Table 5.15.

The transfer function of state space model of lateral-directional motion is obtained using the MATLAB® command "ss2tf" for roll rate response to the aileron input, the result is given as:

$$\frac{p}{\delta_a}(s) = \frac{-20.151s(s^2 + 1.672s + 10.45)}{(s + 5.081)(s - 0.08033)(s^2 + 1.874s + 11.99)} \tag{5.65}$$

The transfer function of p/δa obtained from transfer function modeling is given in Eqn (4.52). This equation is simplified as zero pole terms in Eqn. (5.66)

$$\frac{p}{\delta_a}(s) = \frac{-26.984s(s^2 + 1.807s + 11.79)}{(s + 8.052)(s - 0.11)(s^2 + 1.68s + 13.32)} \tag{5.66}$$

When Eqn. (5.65) and (5.66) are compared, it is noticed that the transfer function modeling and state space modeling results are very close, although roll modes are different. The comparisons of the dynamics modes are given in Table 5.16.

Table 5.15 Comparison of Short Period Modes of Both Model

		ω_{nd}	ζ_d
DUCTH-ROLL	TF MODEL	2.638	1.649
	SS MODEL	2.648	1.669

Table 5.16 Comparison of Lateral/Directional Modes of Both Models

		ω_{nd}	ζ_d
DUCTH-ROLL	TF MODEL	3.650	0.460
	SS MODEL	3.463	0.541
		T_r	
ROLL	TF MODEL	0.124	
	SS MODEL	0.197	
		t_{double}	
SPIRAL	TF MODEL	6.341	
	SS MODEL	8.627	

Also, Eqn (5.63) and (5.64) and Eqn. (5.65) and (5.66) are compared in frequency domain by plotting Bode plots and in time domain by plotting their step responses. As seen in Figure 5.13, the frequency responses of the models are close to each other. It is seen that from the tables and figures where the transfer function models and state space models are compared, the results of both model are quite consistent.

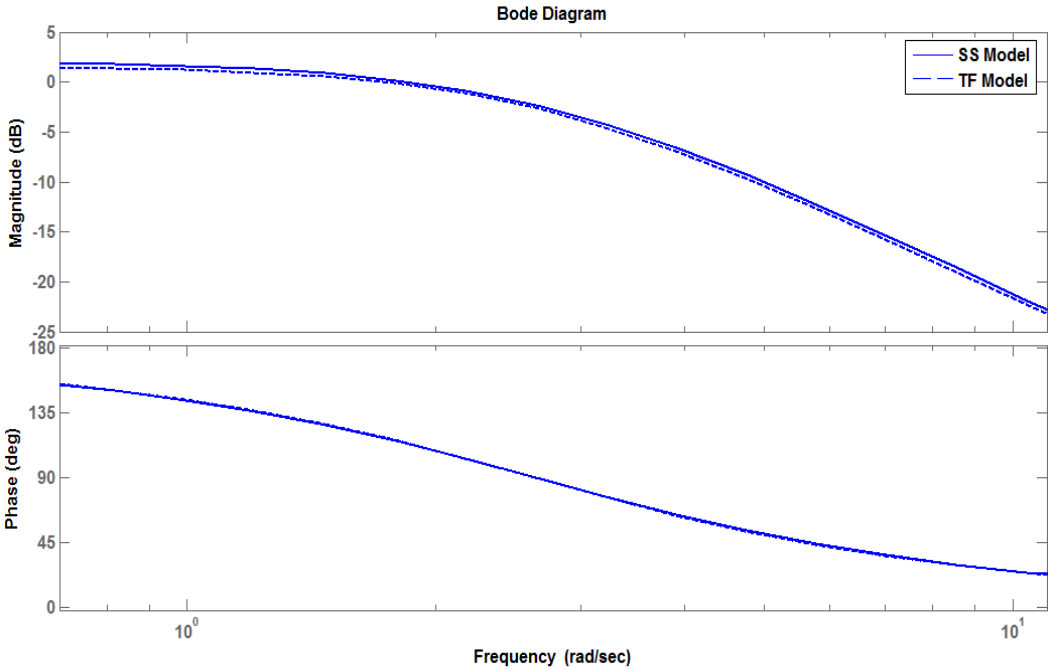

Figure 5.13 Bode Plots of Long. SS and TF Models

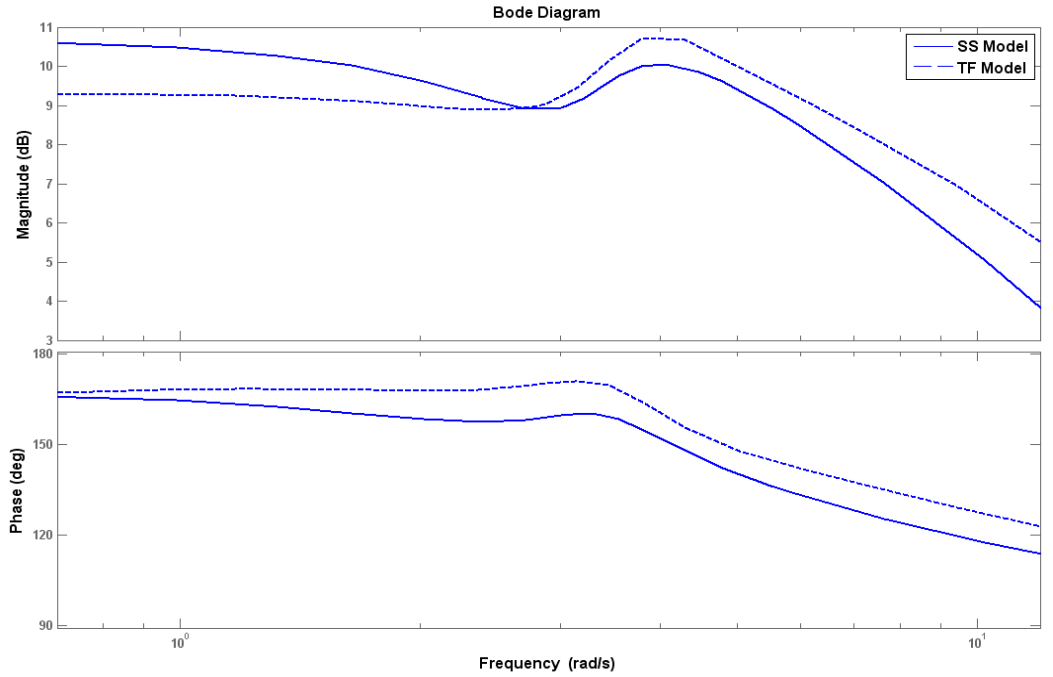

Figure 5.14 Bode Plots of Lat. / Dir. SS and TF Models

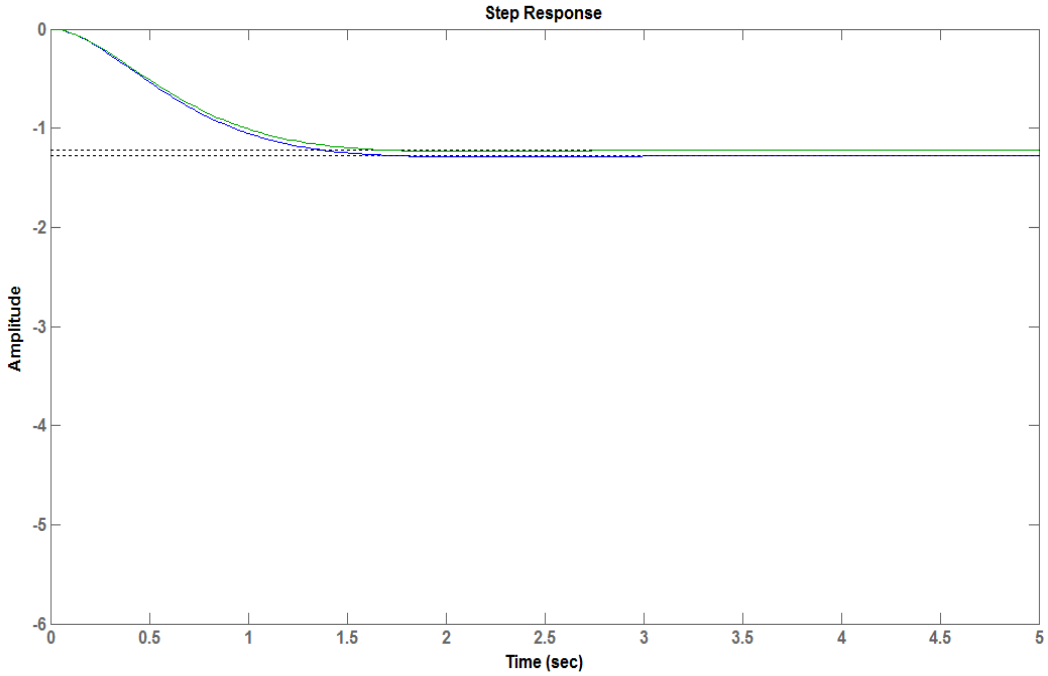

Figure 5.15 Comparison of Short Period Modes of Both Models

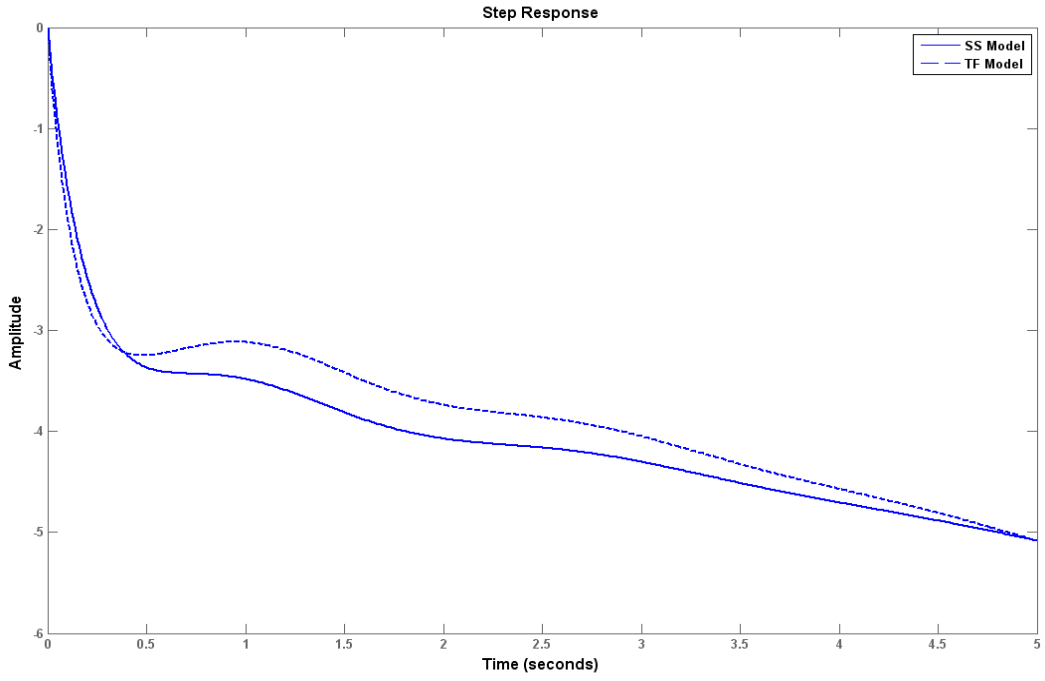

Figure 5.16 Comparison of Lat/Dir Modes of Both Models - Zoomed due to divergence

CHAPTER 6

CONCLUSION AND FUTURE WORK

6.1 Conclusion

The results of the study show that with the system identification, a practical, accurate and verified way of obtaining linear model of the A/C is possible. An accurate model obtained in a short time gives a chance to quickly determine the proper controller gains. The advantage of this is obvious: the number of flights planned for tuning the gains is reduced resulting in reduced cost and reduced risk.

Generally in literature, the inputs are designed to have a certain shape with sharp edged. However, in flight tests, due to pilot and servo dynamics, these inputs cannot be realized. In this study, the theoretical inputs and realized inputs in the flight tests are compared and it is seen that performing exactly the same designed input is not needed if sufficient excitation to the associated mode to be identified is provided.

It is shown that the estimation of all the parameters in A matrix of the longitudinal state space model is possible by using elevator input only. To estimate these parameters, the flight test data must have excitation in both phugoid and short-period modes. Since the flight test data in this study does not include phugoid excitation, this mode could not be identified.

When the time domain verification is applied, it is important to filter the flight test data to keep frequency range of the data in the range of interest. However, in frequency domain identification the filtering is not needed since the identification is carried out for the selected range of frequencies.

When the time domain verification of transfer function and state space models and their comparison are concerned, it is seen that successful models of the UAV are obtained in this study. However, there is some difference between transfer function model and state space model; therefore, selecting state space model results is more proper. One of the reasons is that the transfer function models are derived from single input single output system; however, state space models are derived from multi input multi output system. For example, the lateral/directional motion is identified from only $p/\delta a$ or $\beta/\delta r$ responses in transfer function modeling. In the state space model, on the other hand, the lateral/directional motion is identified from $p/\delta a$, $r/\delta a$, $a_z/\delta a$, $\beta/\delta a$, $p/\delta r$, $r/\delta r$, $a_z/\delta r$, $\beta/\delta r$ responses. The other reason is that state space model structures are derived from Equations of Motion and accuracy analyses in this modeling prevent the modeler from over parameterized model of the dynamics. Although, in this study, both models are very close to each other except roll mode, due to these reasons, the state space model and transfer functions derived from this model is decided to be the preferred approach in flight model identification.

6.2 Future Work

In the flight tests of this study, a good throttle excitation input could not be realized and the phugoid mode was not excited. The reasons of that are that A/C responses to throttle inputs contain nonlinearities such as saturations and the flight leg for sweeps was too short to excite the phugoid mode. To overcome these problems, the engine dynamic model will be identified using subsystem component modeling and phugoid mode will be excited using pulse type throttle inputs and the identification of this mode will be done by concatenating these inputs.

Moreover, the results cover only cruise flight conditions. To identify takeoff and landing characteristics that include ground effect and different flap configurations; the flight test will be done to obtain data for these conditions.

REFERENCES

[1] Anon, *He Has a Question for Any Answer*, Interview with K. Iliff by M. McCall, Antelope Valley Press, CA, Nov. 1, 1994

[2] Astrom, Fundamental Limitations on Control Design, Ecoles des Mines, Fontainebleau, 2001

[3] Bendat, J.S., and Piersol, A.G., Random Data: Analysis and Measurement Procedures, 2nd ed., Wiley, New York, 1986

[4] Bhandari, S., Colgren R., Lederbogen, P. and Kowalchuk, S., *Six-DoF Dynamic Modeling and Flight Testing of a UAV Helicopter*, AIAA Modeling and Simulation Technologies Conference and Exhibit, San Francisco, CA, 2005.

[5] Bischoff, D. E., and Palmer, R. E., *Investigation of Low Order Lateral Directional, Transfer Function Models for Augmented Aircraft*, AIAA Guidance and Control Conference, Paper 82-1610, Aug. 1982, pp. 579-586.

[6] Chao, H., Cao Y., Chen Y., *Autopilots for small fixed-wing unmanned air vehicle: A survey*, IEEE Int. Conference on Mechatronics and Automation, pp. 3144–3149, 2007.

[7] Civilian Applications of UAVs – A California Perspective, a Policy Symposium. Retrieved April 2013 from http://www.aiaa.org/cauav/

[8] Cotting, M.C., *Evolution of Flying Qualities Analysis: Problems for a New Generation of Aircraft*, Ph. D. Thesis, Virginia Polytechnic Institute and State University, Virginia, 2010

[9] Daly M., Streetly M., *Jane's All the World's Aircraft: Unmanned,* Jane's Publishing Ltd, London, 2009

[10] Jategaonkar, R. V., *Flight Vehicle System Identification: A Time Domain Methodology*, edited by Lu, F. K., Vol. 216, Progress in Aeronautics and Astronautics, AIAA, August, 2006, Reston, VA. AIAA Inc., Reston, VA, 2006

[11] Evans, J., Elkaim G., Lo Sherman, Parkinson Bradford, *System Identification of an Autonomous Aircraft using GPS*, ION Global Positioning System Conference, pp. 1065-1074, 1997

[12] Field, E.J., Rossito, K.F. and Hodgkinson, J. *Flying Qualities Applications of Frequency Responses Identified from Flight Data,* Journal of Aircraft, Vol. 41, No. 4, July-August 2004

[13] Fourier Transform. Retrieved August 2013 from http://wikipedia.com

[14] Hodgkinson, J., *Aircraft Handling Qualities*, AIAA Inc., Reston, VA, 1998.

[15] Hodgkinson, J. and Wood J.R., *Definition of Acceptable Levels of Mismatch for Equivalent Systems of Augmented CTOL Aircraft*, McDonnell Aircraft Company, 1984.

[16] Klein, V (1977), *Compatibility Check of Measured Aircraft Responses Using Kinematic Equations and Extended Kalman Filter*, NASA TN D-8514, Washington D.C.

[17] Klein, V., and Morelli, E. A. (2006), Aircraft System Identification: Theory and Practice, AIAA Inc., Reston, VA.

[18] McRuer, D.T., Ashkenas, I.L., and Graham D., *Aircraft Dynamics and Automatic Control*, Princeton Univ. Press, 1973

[19] Military Handbook, Flying Qualities of Piloted Aircraft, MIL-HDBK-1797, 1997

[20] Mitchell, D.G. and Hoh, R.H. *Low Order Approaches to High Order Systems: Problems and Promises*, AIAA 82-4250, 1982.

[21] Morelli, E.A., *Identification of Low Order Equivalent System Models from Flight Test Data*, NASA TM-2000-210117, August 2000.

[22] Morelli, E. A., *Low Order Equivalent System Identification for the Tu-144LL Supersonic Transport Aircraft*, Journal of Guidance, Control, and Dynamics, Vol. 26, No. 2, pp. 354-362, 2003.

[23] Ogata, K., *Modern Control Engineering*, 3rd Edition, AIAA Inc., Reston, VA, 1997.

[24] Prosser, C. F., and Wiler, C.D, *RPV Flying Qualities Design Criteria*, AFFDL-TR-76-125., WPAFB, OH, 1976.

[25] Rabiner, L. R., *Theory and Application of Digital Signal Processing*, Prentice-Hall, Upper Saddle River, NJ, 1975

[26] Roskam, J., *Airplane Flight Dynamics and Automatic Flight Controls,* DARcorporation, Lawrence, KS. Prentice Hall Inc., Upper Saddle River, NJ, 2001

[27] Schafer, R.W: *What Is a Savitzky-Golay Filter,* IEEE Signal Processing Magazine, pp.111-117, July 2011

[28] Tischler, M. B., and Remple, R.K., *Aircraft and Rotorcraft System Identification: Engineering Methods with Flight-Test Examples*, AIAA Inc., Reston, VA, 2006.

[29] United States Department of Defense, *Dictionary of Military and Associated Terms,* Joint Publication 1-02, 2001, p. 557.

[30] Unmanned Aircraft Systems, Advantages of UAVs. Retrieved May 2013 from http://www.uavs.org/advantages

[31] User Guide, CIFER Version 6.0.00 (Student Version), 2011

[32] User Guide, Simulink Parameter Estimation, MATLAB 2007b

[33] Williams, J.N., Ham J.A., and Tischler M.B., *Flight Test Manual: Rotorcraft Frequency Domain Flight Testing*, Airworthiness Qualification Test Directorate, California, CA, 1995

[34] Zadeh, L., *From Circuit Theory to System Theory*, Proc. IRE, Vol. 50, pp, 856-865

APPENDIX A

AIRCRAFT EQUIPMENT SPECIFICATIONS

The UAV is equipped with one EGI and the device is connected to a FCC and a data logger using its RS-232 serial interfaces. The EGI used in A/C is IG-500N. IG-500N is the world smallest GPS enhanced Attitude and Heading Reference System (AHRS). With its embedded Extended Kalman Filter, the IG-500N delivers unmatched precision for attitude and position measurements. The specifications of IG-500N are given in Table A.1.

Two pressure transducers are put in UAV to get static and total pressure information from the probe. The transducers are chosen as Honeywell 1PSI and Honeywell 20PSI PPTs (Precision Pressure Transducer). The transducers have analog outputs; therefore for FCC, the analog data are converted to serial input. The specifications of 20 PSI transducer is given in Table A.2

The FCC communicates with the EGI, the data logger, the data link and the DGPS by using its RS-232 ports. The specifications of FCC device are given in Table A.3.

The data logger system uses its RS-232 port to communicate with FCC and its Ethernet port to communicate with data link. UEILogger is selected as a data logger. The recorded data are the outputs of FCC. The data are sent to ground station using data link. The specifications of data logger are given in Table A.4.

Table A.1 EGI Specifications

IG500N Specifications			
All specifications are valid in the full temperature range -40°C to 85°C			
Attitude			
Static Accuracy	±0.5°	for Pitch-Roll	
	±1.0°	for Heading	
Dynamic Accuracy	±1.0°	RMS	
Resolution	<0.05°		
Output Frequency	0.01 to 500 Hz		
	Accelerometer	**Magnetometer**	**Gyroscope**
Measurement Range	±5g	±1.2 Gauss	±300°/s
Bias Stability	±4mg	±0.5 mGauss	±1.0°/s
Noise Density	0.25mg/√Hz	0.01mGauss/√Hz	0.05°/s/√Hz
Alignment Error	<0.1°	<0.25°	<0.1°
Sampling Rate	10000Hz	1000Hz	10000Hz
Communication			
Outputs	Euler Angles	Quaternion	Matrix
	3D Velocity	3D position	UTC Time
	Calibrated	Raw	
	Sensor Data	Sensor Data	
Interfaces	Serial(RS-232)	USB	

Table A.2 Transducer Specifications

Honeywell 20PSI Specifications	
Accuracy	±0.12% FS for analog input
Range	20 PSI
Resolution	0.024% FS over 0-5V
Operating Temp	-40°C to 85°C
Sample Rate	100Hz

Table A.3 FCC Specifications

FCC Specifications	
Processor	AMCC 405GP
RAM	Up to 128MB
Ethernet	1 x 10/100 with RJ-45 connector
Serial Ports	2 x RS-232

Table A.4 Data Logger Specifications

UEILogger Features
Up to 150 analog inputs or 288 digital inputs per cube
Stores data on standard SD Card
Samples up to 1000 samples/second per channel
Can be run as a standalone device
3 x I/O Slots
Operates -40°C to 85°C
1 x RS-232 Serial Port
2 x Ethernet Connectors

The data link in the UAV system is used to get the data from UAV to ground station for online data monitoring and to send the comments other than pilot commands such as; gains for control system. The specifications of data link are given in Table A.5.

Table A.5 Data Link Specifications

Data Link Specifications	
Link Rate	1.1 Mbps
Range	100km
Sensitivity	-112dBm
Ethernet	10/100 BaseT
Serial Interface	RS-232

APPENDIX B

SOFTWARE AND THEIR USAGE IN IDENTIFICATION PROCESS

B.1 CIFER

AFDD (The Army Aeroflightdynamics Directorate) at Ames Research Center developed the CIFER® (Comprehensive Identification from Frequency Responses) software for system identification in frequency domain.

CIFER key features are listed as:

- The identification algorithm in CIFER have been proven on many flight project
- The program checks the user data according to key guidelines in identification
- CIFER obtains high quality frequency responses by using Chirp-Z transformation and windowing optimization
- CIFER provides weighting function selection based on response accuracy while cost is calculated
- Interface provisions of CIFER are made for common programs e.g. MATLAB and Excel vs.

The software consists of six-analysis program and the working process and organization is given in Figure B.1 The Top-Level CIFER Product Organization [28].

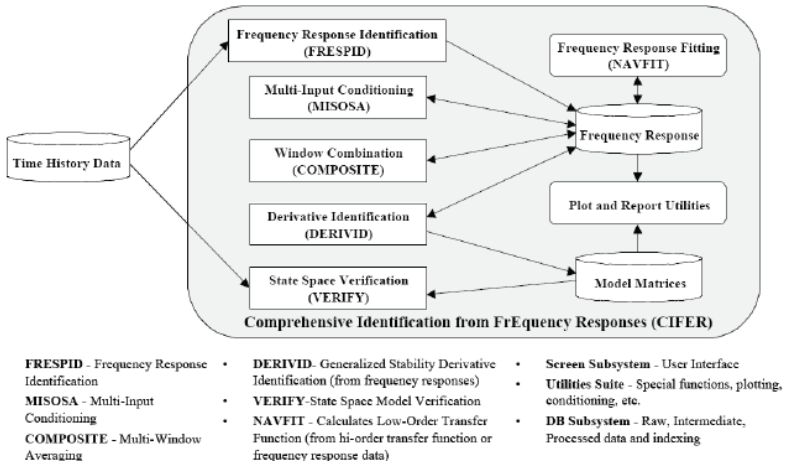

Figure B.1 The Top-Level CIFER Product Organization [28]

In this thesis, 4 of 6 analysis modules are used: FRESPID to obtain frequency responses from time history data, then COMPOSITE is used to obtain windowing optimization, NAVFIT is used to obtain transfer function model and DERIVID is used to obtain state space model. Since multi input single output model structure is not suitable for aircraft dynamics in this thesis, MISOSA is not used. An analysis similar to DERIVID is applied by using software; since verifying the results with another program, which works on another domain, seems to be more impressive way of verification. Therefore, MISOSA and DERIVID modules are not used.

The detailed information about modules and how these modules are used in this thesis are given in the next sections. CIFER 6.0.00 Student Version is used in this thesis.

B.1.1 FRESPID

This tool gets the time history data and filters it digitally to eliminate high frequency noises, and then apply overlapped windowing method to reduce random error [28]; after that, this time history data are transformed into frequency domain using Chirp-Z transformation and spectral functions are obtained. Finally, using these spectral functions, coherence functions and frequency response functions (and their Bode plots) are obtained to be used in frequency domain system identification.

The user interface for FRESPID are given in the figures and for each screen, the explanations take place under the figures. All the process in FRESPID is explained in step-by-step based on the information in CIFER User's Guide [31].

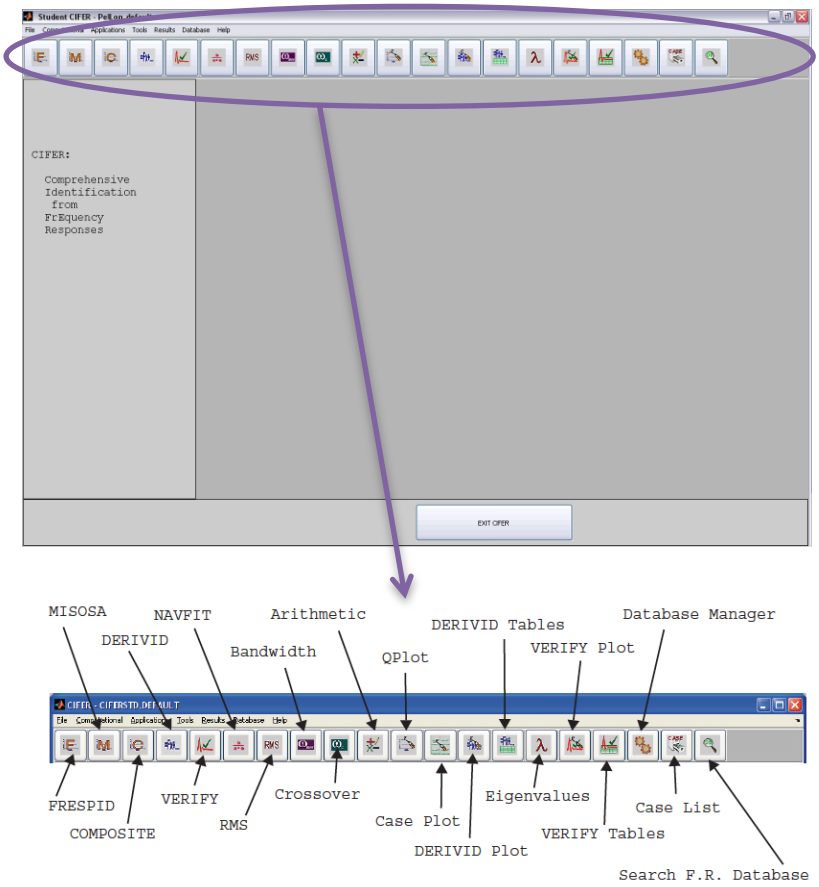

Figure B.2 Main Page and Shortcut Bar

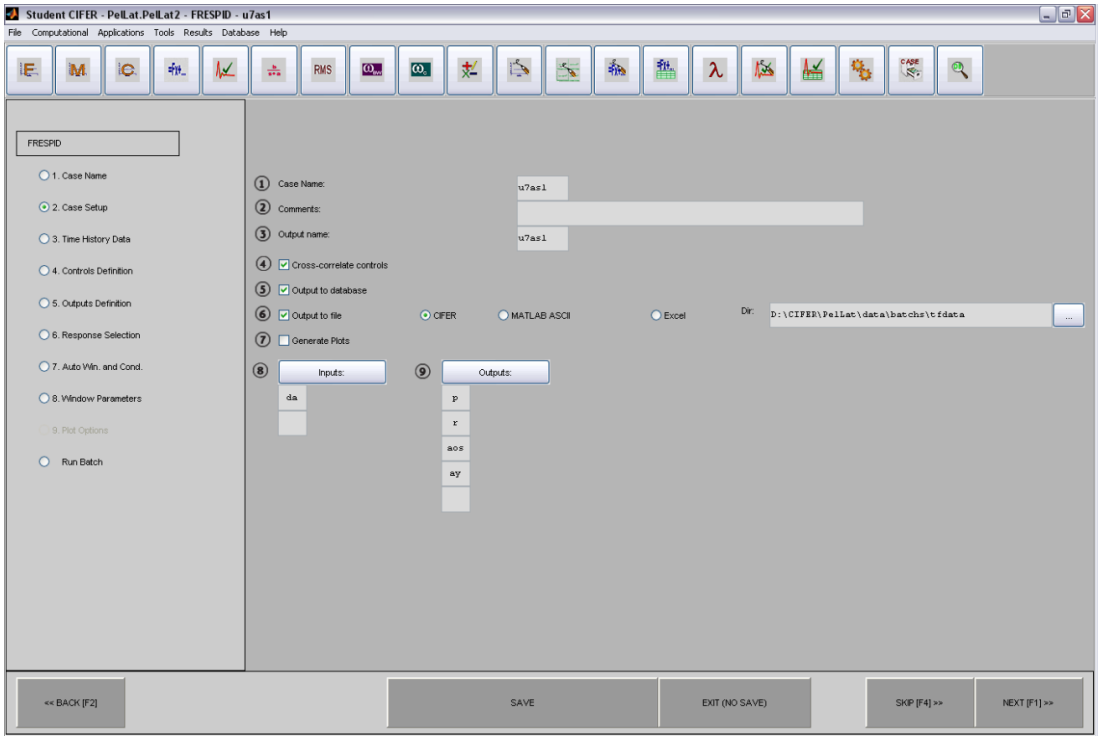

Figure B.3 FRESPID Case Setup Page

In Case Setup page, the names of the case, inputs and outputs are specified.

1. Case Name
2. Comments
3. String used to name the output frequency responses
4. The box is checked if cross correlation between inputs is wanted, which is used for MISOSA analysis
5. The box is checked if frequency responses are wanted to save in CIFER output format
6. Determine whether or not the output file is generated. Moreover, the format and address of the file are defined.
7. Determines whether or not the plots are drawn
8. User defines the input names using up to 4 characters
9. User defines the output names using up to 4 characters

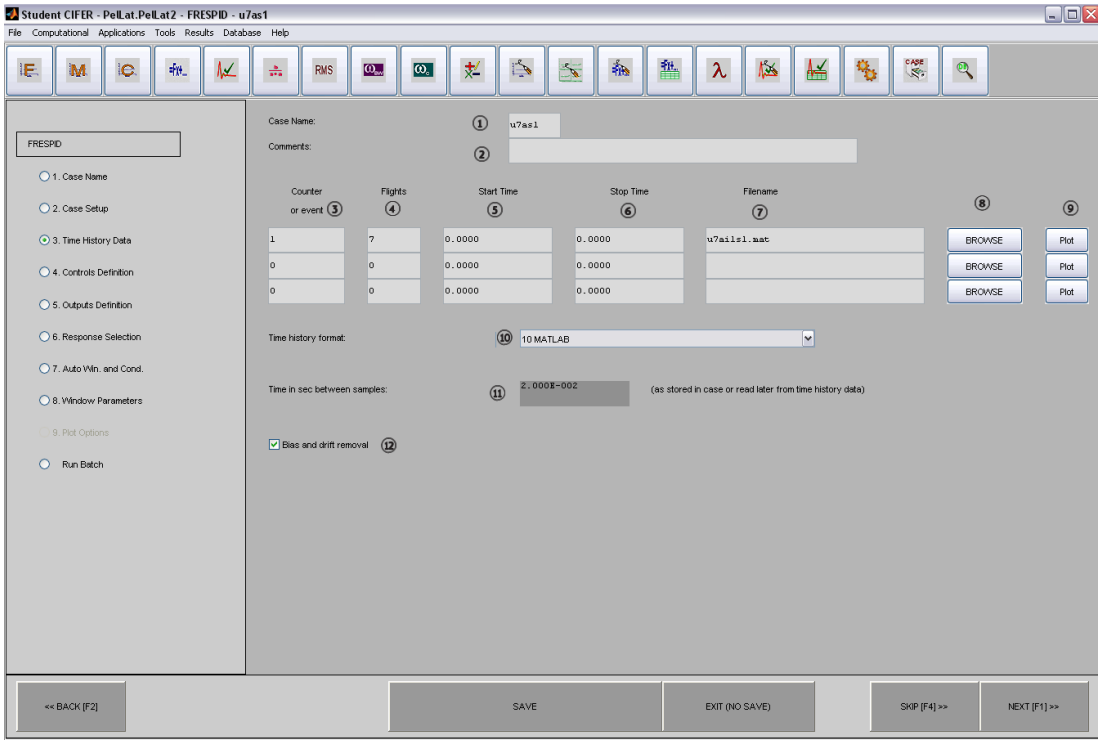

Figure B.4 Time History Data Page

1. Case name
2. Comments
3. The event number, to specify the imported time history data
4. The flight number, to specify the imported time history data
5. Optional start time offset, to define a starting point to CIFER from the data
6. Optional stop time, to define an end point to CIFER; if it is 0, then CIFER takes end of the data as an end point
7. Name of the time history data (It is filled by CIFER when the Browse button is used)
8. Browse for the time history data
9. Plot option to check the data in time history data; it plots only one user defined parameter at one time.
10. Indicates time history data format
11. Time between samples, the unit is second and it is required for some data formats only.
12. It must be checked when frequency responses are computing

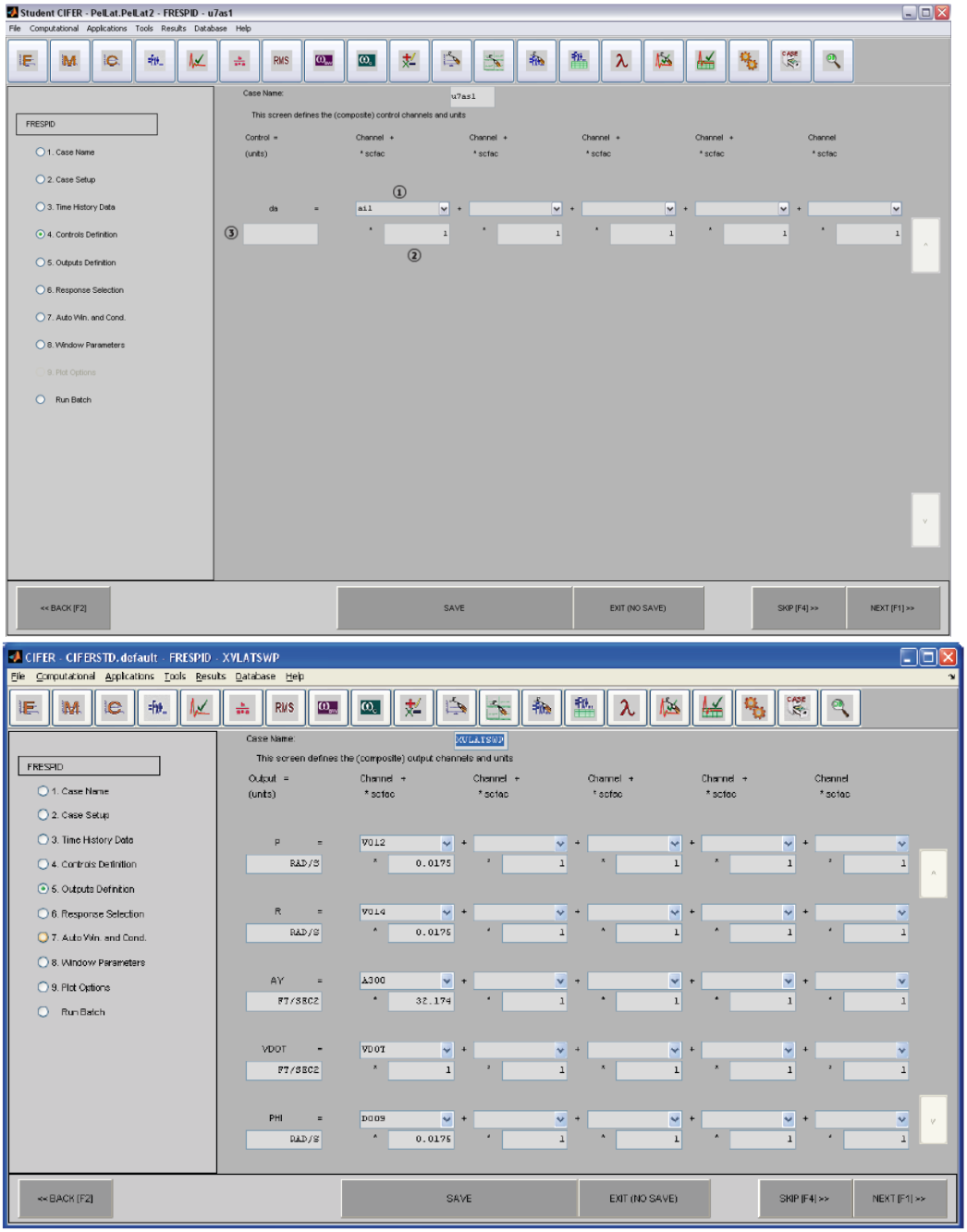

Figure B.5 Control and Output Definition Pages

In these screens, the input and output names defined in the case are matched with the variables in the time history data.

1. Variable name in the time history data
2. Scale factors (due to unit conversions, etc.)
3. Comments, usually the units are noted.

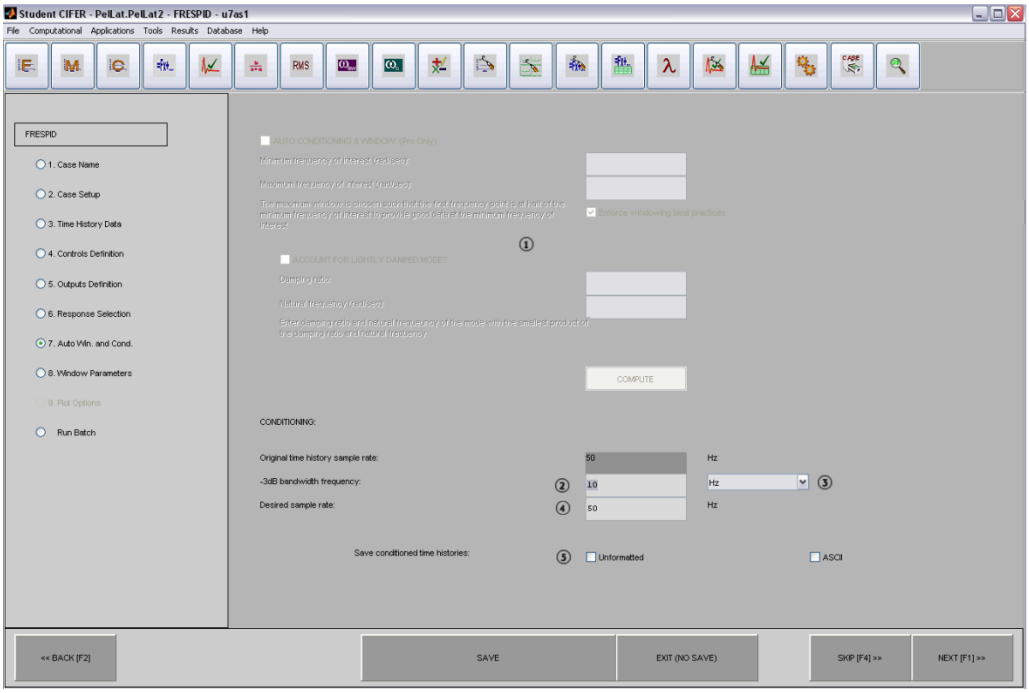

Figure B.6 Auto Windowing and Conditioning Page

In this screen, the data samples are arranged. The higher frequencies, beyond the frequency range of interest are filtered.

1. In the pro version only
2. Bandwidth frequency for the filter
3. The unit of the defined bandwidth frequency
4. Desired sample rate
5. The format options for conditioned time histories

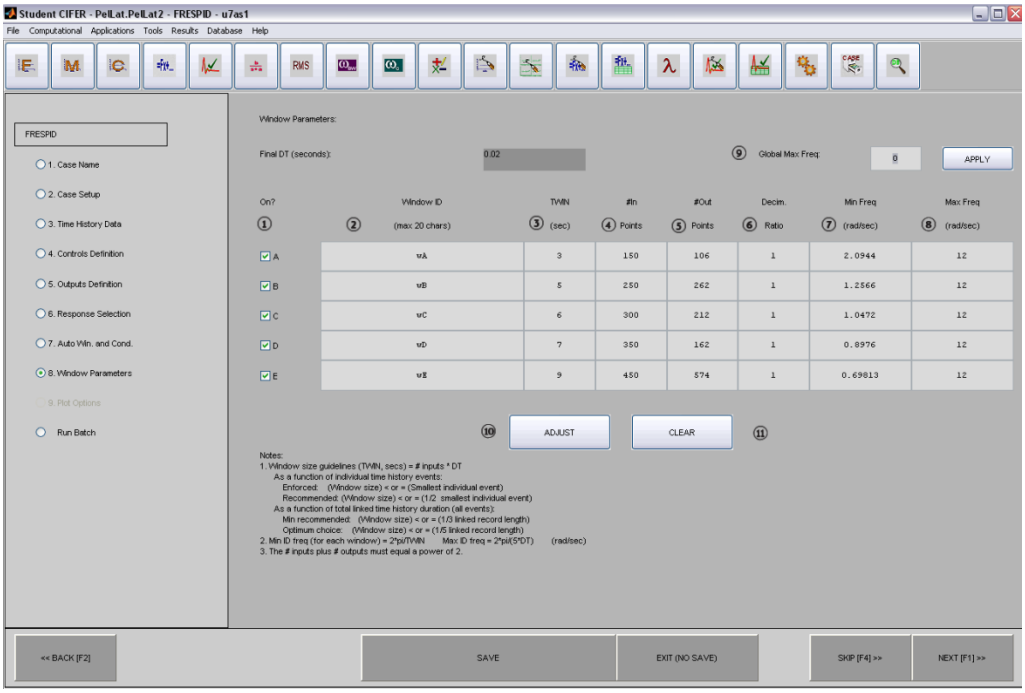

Figure B.7 Window Parameters Screen

In this screen, the number of the windows and their parameters are defined. The window size determines how much data is processed by FFT at a time.

1. The checked boxes shows that which user defined windows are used in generating frequency responses. The program generates frequency responses for each window separately.
2. Comments
3. Window size in seconds
4. Number of points sent to the FFT
5. Number of points returned by the FFT
6. Decimation ratio for storing the response
7. Minimum frequency of interest
8. Maximum frequency of interest
9. To define same maximum frequency of interest for all windows quickly
10. Adjust button to fill the other values of window using desired sample rate and window length
11. Clear button is to delete the values added by adjust button

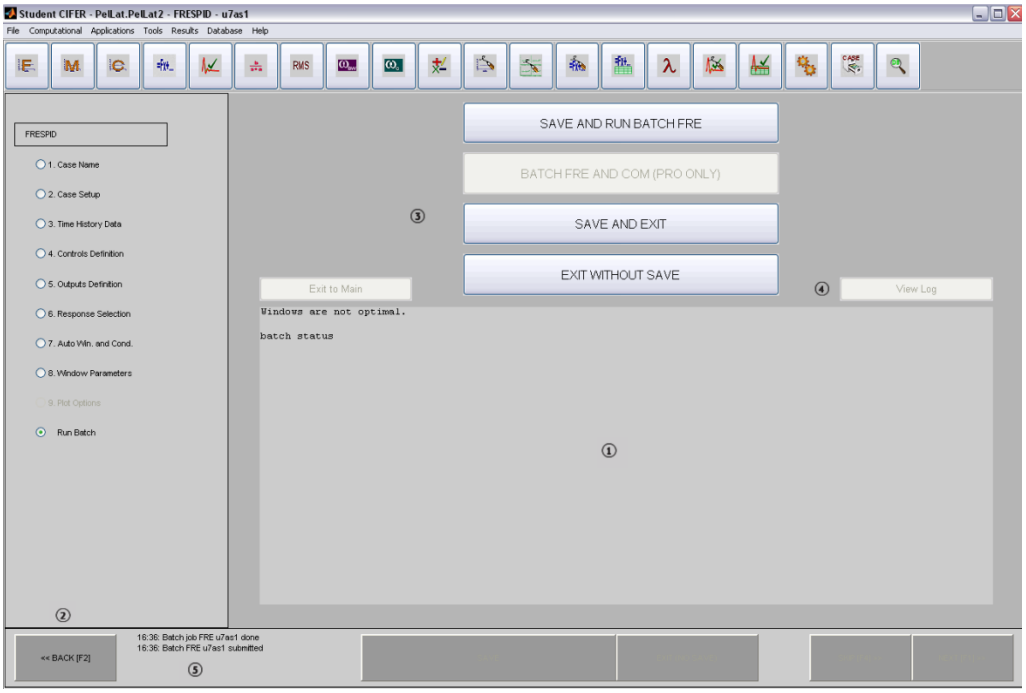

Figure B.8 Run Batch Page

The screen is used to run the FRESPID case, which is also called as batch job.

1. Shows the warnings and cautions by checking the suitability of user inputs for windowing.
2. Before submitting the batch job, the previous pages can be opened again using Back button, F2 key or navigation panel.
3. There are 3 options to do with the data user entered. The 2. Option is available in pro version. The options are save and run, save and exit, exit without save
4. After the batch is run, the calculation log can be viewed.

The FRESPID module is explained step by step to show the user interface of CIFER and how the screens are used and make the reader familiar with the screens. The above figures seem enough to understand the user interface; therefore, other modules are not explained step-by-step, only important screens of other modules are shown while explaining how the modules are used in identification.

B.1.2 COMPOSITE

COMPOSITE merges the results of the windows defined in FRESPID and using optimization, it finds a single frequency response estimates with an optimum quality and frequency range. Thus, this tool clears away the manual adjustment and assessment of window length and satisfies a balance between information content at low frequencies and number of averaged data, which reduce the random error.

COMPOSITE tool is used the frequency responses in FRESPID or MISOSA and it also used the windows selected in FRESPID tool. The optimization method in COMPOSITE tool is quasi-Newton-Raphson [28].

Figure B.9 COMPOSITE Setup Page

In this screen, the user specifies the input and output, the source tool of frequency responses and the windows used in COMPOSITE tool.

1. Case name
2. Comments
3. Program that generated the input frequency responses.

4. Name of the freq. responses
5. Name of the final composite freq. response.
6. Check this to store composite responses in the database.
7. Check this to write responses to individual files.
8. Check this to generate plots.
9. Shows the number of frequencies in the resulting responses.
10. Inputs for processing.
11. Outputs for processing.
12. Windows for processing.

B.1.3 NAVFIT

NAVFIT is a tool for SISO transfer function modeling in frequency domain. NAVFIT satisfies a LOES fitting to frequency response of aircraft dynamic.

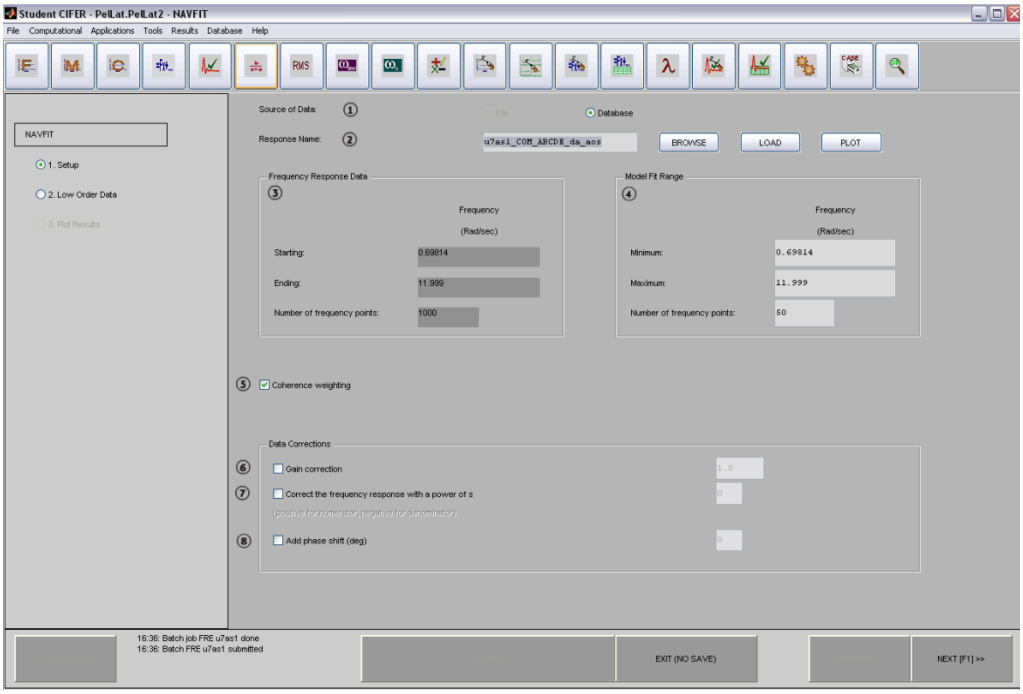

Figure B.10 NAVFIT Setup Page

In the Setup page, the frequency response, which will be identified, is chosen and the LOES fit range is determined.

1. Determines whether the frequency responses comes from the database or a file
2. Enter the name of the frequency response.
3. Shows the starting and ending frequencies and the number of points in the frequency response.
4. Specify the min. and max. frequencies over which to fit and the number of points for the fit.
5. Check this to use coherence as a weighting function.
6. A gain correction factor

7. Integration or differentiation of the frequency response
8. A phase shift

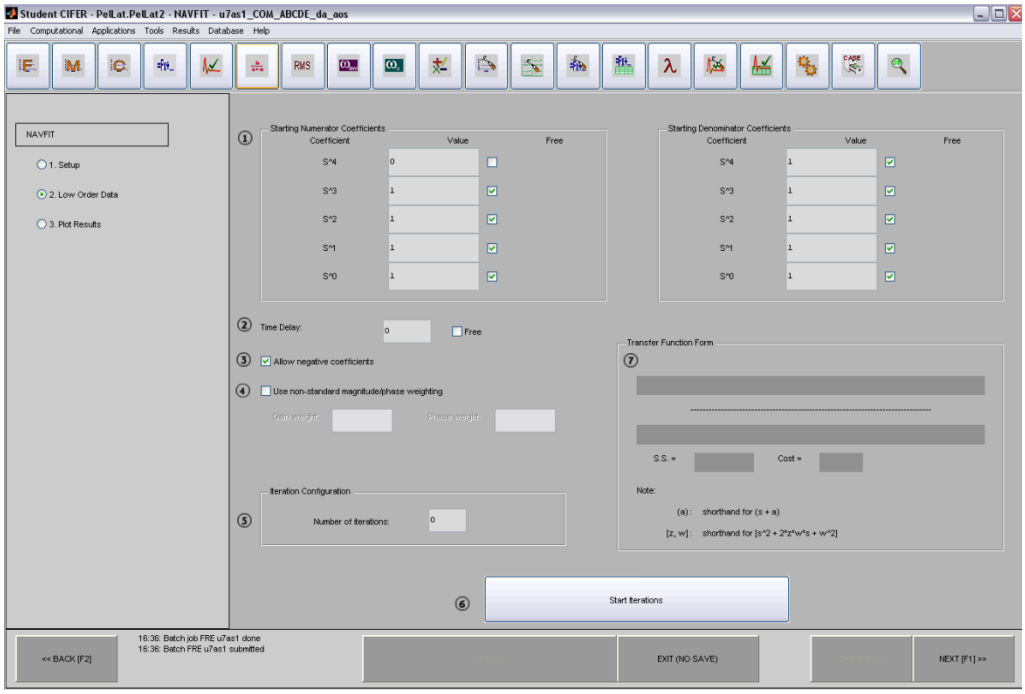

Figure B.11 NAVFIT Low Order Data Page

In this screen, the order of the transfer function and initial conditions of the coefficients are determined. Moreover, the iteration is started at this page, and the results also are seen.

1. Check this boxes to specify free parameters and indicates the initial numerator and denominator coefficients.
2. Check this box to determine whether it is free
3. Check whether negative coefficients may be allowed
4. Non-standard gain and phase weighting
5. Enter the number of iterations
6. Perform the iterations
7. The identified transfer function, the steady state gain and it cost are displayed

B.1.4 DERIVID

This module is used to obtain MIMO state space model identification. In student edition, DERIVID module can be used to identify a model with up to 5 states, 5 outputs and 2 inputs. With this module, the user can identify a state-space model, make an accuracy analysis, and adjust the model structure.

Figure B.12 State Space Names

1. Model name
2. Comments
3. State names
4. Output names
5. Control names
6. Number of frequency points used in the identification
7. Relative weighting of magnitude and phase errors.

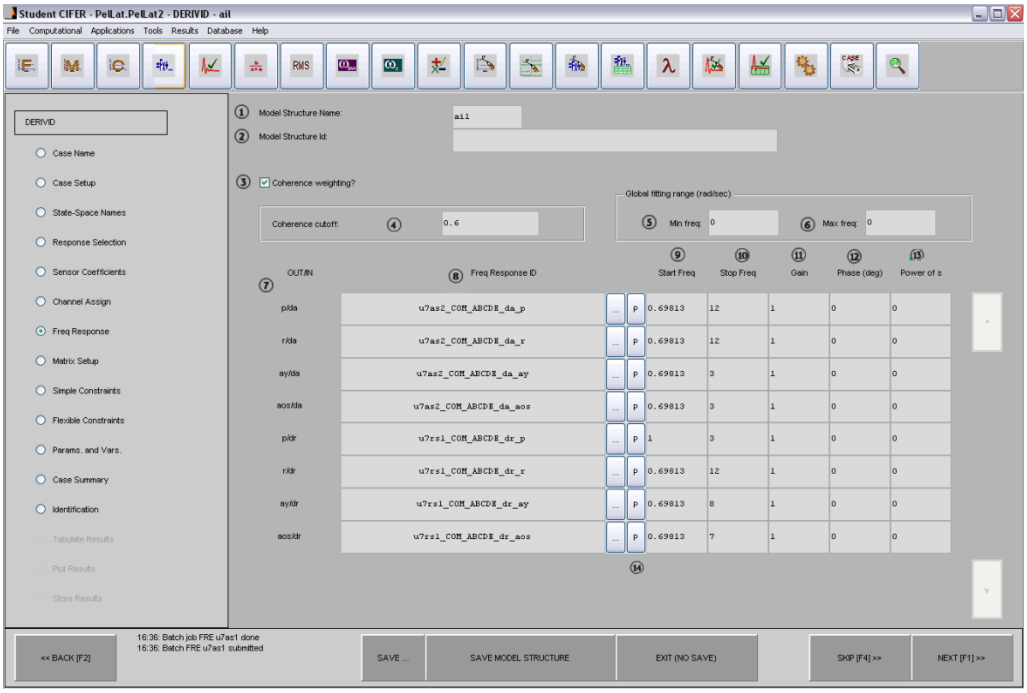

Figure B.13 Frequency Response Page

1. Model name
2. Comments
3. Indicates whether the coherence is used as a weighting function
4. Determine the coherence bottom limit for identification analysis
5. The min overall frequency for all responses used in the identification.
6. The max overall frequency for all responses used in the identification.
7. The input output pairs
8. The selected frequency response
9. The min. freq. to use for this response, this value is not used if it is less than min. overall frequency
10. The max. freq. to use for this response, this value is not used if it is greater than max. overall frequency
11. A gain is applied for each response
12. A phase shift for each response
13. Integration or derivation of each responses
14. Use to generate plots of frequency responses

Figure B.14 Matrix Setup Page

1. Matrix tabs
2. Name of the selected matrix
3. Comments
4. To set all parameters to fixed or free
5. Indicates whether the parameter is free or fixed
6. The name of the parameter
7. The constant part of the parameter
8. The variable part of the parameter

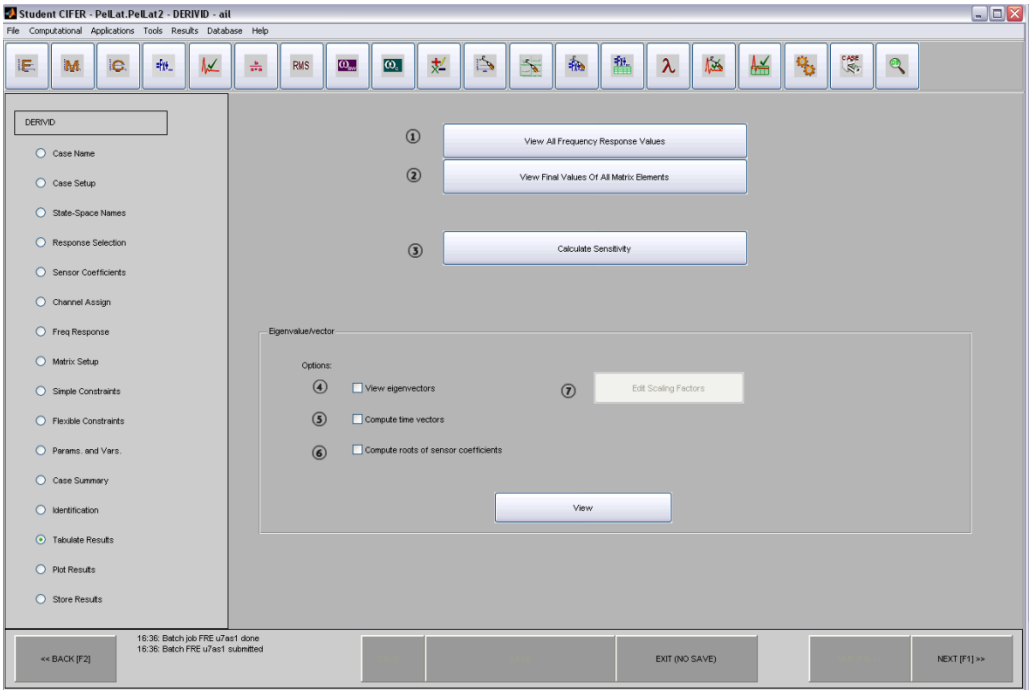

Figure B.15 Tabulate Results Page

1. To view all the phase and magnitude values for frequency response data
2. To view the result matrices
3. To compute the Cramer-Rao bounds, insensitivities for each parameter
4. To view the eigenvectors and eigenvalues
5. To view the time vectors and eigenvalues
6. To view the roots of the sensor transfer functions

B.2 SIMULINK PARAMETER ESTIMATION

Simulink Parameter Estimation in Simulink Design Optimization Toolbox, which is called as SimPE in this study, is a tool to estimate identification parameters [32]. SimPE estimates the parameters and ICs of states to minimize cost function, which is chosen by the user. Before estimation process, firstly the data must be assigned to the Simulink model channels. In order to assign, Simulink model must include:

- Top-level Inport block
- Top-level Outport block or Logged signal

The software has The Control and Estimation Tools Manager GUI, the assignment of measured data and estimation processes are applied using this GUI. A picture of the GUI is given in Figure B.16

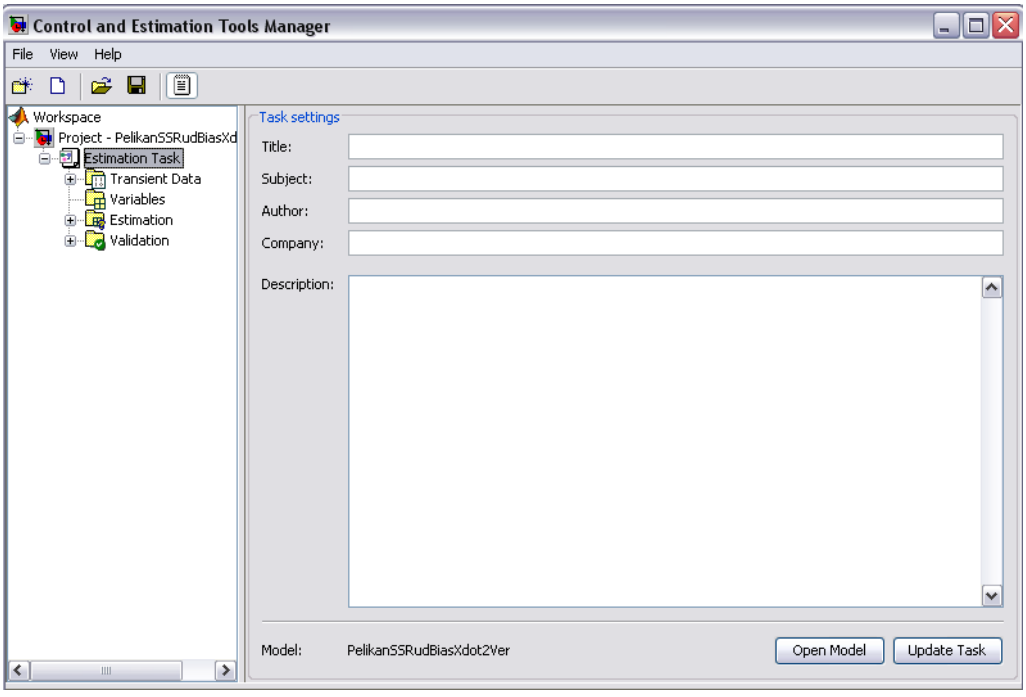

Figure B.16 SimPE GUI Main Page

To start the estimation, firstly an estimation task is created. The estimation task has 4 nodes: transient data, variables, estimation and validation.

In transient data node, the measured input and output data are matched with the ports in the Simulink model. The transient data node is shown in Figure B.17. The measured data is imported by using Import button. The measured data must be in the workspace. Time information about measured data must be a parameter in the workspace. Pre-process feature of the node provides some data processing capability such as handling missing data, filtering data, cropping data, etc. Moreover, the imported data can be plotted.

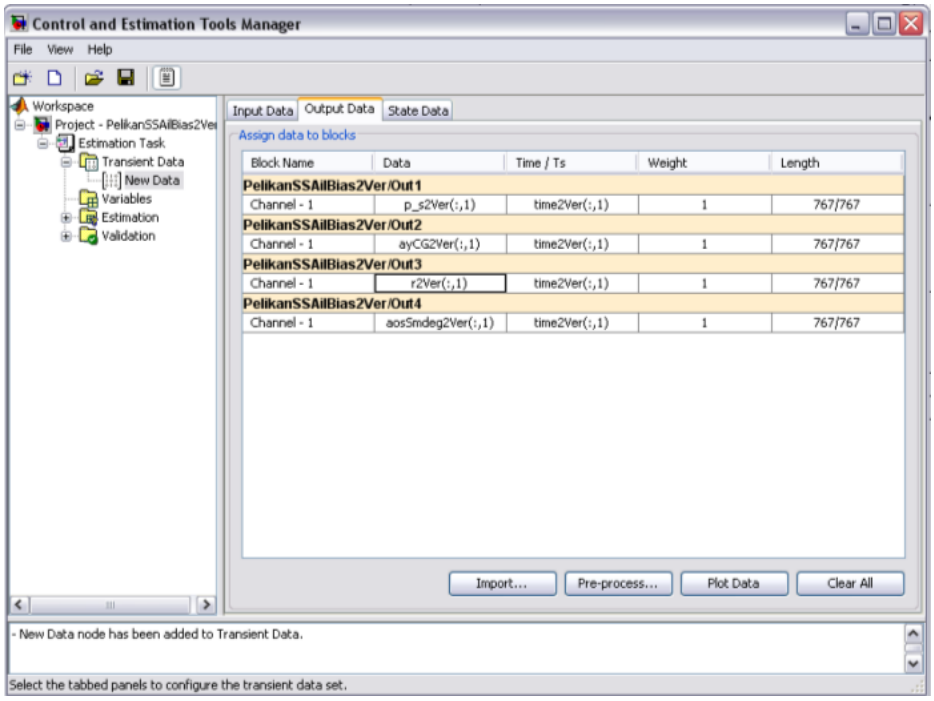

Figure B.17 SimPE Transient Data Node

In variables node, the parameter that will be used in estimation is specified. They are specified by adding to selected parameters section. The default settings of each parameter can be seen and changed in default setting section.

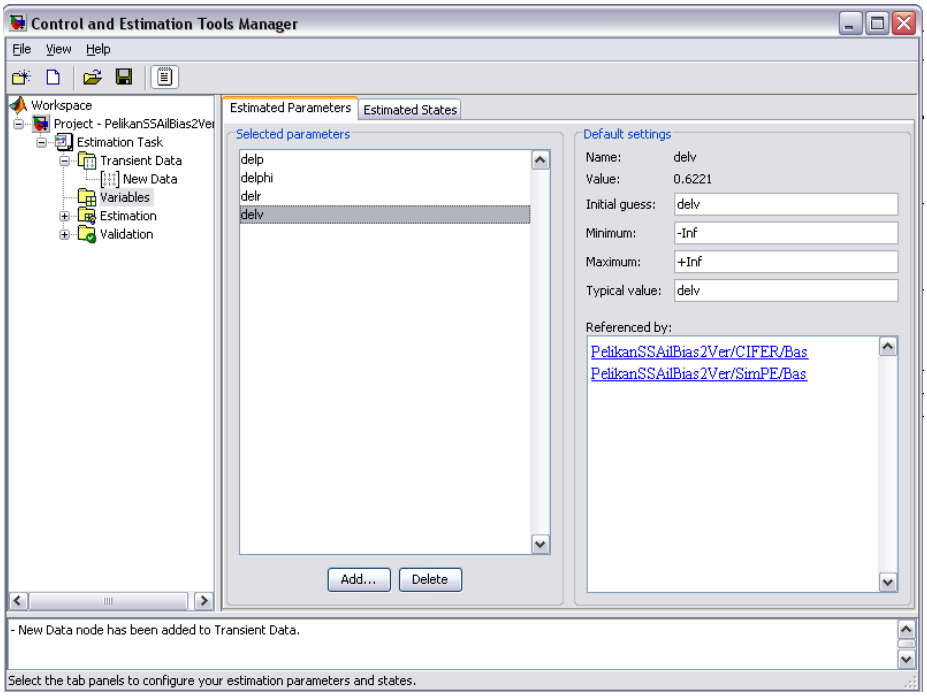

Figure B.18 SimPE Variables Node

In estimation node, estimation method, algorithm options and cost function for the estimation are selected.

The estimation option details are shown in Figure B.19 SimPE Estimation Node and Estimation Option Tab. The optimization methods are:

- Nonlinear least square
- Gradient descent
- Pattern search
- Simplex search

In optimization option section, the limits are defined where optimization terminates:

- Diff max/min change is the maximum/minimum allowable change in variables for finite difference derivatives.
- Parameter tolerance gives the value where if change in the parameter value less than that value, optimization terminates.

After estimation, the values of these parameters are also updated in the MATLAB workspace.

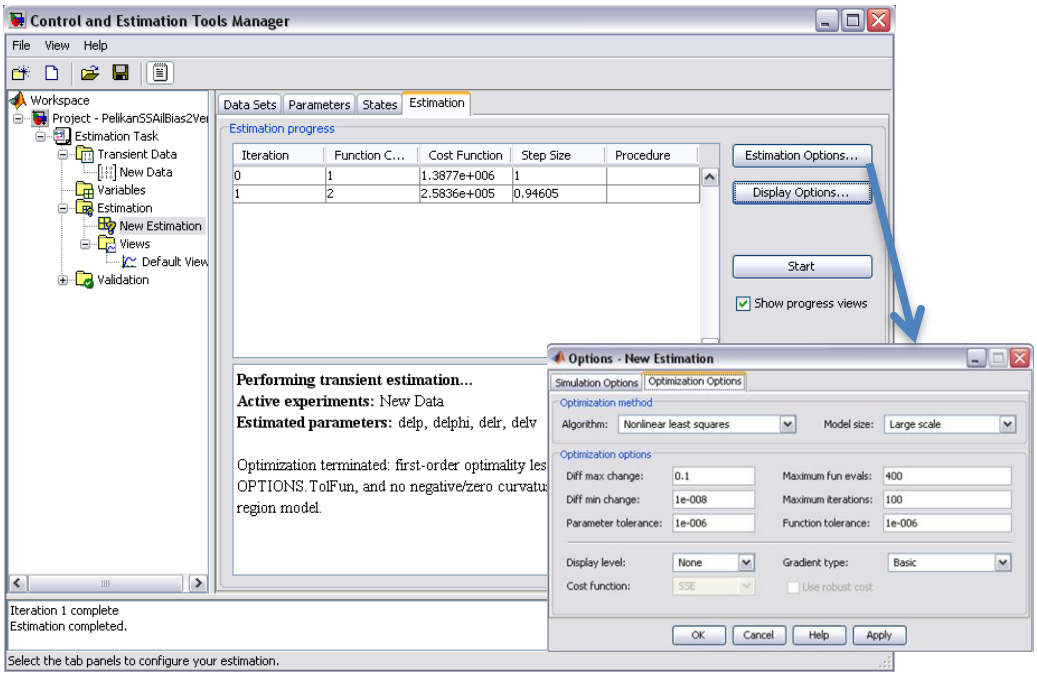

Figure B.19 SimPE Estimation Node and Estimation Option Tab

B.2.1 Nonlinear Least Square Estimation

In the nonlinear least square estimation, the estimation function is nonlinear and the square of the error between estimation function and data are summed and the aim of the estimation is minimizing the error between the system and its estimation function. The equation for nonlinear least square estimation is written as

$$\min_x f(x) = E = \sum_{i=1}^{m} [y_e(x_i) - y(x_i)]^2 \tag{B.1}$$

where y_e is the nonlinear estimation function

Since the estimation function represents the system with an error, which is minimized in estimation, the system equation is written as

$$y(\boldsymbol{x}) = y_e(\boldsymbol{x}) + \varepsilon \tag{B.2}$$

The minimum of the error, E, is obtained by estimating a function which makes the partial derivatives of E with respect to each parameter zero:

$$\frac{\partial E}{\partial x_i} = 0 \tag{B.3}$$

One of the methods to solve nonlinear least square estimation problem is linearization. To obtain a linear model, Taylor expansion of Eqn. (B.2) for initial value, x_0, is written as:

$$y(x_i) \approx y_e\big(\boldsymbol{x_0}(i)\big) + \frac{\partial y_e}{\partial x_i}\Big|_{x_i = \boldsymbol{x_0}(i)} \big(x_i - \boldsymbol{x_0}(i)\big) + \varepsilon \tag{B.4}$$

For $\Delta \boldsymbol{y} = y(\boldsymbol{x})$- $y_e(\boldsymbol{x_0})$, $\Delta \boldsymbol{x} = \boldsymbol{x} - \boldsymbol{x_0}$and $\boldsymbol{A} = \partial \boldsymbol{y_e}/\partial \boldsymbol{x}$, the Eqn. (B.4) becomes

$$\Delta \boldsymbol{y} = \boldsymbol{A}\, \Delta \boldsymbol{x} + \boldsymbol{\varepsilon} \tag{B.5}$$

Then, the normal equation for the least square estimate $\widehat{\Delta x}$ of the increment Δx is

$$\boldsymbol{A^T P A \widehat{\Delta x}} = \boldsymbol{A^T P \Delta y} \tag{B.6}$$

For parameter estimation, a formal solution is

$$\boldsymbol{\widehat{\Delta x}} = (\boldsymbol{A^T P A})^{-1} \boldsymbol{A^T P \Delta y} \tag{B.7}$$

Due to numerical stability issues, this normal equation is not solved by inverting $(\boldsymbol{A^T P A})$, several techniques like Singular Value Decomposition, QR Decomposition, Cholesky Decomposition is applied.